

ABSTRACT

ZHAO, JIANWEI. Inhomogeneous Electric Field-Induced Domain Reorientation and Phase Transitions in Ferroelectrics (Under the direction of Dr. Jacob Jones).

Ferroelectric materials are commonly employed in electronic applications due to their unique electromechanical response. As a part of the applications, piezoelectric multilayer ceramic actuators (MLCAs) have been widely used in the commercial transducer, sensor, and fuel-injection devices because of their low driving voltage, high-strain generation, high precision displacement, and quick response. However, with a voltage applied to the device, high electric field concentrations can develop around the interdigitated electrode edges inside a MLCA to significantly influence the electromechanical response and facilitate the device to failure. Due to the complexity of investigating the field inhomogeneity in MLCAs, a novel research strategy using partially electroded samples is designed and conducted in this research to probe the spatially dependent material behaviors in response to the inhomogeneous electric fields.

This research employs the synchrotron-based *in situ* high-energy XRD with applied fields to uncover their microstructural changes in Nb-PZT-based and KNN-based monolithic samples. The ferroelectric materials studied in this research involve various crystallographic phases, including tetragonal, rhombohedral, and orthorhombic phase. Additionally, a Nb-PZT-based material with a composition nears the MPB region is particularly studied to reveal tetragonal-to-rhombohedral phase transitions in selective crystallographic orientations. The results from full-electrode samples (monolithic ceramic bars with fully painted electrodes) show the most preferred 002, 111, and 202 domain orientation in tetragonal, rhombohedral, and orthorhombic phase, respectively, are parallel along the macroscopic field direction. Particularly, for the Nb-PZT 53/47 composition (near MPB), a new mechanism of field-induced orientation-selective phase transitions is revealed.

In order to develop in-depth understanding of microstructural changes due to electric field inhomogeneity, *in situ* high-energy XRD experiments with different beam sizes were conducted on the ferroelectric partial-electrode samples (monolithic ceramic bars with partially painted electrodes). Due to the top electrode discontinuity, the local electric fields are position-sensitive throughout the sample and concentrated near the electrode edge. Under the macroscopic field application, the maximum domain textures are quantitatively calculated, and the local electric field directions are inferred in all scanned pixels. The results demonstrate that the domain switching behavior is orientation-dependent and spatially dependent across the whole partial-electrode samples. Specifically, in the active region (between electrodes), the domain reorientation is more homogeneous; in the passive region (outside the fully electroded region), the domain orientation is inhomogeneous. More specifically, due to the electric field concentration near the electrode edge, the domain reorientation is enhanced, resulting in higher domain texture strength. For the Nb-PZT 53/47 (near MPB) partial-electrode sample, the orientation-dependent phase transitions are also amplified. Complementing to the results from *in situ* high-energy XRD experiments, finite element analysis conducted in this work predicts the spatially dependent inhomogeneous electric field distribution in both lead-based and lead-free partial-electrode samples, showing a good correlation with the experimentally inferred local electric field directions in scanned pixels.

This research systematically explores the position sensitive and orientation-dependent domain reorientation and phase transitions in multiple ferroelectric materials in response to inhomogeneous electric fields. The field concentration-amplified domain switching and phase transitions provide new insight to reassess the non-uniform electromechanical response near an electrode edge, which may facilitate MLCA degradation and fracture. Moreover, the experimental strategy using synchrotron-based *in situ* high-energy XRD with an area detector also presents

opportunities to probe angular-dependent and position-dependent microstructural changes in ferroelectric devices.

© Copyright 2020 by Jianwei Zhao

All Rights Reserved

Inhomogeneous Electric Field-Induced Domain Reorientation and Phase Transitions in
Ferroelectrics

by
Jianwei Zhao

A dissertation submitted to the Graduate Faculty of
North Carolina State University
in partial fulfillment of the
requirements for the degree of
Doctor of Philosophy

Materials Science and Engineering

Raleigh, North Carolina
2020

APPROVED BY:

Dr. Jacob Jones
Committee Chair

Dr. Elizabeth Dickey

Dr. Veronica Augustyn

Dr. Xiaoning Jiang

DEDICATION

To my wonderful family.

BIOGRAPHY

Jianwei Zhao was born and grew up in the Jilin province at northeastern China. After graduating from the Wuhan University of Technology in 2012, he sought an M.S.E. degree in Mechanical Engineering under the direction of Prof. Pankaj Mallick at the University of Michigan-Dearborn (UMD) and graduated in 2015. The incredible experience of utilizing various characterization instrument at UMD helped him decide to continue his research venture in material science. He began his Ph.D. career at North Carolina State University in 2016 under the advising of Prof. Jacob Jones. His projects have been kindly supported by the Center for Dielectrics and Piezoelectrics (CDP) to explore the effects of electric field-inhomogeneity on microstructural changes in ferroelectrics. He has attended seven synchrotron-based experiments at the Advanced Photon Source and joined multiple international conferences and workshops during his time as a graduate student.

ACKNOWLEDGMENTS

I truly thank Prof. Jacob Jones for being a terrific advisor in my Ph.D. venture. Thank you for the patient guidance in my research, critical advice in scientific communications, and generous supports in numerous conferences, workshops, and travels. I am brimming with gratitude for all the research opportunities he offered while conducting this work. Moreover, I sincerely appreciate Prof. Elizabeth Dickey for recruiting me to the department of Materials Science and Engineering at North Carolina State University and being a superb co-advisor in my project. Furthermore, I acknowledge my committee members: Prof. Jacob Jones, Prof. Elizabeth Dickey, Prof. Veronica Augustyn, and Prof. Xiaoning Jiang, for all kinds of research advisement in this journey.

I want to thank the present and previous members from Jones research group: Alexandra Henriques, Rachel Broughton, Younghwan Lee, Alexis Payne, Alex Hasin, Alexandria Cruz, Emily Molina, Madison Horgan, Patrick Edgington, Dr. Hanhan Zhou, Dr. Giovanni Esteves, Dr. Dong Hou, Dr. Alisa Paterson, Dr. Ching-Chang Chung, Dr. Deepika Saini, Dr. Brienne Johnson, Dr. Christopher Fancher. Thanks for being great friends and colleagues throughout the years that makes me feel close to home.

I would like to appreciate the delicate work from Stephen Funni and Caleb Mooney from Prof. Elizabeth Dickey's research group for performing the finite element analysis on ferroelectric partial-electrode samples and multiplayer ceramic actuators, respectively. Additionally, I appreciate Abinash Kumar from Prof. James LeBeau's research group for collaborations on characterization of lead-free based ferroelectric materials.

I gratefully acknowledge PI Ceramic GmbH, Germany, for providing ferroelectric samples to investigate in the research, including lead-based and lead-free monolithic ceramics and

multilayer ceramic actuators. I also appreciate the supply of undoped potassium sodium niobate ceramic from Prof. Barbara Malič's group in Jožef Stefan Institute, Slovenia.

I acknowledge all the supports from the Center for Dielectrics and Piezoelectrics (CDP), which is supported by the National Science Foundation under Grant Nos. IIP-1841453 and IIP-1841466. Moreover, I would like to acknowledge the use of Analytical Instrumentation Facility (AIF) at North Carolina State University, which is supported by the State of North Carolina and the National Science Foundation under the award No. ECCS-1542015. Many thanks to AIF staffs, Anna Lumpkin, Dr. Ching-Chang Chung, Robert Garcia, Chuck Mooney, And Fred Stevie. I also acknowledge the use of the Advanced Photon Source, a U.S. Department of Energy (DOE) Office of Science User Facility operated for the DOE Office of Science by Argonne National Laboratory under Contract No. DE-AC02-06CH11357. All the technical assistance and data discussion from Yang Ren, Longlong Fan, and Rick Spence, at Sector 11 is gratefully appreciated.

TABLE OF CONTENTS

LIST OF TABLES	ix
LIST OF FIGURES	xii
Chapter 1: Background and Introduction.....	1
1.1. Dielectrics, Piezoelectrics, and Ferroelectrics	1
1.2. Ferroelectric Materials.....	5
1.2.1. Lead-based Ferroelectric Materials.....	5
1.2.2. Lead-free Ferroelectric Materials	6
1.3. Characterization Methods	8
1.4. Motivation of the Research.....	10
Chapter 2: <i>In Situ</i> Experimental Setup and Data Analysis	14
2.1. Overview.....	14
2.2. Samples	14
2.3. Electrode Configuration and Scan Patterns	16
2.4. Experiment Description	18
2.5. Data Reduction	21
2.6. Peak Fitting Analysis	25
Chapter 3: Homogeneous Electric Field-Induced Material Behaviors.....	26
3.1. Overview	26
3.2. Nb-PZT-based Materials.....	26
3.2.1. Nb-PZT 50/50	26
3.2.2. Nb-PZT 53/47	29
3.2.3. Nb-PZT 56/44	37

3.3. KNN-based Materials	40
3.3.1. Undoped KNN	40
3.3.2. Doped KNN	44
3.4. Summary	46
Chapter 4: Inhomogeneous Electric Field-Induced Material Behaviors.....	49
4.1. Overview.....	49
4.2. Whole Bar Scan	49
4.2.1. Nb-PZT-based Materials.....	50
4.2.2. KNN-based Materials	56
4.2.3. Discussion.....	62
4.3. Electrode Edge Scan	69
4.3.1. Nb-PZT-based Materials.....	71
4.3.2. KNN-based Materials	76
4.3.3. Discussion.....	78
4.4. Summary	82
Chapter 5: Conclusions and Future Work	84
5.1. Conclusions.....	84
5.2. Suggestions for Future Work.....	87
REFERENCES.....	89
APPENDICES	104
Appendix A: Image Reduction of Using FIT2D	105
Appendix B: Peak Fitting in LIPRAS.....	118
Appendix C: Supplementary Figures.....	126

Appendix D: Supplementary Tables..... 140

Appendix E: Reprint Permissions..... 146

LIST OF TABLES

Table 1 Specifications of beamline 11-ID-C.....	18
Table 2 Lattice parameters in undoped KNN material in the virgin state with respect to the orthorhombic and pseudo-monoclinic frames, assuming $a_M = c_M$	41
Table 3 Indices for 220 reflections with respect to the orthorhombic and pseudo-monoclinic frames for undoped KNN material in the virgin state.	41
Table 4 Under the macroscopic electric field of 3 kV/mm, the calculated maximum domain texture strength (in tetragonal, rhombohedral) and maximum fraction of domain interchange (in orthorhombic) in different sample geometries.	80
Table 5 Summary of the maximum 002 domain texture strength and experimentally inferred local electric field direction in each scanned pixel for Nb-PZT 50/50 partial-electrode sample with the whole bar scan pattern under the application of macroscopic electric field 3kV/mm.	140
Table 6 Summary of the maximum 002 domain texture strength and experimentally inferred local electric field direction in each scanned pixel for Nb-PZT 53/47 partial-electrode sample with the whole bar scan pattern under the application of macroscopic electric field 3kV/mm.	140
Table 7 Summary of the maximum 111 domain texture strength and experimentally inferred local electric field direction in each scanned pixel for Nb-PZT 56/44 partial-electrode sample with the whole bar scan pattern under the application of macroscopic electric field 3kV/mm.	141
Table 8 Summary of the maximum 002 domain texture strength and experimentally inferred local electric field direction in each scanned pixel for doped KNN	

partial-electrode sample with the whole bar scan pattern under the application of macroscopic electric field 3kV/mm.	141
Table 9 Summary of fraction of domain interchange and experimentally inferred local electric field direction in each scanned pixel for undoped KNN partial-electrode sample with the whole bar scan pattern under the application of macroscopic electric field 3kV/mm.....	142
Table 10 Summary of 002 domain texture strength and experimentally inferred local electric field direction in each scanned pixel for Nb-PZT 50/50 partial-electrode sample with the electrode edge scan pattern under the application of macroscopic electric field 3kV/mm.....	143
Table 11 Summary of 002 domain texture strength and experimentally inferred local electric field direction in each scanned pixel for Nb-PZT 53/47 partial-electrode sample with the electrode edge scan pattern under the application of macroscopic electric field 3kV/mm.	143
Table 12 Summary of 111 domain texture strength and experimentally inferred local electric field direction in each scanned pixel for Nb-PZT 56/44 partial-electrode sample with the electrode edge scan pattern under the application of macroscopic electric field 3kV/mm.....	144
Table 13 Summary of fraction of domain interchange and experimentally inferred local electric field direction in each scanned pixel for undoped KNN partial-electrode sample with the electrode edge scan pattern under the application of macroscopic electric field 3kV/mm.....	144

Table 14 Summary of 002 domain texture strength and experimentally inferred local electric field direction in each scanned pixel for doped KNN partial-electrode sample with the electrode edge scan pattern under the application of macroscopic electric field 3kV/mm.....	145
---	-----

LIST OF FIGURES

- Figure 1-1** Possible polarization directions in (a) tetragonal, (b) orthorhombic, and (c) rhombohedral relative to the pseudo-cubic unit cell 2
- Figure 1-2** Changes in primitive-cell lattice parameters and anomalies in relative permittivity during the sequence of phase transitions in BaTiO₃ with crystal structure illustrations of cubic, tetragonal, orthorhombic, and rhombohedral phases. Reprinted with permission from M. Acosta *et al.* Applied Physics Reviews, vol. 4, no. 4. American Institute of Physics Inc., 01-Dec-2017. 3
- Figure 1-3** Phase diagram of PbZrO₃-PbTiO₃ solid solutions showing the MPB in the middle of the diagram separating tetragonal and rhombohedral ferroelectric phases. The subscripts A and F represent for antiferroelectric and ferroelectric phases, and the letters C, T, O, and R stand for cubic, tetragonal, orthorhombic, and rhombohedral phases. Reprinted with permission from D. Damjanovic. *Reports Prog. Phys.*, vol. 61, no. 9, p. 1267, 1998..... 6
- Figure 1-4** Phase diagram of KNbO₃-NaNbO₃ solid solutions. Reprinted with permission from Li, Jing-Feng, *et al.* Journal of the American Ceramic Society 96.12 (2013): 3677-3696..... 8
- Figure 1-5** Two dimensional FEA results of inhomogeneous (a) electric field [kV/mm], (b) strain, and (c) principal stress [Pa] distributions around an interdigitated electrode edge in a KNN-based MLCA under the application of 3 kV/mm. The interdigitated electrode spacing is 53 μm. Courtesy of Caleb Mooney for the FEA work. 12

Figure 2-1 X-ray scan patterns for the synchrotron-based experiments in beamline 11-ID-C, showing the full-electrode sample with (a) center scan, and the partially electroded sample with (b) whole bar scan, and (c) electrode edge scan.....	17
Figure 2-2 Schematics of the synchrotron-based experimental setup in beamline 11-ID-C, APS, using the piezoelectric (a) full-electrode sample, and (b) partial-electrode sample.....	19
Figure 2-3 Layout for the custom sample stage and the 2D area detector in beamline 11-ID-C, APS.	20
Figure 2-4 The custom sample stage with connections to a HV cable and a grounding wire. The piezoceramic sample is placed in the Kapton tube.	21
Figure 2-5 (a) The divided sectors in a 2D XRD pattern, and (b) integrated 1D plots from different azimuthal sectors for the tetragonal phase commercial PZT-EC-65 ferroelectric sample with the full-electrode configuration at 3 kV/mm.....	23
Figure 2-6 Peak intensities as a function of electric field amplitude for the tetragonal phase commercial PZT-EC-65 sample with the full-electrode configuration at (a) 0°, and (b) 90° azimuthal angles.	24
Figure 2-7 Peak intensities as a function of azimuthal angle φ for the tetragonal phase commercial PZT- EC-65 sample with the full-electrode configuration in (a) the virgin state, and (b) 3 kV/mm.	24
Figure 3-1 Peak intensities as a function of azimuthal angle (φ) for the tetragonal phase Nb-PZT 50/50 sample with the full-electrode configuration in (a) the virgin state and (b) 3 kV/mm.	27

Figure 3-2 The degree of 002 domain alignment of the tetragonal Nb-PZT 50/50 sample with the full-electrode configuration at multiple electric field amplitudes along all azimuthal angles.	28
Figure 3-3 Peak intensities as a function of azimuthal angle (φ) for the Nb-PZT 53/47 sample with the full-electrode configuration in (a) the virgin state, (b) 3 kV/mm, and (c) 7 kV/mm.	29
Figure 3-4 Peak intensities as a function of electric field amplitude for the Nb-PZT 53/47 sample with the full-electrode configuration at the (a) 0°, (b) 45°, and (c) 90° azimuthal angles.	31
Figure 3-5 The degree of 002 domain alignment of the tetragonal phase Nb-PZT 53/47 sample with the full-electrode configuration as a function of electric field amplitude in the 0° and 90° azimuthal angles.	32
Figure 3-6 In the virgin state, the possible representative tetragonal unit cell orientations in Nb-PZT 53/47 in (a) and (b); under the application of an electric field, the elongated tetragonal unit cells in (c), and the distorted rhombohedral-like unit cells in (d).	34
Figure 3-7 Orientation-dependent field-induced lattice strain in Nb-PZT 50/50 and Nb-PZT 53/47 at macroscopic electric field of 3 kV/mm.	35
Figure 3-8 Inverse pole figure of a multi-phase simulation of tetragonal and rhombohedral grains, and their resulting phase selection based on variant selection when an electric field is applied along the [001]. Reproduced from Esteves <i>et al. Acta Mater.</i> , vol. 132, pp. 96–105, 2017.	36

Figure 3-9 Peak intensities as a function of azimuthal angle (φ) for the rhombohedral phase Nb-PZT 56/44 sample with the full-electrode configuration in (a) the virgin state and (b) 3 kV/mm.	38
Figure 3-10 The degree of 111 domain alignment of the rhombohedral phase Nb-PZT 56/44 sample with full-electrode configuration at multiple electric field amplitudes along all azimuthal angles.....	39
Figure 3-11 Spontaneous polarization directions (P_S) in undoped KNN (a) orthorhombic unit cell and (b) pseudo-monoclinic unit cell.....	41
Figure 3-12 Peak intensities as a function of azimuthal angle (φ) for the pseudo-monoclinic (orthorhombic) phase, undoped KNN sample with the full-electrode configuration in (a) the virgin state and (b) 3 kV/mm.	42
Figure 3-13 The fraction of domain interchange in the pseudo-monoclinic (orthorhombic) phase, undoped KNN sample with the full-electrode configuration as a function of electric field amplitude along all azimuthal angles.	44
Figure 3-14 Peak intensities as a function of azimuthal angle (φ) for the tetragonal phase, doped KNN sample with the full-electrode configuration in (a) the virgin state and (b) 3 kV/mm.	45
Figure 3-15 The degree of 002 domain alignment of the tetragonal phase, doped KNN sample with the full-electrode configuration at multiple electric fields along all azimuthal angles.....	46
Figure 4-1 The whole bar scan pattern in ferroelectric partial-electrode samples with labeled pixels.	50

- Figure 4-2** Peak intensities as a function of azimuthal angle (φ) for P_{2-10} , P_{1-5} , and P_{1-1} in the tetragonal phase Nb-PZT 50/50 partial-electrode sample with the whole bar scan pattern. Plots (a), (b), (c) present the peak intensities in the virgin state, and (d), (e), (f) show the interchanged intensities at 3 kV/mm for P_{2-10} , P_{1-5} , and P_{1-1} , respectively..... 52
- Figure 4-3** The degree of 002 domain alignment (MRD) of representative pixels P_{2-10} , P_{1-5} , and P_{1-1} in the tetragonal phase Nb-PZT 50/50 partial-electrode sample with the whole bar scan pattern at 3 kV/mm. 54
- Figure 4-4** Under the application of 3 kV/mm, the calculated maximum domain texture strength in each scanned pixel for the partial-electrode samples with lead-based composition of (a) Nb-PZT 50/50, (b) Nb-PZT 53/47, and (c) Nb-PZT 56/44. 55
- Figure 4-5** Peak intensities as a function of azimuthal angle (φ) for P_{2-10} , P_{1-5} , and P_{1-1} in the pseudo-monoclinic (orthorhombic) phase, undoped KNN partial-electrode sample with the whole bar scan pattern. Plots (a), (b), (c) present the peak intensities in the virgin state, and (d), (e), (f) show the interchanged intensities at 3 kV/mm for P_{2-10} , P_{1-5} , and P_{1-1} , respectively. 57
- Figure 4-6** Fraction of domain interchange in representative pixels (a) P_{2-10} , (b) P_{1-5} , and (c) P_{1-1} in the pseudo-monoclinic (orthorhombic) phase, undoped KNN partial-electrode sample with the whole bar scan pattern at 3 kV/mm. 60
- Figure 4-7** Under the application of 3 kV/mm, the calculated maximum fraction of domain interchange (a) $n_{022-202}$, and (b) $n_{220-202}$, in each scanned pixel for the pseudo-monoclinic (orthorhombic) phase, undoped KNN partial-electrode sample with the whole bar scan pattern..... 61

- Figure 4-8** Under the application of 3 kV/mm, the calculated maximum 002 domain texture strength in each scanned pixel for the tetragonal phase, doped KNN partial-electrode sample with the whole bar scan pattern. 62
- Figure 4-9** FEA results of simulated local electric field vector for each pixel in a (a) Nb-PZT-based, and a (b) KNN-based partial-electrode sample. The macroscopic electric field is set as 3 kV/mm in the simulation. Courtesy of Stephen Funni for the FEA work. 64
- Figure 4-10** Correlations between the simulated electric field amplitudes from FEA and (a) degree of domain alignment in tetragonal and rhombohedral phase materials, and (b) fraction of domain interchange in orthorhombic phase material. (Note: Pixels with high simulated electric field values are not used in correlations) 67
- Figure 4-11** Correlations between the experimentally inferred electric field directions and simulated electric field directions from FEA in (a) Nb-PZT-based, and (b) KNN-based partial-electrode samples. (Note: Pixels exhibiting extremely low domain reorientation are not used in correlations) 68
- Figure 4-12** The electrode edge scan pattern used in ferroelectric partial-electrode samples with labeled pixels. 70
- Figure 4-13** Under the application of 3 kV/mm, the calculated maximum degree of 002 domain alignment in the electrode termination region of the tetragonal phase Nb-PZT 50/50 partial-electrode sample..... 71
- Figure 4-14** Under the application of 3 kV/mm, the calculated maximum degree of 111 domain alignment in the electrode termination region of the rhombohedral phase Nb-PZT 56/44 partial-electrode sample. 72

Figure 4-15 Peak intensities as a function of azimuthal angle (φ) for representative pixels P_{4-5} and P_{1-4} in the Nb-PZT 53/47 partial-electrode sample with the electrode edge scan pattern. Plots (a) and (b) show the peak intensities in the virgin state, (c) and (d) show the interchanged intensities at a macroscopic electric field of 3 kV/mm, (e) and (f) show the field-dependent intensity interchanges along the 45° azimuthal angle, for P_{4-5} and P_{1-4} , respectively.	74
Figure 4-16 Under the application of 3 kV/mm, the calculated maximum degree of 002 domain alignment in the electrode termination region of the tetragonal phase Nb-PZT 53/47 partial-electrode sample.....	75
Figure 4-17 Under the application of 3 kV/mm, the calculated maximum fraction of domain interchange (a) $n_{022-202}$, and (b) $n_{220-202}$, in the electrode termination region of the pseudo-monoclinic (orthorhombic) phase, undoped KNN partial-electrode sample.	77
Figure 4-18 Under the application of 3 kV/mm, the degree of 002 domain alignment in the electrode termination region of the tetragonal phase, doped KNN partial-electrode sample.	78
Figure S-1 Program interface of FIT2D.....	106
Figure S-2 FIT2D software interface displays the collected 2D Debye-Scherrer rings from standard calibrant CeO_2	109
Figure S-3 FIT2D software interface displays the fitted Debye-Scherrer rings for the standard calibrant CeO_2	110
Figure S-4 FIT2D software interface displays the completed experimental geometry calibration with the appropriate parameters refined.....	111

- Figure S-5** XRD plots integrated from each azimuthal sector from the tetragonal phase commercial PZT-EC-65 sample with the full-electrode configuration. 114
- Figure S-6** Peak intensity changes in the (a) 0° , (b) 30° , (c) 60° , and (d) 90° azimuthal sector as a function of electric field amplitude, for the tetragonal phase commercial PZT-EC-65 material. 116
- Figure S-7** Representative Pseudo-Voigt profile functions with different mixing parameter values. These functions set $x_0 = 0$ and $H_K = 1$ 119
- Figure S-8** Peak fitting analysis on 002 and 200 reflections parallel to the macroscopic electric field direction in the tetragonal phase Nb-PZT 50/50 full-electrode sample at 3 kV/mm, using (a) Pseudo-Voigt, and (b) asymmetric Pearson VII profile functions. 123
- Figure S-9** Peak fitting analysis on 111 and $11\bar{1}$ reflections parallel to the macroscopic electric field direction in the rhombohedral phase Nb-PZT 56/44 full-electrode sample at 3 kV/mm, using (a) Pseudo-Voigt, and (b) asymmetric Pearson VII profile functions. 124
- Figure S-10** Peak fitting analysis on 202 , 022 , and 220 reflections parallel to the macroscopic electric field direction in the pseudo-monoclinic (orthorhombic) phase undoped KNN full-electrode sample at 3 kV/mm, using (a) Pseudo-Voigt, and (b) asymmetric Pearson VII profile functions. 125
- Figure S-11** Peak intensities as a function of azimuthal angle (φ) for P_{2-10} , P_{1-5} , and P_{1-1} in the Nb-PZT 53/47 partial-electrode sample with the whole bar scan pattern. Plots (a), (b), (c) present the peak intensities in the virgin state, and (d), (e), (f)

show the interchanged intensities at 3 kV/mm for P ₂₋₁₀ , P ₁₋₅ , and P ₁₋₁ , respectively.	126
Figure S-12 The degree of 002 domain alignment (MRD) of representative pixels P ₂₋₁₀ , P ₁₋₅ , and P ₁₋₁ in the Nb-PZT 53/47 partial-electrode sample with the whole bar scan pattern at 3 kV/mm.	127
Figure S-13 Peak intensities as a function of azimuthal angle (φ) for P ₂₋₁₀ , P ₁₋₅ , and P ₁₋₁ in the Nb-PZT 56/44 partial-electrode sample with the whole bar scan pattern. Plots (a), (b), (c) present the peak intensities in the virgin state, and (d), (e), (f) show the interchanged intensities at 3 kV/mm for P ₂₋₁₀ , P ₁₋₅ , and P ₁₋₁ , respectively.	128
Figure S-14 The degree of 111 domain alignment (MRD) of representative pixels P ₂₋₁₀ , P ₁₋₅ , and P ₁₋₁ in the Nb-PZT 56/44 partial-electrode sample with the whole bar scan pattern at 3 kV/mm.	129
Figure S-15 Peak intensities as a function of azimuthal angle (φ) for P ₂₋₁₀ , P ₁₋₅ , and P ₁₋₁ in the doped KNN partial-electrode sample with the whole bar scan pattern. Plots (a), (b), (c) present the peak intensities in the virgin state, and (d), (e), (f) show the interchanged intensities at 3 kV/mm for P ₂₋₁₀ , P ₁₋₅ , and P ₁₋₁ , respectively.	130
Figure S-16 The degree of 002 domain alignment (MRD) of representative pixels P ₂₋₁₀ , P ₁₋₅ , and P ₁₋₁ in the doped KNN partial-electrode sample with the whole bar scan pattern at 3 kV/mm.	131
Figure S-17 Peak intensities as a function of azimuthal angle (φ) for P ₄₋₅ , P ₁₋₃ , and P ₁₋₁ in the Nb-PZT 50/50 partial-electrode sample with the electrode edge scan	

pattern. Plots (a), (b), (c) present the peak intensities in the virgin state, and (d), (e), (f) show the interchanged intensities at 3 kV/mm for P ₄₋₅ , P ₁₋₃ , and P ₁₋₁ , respectively.	132
Figure S-18 The degree of 002 domain alignment (MRD) of representative pixels P ₄₋₅ , P ₁₋₃ , and P ₁₋₁ in the Nb-PZT 50/50 partial-electrode sample with the electrode edge scan pattern at 3 kV/mm.	133
Figure S-19 Peak intensities as a function of azimuthal angle (φ) for P ₄₋₅ , P ₁₋₃ , and P ₁₋₁ in the Nb-PZT 56/44 partial-electrode sample with the electrode edge scan pattern. Plots (a), (b), (c) present the peak intensities in the virgin state, and (d), (e), (f) show the interchanged intensities at 3 kV/mm for P ₄₋₅ , P ₁₋₃ , and P ₁₋₁ , respectively.	134
Figure S-20 The degree of 111 domain alignment (MRD) of representative pixels P ₄₋₅ , P ₁₋₃ , and P ₁₋₁ in the Nb-PZT 56/44 partial-electrode sample with the electrode edge scan pattern at 3 kV/mm.	135
Figure S-21 Peak intensities as a function of azimuthal angle (φ) for P ₃₋₅ , P ₁₋₄ , and P ₁₋₁ in the undoped KNN partial-electrode sample with the electrode edge scan pattern. Plots (a), (b), (c) present the peak intensities in the virgin state, and (d), (e), (f) show the interchanged intensities at 3 kV/mm for P ₃₋₅ , P ₁₋₄ , and P ₁₋₁ , respectively.	136
Figure S-22 Fraction of domain interchange in (a) P ₃₋₅ , (b) P ₁₋₄ , and (c) P ₁₋₁ in the pseudo-monoclinic (orthorhombic) phase undoped KNN partial-electrode sample with the electrode edge scan pattern at 3 kV/mm.	137

Figure S-23 Peak intensities as a function of azimuthal angle (φ) for P₄₋₅, P₁₋₃, and P₁₋₁ in the doped KNN partial-electrode sample with the electrode edge scan pattern. Plots (a), (b), (c) present the peak intensities in the virgin state, and (d), (e), (f) show the interchanged intensities at 3 kV/mm for P₄₋₅, P₁₋₃, and P₁₋₁, respectively. 138

Figure S-24 The degree of 002 domain alignment (MRD) of representative pixels P₄₋₅, P₁₋₃, and P₁₋₁ in the doped KNN partial-electrode sample with the electrode edge scan pattern at 3 kV/mm. 139

Chapter 1: Background and Introduction

1.1. Dielectrics, Piezoelectrics, and Ferroelectrics

Dielectrics or dielectric materials are electrical insulators or nonconductors, which exhibit or can be made to exhibit electric dipole moments, and can be used in capacitors [1]. Under the application of an external electric field, the dipole moments in a dielectric material can be reoriented to align with the field direction, resulting in electric charges on the capacitor surface. This process is referred to as polarization and the quantity of charge per unit area stored on the capacitor is called surface charge density or dielectric displacement [1], [2]. For a dielectric material, both dielectric displacement (D) and field-induced polarization (P) are related to the applied electric field (E) as illustrated in Equations (1) and (2) [1], [3]:

$$D_i = \epsilon_0 E_i + P_i \quad \text{Equation (1)}$$

$$P_i = \epsilon_0 (\epsilon_r - 1) E_i \quad \text{Equation (2)}$$

where, ϵ_0 is the permittivity of a vacuum space that is a constant in value of 8.85×10^{-12} F/m, and ϵ_r is the relative permittivity of the dielectric material.

Piezoelectric materials are a sub-category of dielectrics that have non-centrosymmetric crystal structures. Piezoelectric materials were first discovered by the Curie brothers in 19th century and have since been extensively investigated [4], [5]. Electric charges are generated in piezoelectric materials in response to a mechanical stress, which is referred to as the direct piezoelectric effect. On the other hand, a mechanical deformation can be induced in piezoelectric materials under the application of an electric field, which is referred to as the converse piezoelectric effect. The direct and converse piezoelectric effects are illustrated in Equations (3) and (4), respectively [3]:

$$D_i = d_{ijk}T_{jk} \quad \text{Equation (3)}$$

$$S_{jk} = d_{ijk}E_i \quad \text{Equation (4)}$$

where, T_{jk} is the applied mechanical stress, S_{jk} is the strain generated in response to the applied electric field, E_i , and d_{ijk} represents the piezoelectric tensor. Due to these complementary effects, piezoelectric materials are commonly used in applications converting mechanical energy into electrical energy and vice versa.

Within the category of piezoelectrics, there are certain materials referred to as ferroelectrics, which were first discovered in 1920 by Joseph Valasek and reported in 1921 [6]. Ferroelectric materials, which are often compared with ferromagnetic materials, have permanent dipoles and exhibit spontaneous polarizations in the absence of an external electric field. The direction of spontaneous polarization in a ferroelectric varies depending on the crystallographic structure of the material. As shown in Figure 1-1, Jones demonstrated that, in a tetragonal phase ferroelectric, the spontaneous polarizations are parallel to the $\langle h00 \rangle$ directions; in an orthorhombic phase ferroelectric, the spontaneous polarizations are parallel to the $\langle hh0 \rangle$ directions; and in a rhombohedral phase ferroelectric, the spontaneous polarizations are parallel along the $\langle hhh \rangle$ directions [7].

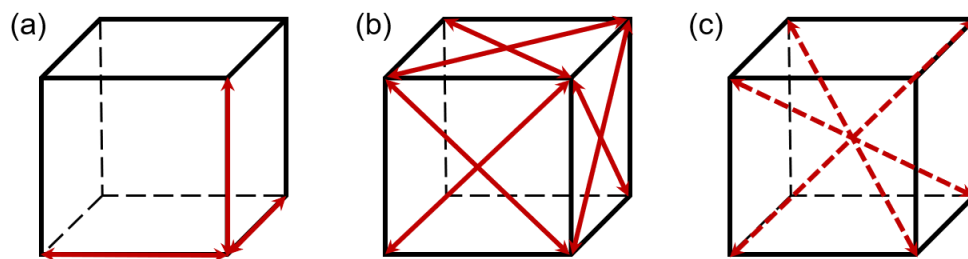


Figure 1-1 Possible polarization directions in (a) tetragonal, (b) orthorhombic, and (c) rhombohedral relative to the pseudo-cubic unit cell.

In a ferroelectric material, there are regions called domains, within which the spontaneous polarizations are commonly aligned in a uniform direction. When a ferroelectric material is cooled from a high temperature, a transition from the paraelectric phase to the ferroelectric phase occurs at the Curie point (T_c) and the spontaneous polarizations develop subsequently in the corresponding phase. During the phase transition, domains are formed in order to minimize the free energy [8], [9]. As shown in Figure 1-2, for example, barium titanate (BaTiO_3), one of the most common ferroelectric materials with a perovskite structure, undergoes a sequence of phase transitions from cubic ($Pm\bar{3}m$), to tetragonal ($P4mm$), to orthorhombic ($Amm2$), and then to rhombohedral ($R3m$) phase with decreasing temperature from the Curie point [10].

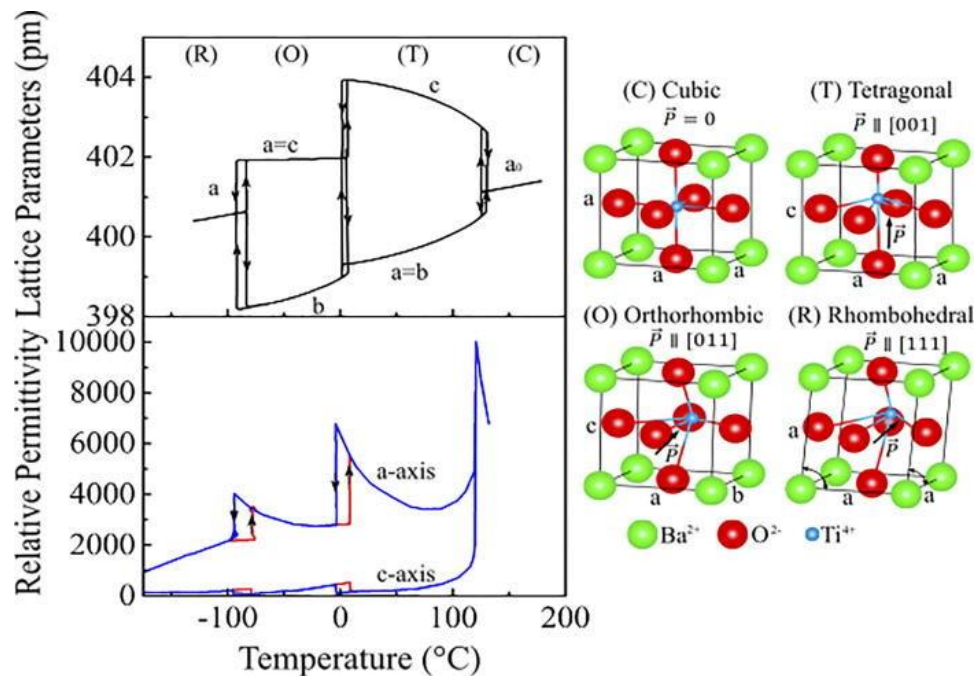


Figure 1-2 Changes in primitive-cell lattice parameters and anomalies in relative permittivity during the sequence of phase transitions in BaTiO_3 with crystal structure illustrations of cubic, tetragonal, orthorhombic, and rhombohedral phases. Reprinted with permission from M. Acosta *et al.* Applied Physics Reviews, vol. 4, no. 4. American Institute of Physics Inc., 01-Dec-2017.

The domains in a ferroelectric are separated by domain walls, which are the transition areas where the polarization directions in adjacent domains change. Since the polarization directions vary for different phases, they can be categorized as 180° ferroelectric domain walls and non- 180° ferroelectric/ferroelastic domain walls. For example, in the tetragonal phase, there are 180° and 90° domain walls; in the orthorhombic phase, there are 180° , 120° , 90° , and 60° domain walls; in the rhombohedral phase, there are 180° , 109° , and 71° domain walls. Domain sizes in ferroelectric materials are generally in the range of a few nanometers to tens of micrometers [11]. A typical 180° domain wall width is on the order of one lattice parameter (2 or 3 Å), whereas a non- 180° domain wall may exhibit a smaller width. The width of both 180° and non- 180° domain walls vary with temperature and crystal purity [2].

In the virgin state (electrically unpoled state) of a polycrystalline ferroelectric material, the domains are randomly oriented in all directions. Under the application of an external electric field with an amplitude above the coercive field (E_C) of the material, domains start to reorient to align with the applied field direction, resulting in an increase of the net polarization. With further increasing the electric field to higher magnitudes ($\gg E_C$), the polarization in the ferroelectric material will saturate. This process is referred to as poling, which results in domain reorientation in the ferroelectric material. After removing the applied electric field, a remnant net polarization remains with a majority of the domains still aligned in a uniform direction.

When a ferroelectric material is subjected to an electrical load, there are two main contributions to its electromechanical response, i.e. field-induced macroscopic strain [12], [13]: (1) an intrinsic contribution that results from the electric field-induced lattice distortion [13], [14] and (2) an extrinsic contribution that originates from other factors such as domain reorientation [15]–[18]. It is worth noting that phase transitions can occur in ferroelectric materials of particular

compositions under the application of electric fields, contributing to the macroscopic strain [15], [19]–[22]. Specifically, the field-induced strain contribution from a phase transition is considered as volumetric [19].

1.2. Ferroelectric Materials

1.2.1. Lead-based Ferroelectric Materials

To date, ferroelectrics have been widely developed for use of commercialized applications, such as transducers, sensors, and actuators [23], [24]. The dominant material for the ferroelectric applications is lead zirconate titanate, $\text{Pb}[\text{Zr}_x\text{Ti}_{1-x}]\text{O}_3$ (PZT), because of its superior dielectric and piezoelectric properties [24]–[26]. Over the decades, PZT-based materials have been extensively studied to further enhance their piezoelectric performance [27]–[31]. It is worth noting that PZT-based ferroelectric materials exhibit improved properties, e.g., dielectric constants, piezoelectric constants, and electromechanical coupling coefficients, when the composition approaches the morphotropic phase boundary (MPB), a region where two phases can coexist stably in the material [8], [32]. Figure 1-3 presents a conventional binary phase diagram for the PZT system [11]. Near the MPB ($x \sim 0.52$) of PZT-based ferroelectrics at room temperature, electric field-induced phase transitions can occur between co-existing phases or phases near the limit of their stability. For example, field-induced changes in the phase fractions have been observed in PZT compositions containing both tetragonal ($P4mm$) and monoclinic (Cm) phases [22], and tetragonal ($P4mm$) and rhombohedral ($R3m$) phases [33]–[35].

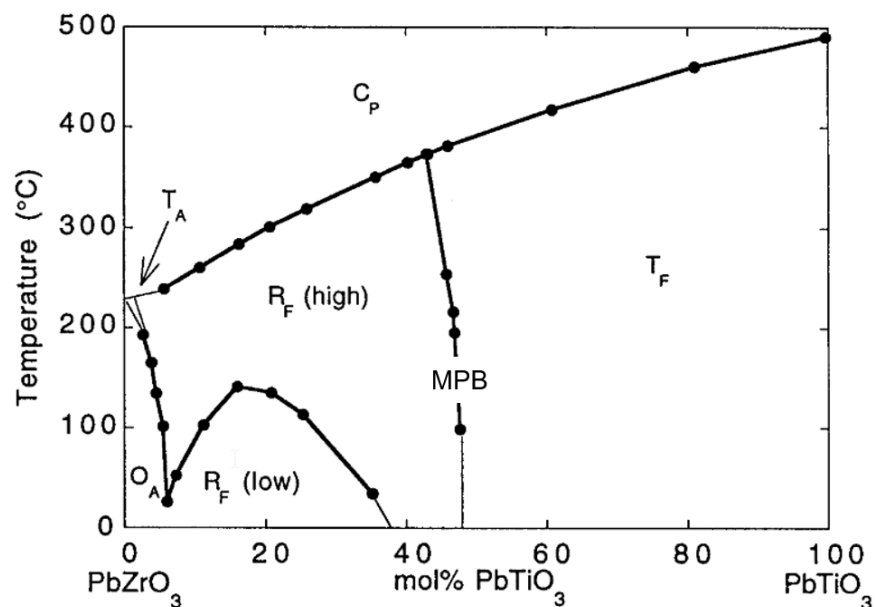


Figure 1-3 Phase diagram of PbZrO₃-PbTiO₃ solid solutions showing the MPB in the middle of the diagram separating tetragonal and rhombohedral ferroelectric phases. The subscripts A and F represent for antiferroelectric and ferroelectric phases, and the letters C, T, O, and R stand for cubic, tetragonal, orthorhombic, and rhombohedral phases. Reprinted with permission from D. Damjanovic. *Reports Prog. Phys.*, vol. 61, no. 9, p. 1267, 1998.

1.2.2. Lead-free Ferroelectric Materials

To develop socially sustainable and eco-friendly technologies, the European Union has passed the Restriction of Hazardous Substances (RoHS) directive in 2003 and has been leading efforts to investigate lead-free ferroelectrics [36]. Over decades, many lead-free material systems, such as [xBa(Zr,Ti)O₃-(1-x)(Ba,Ca)TiO₃] (BZT-BCT) [37]–[40], [xNa_{0.5}Bi_{0.5}TiO₃-(1-x)BaTiO₃] (NBT-BT) [41]–[44], chemically modified (K_xNa_{1-x})NbO₃ (KNN) [45]–[49], etc., have been extensively investigated for various ferroelectric applications [50]. Since Saito *et al.* reported a large piezoelectric coefficient d_{33} of 416 pC/N comparable with lead-based ferroelectrics [51], KNN-based materials have been considered as one of the most promising alternatives for PZT-based ceramics. The piezoelectric coefficient in an undoped KNN system is optimized when the composition has K/Na ratio of approximately one, i.e. K_{0.5}Na_{0.5}NbO₃ [52]. As shown in the

phase diagram in Figure 1-4, with increasing temperature, the composition $\text{K}_{0.5}\text{Na}_{0.5}\text{NbO}_3$ undergoes a rhombohedral ($R3m$) - orthorhombic ($Amm2$) phase transition around -123°C , an orthorhombic ($Amm2$) - tetragonal ($P4mm$) phase transition at approximately 210°C , and becomes a paraelectric cubic ($Pm\bar{3}m$) phase upon its Curie point around 410°C [52], [53]. Thus, $\text{K}_{0.5}\text{Na}_{0.5}\text{NbO}_3$ has a single orthorhombic phase at room temperature. It is widely accepted that the formation of phase boundaries through chemical modifications can enhance piezoelectric properties of ferroelectric materials because it facilitates polarization rotations induced by the structural instability [54], [55]. In general, For example, Wu *et al.* summarized that the use of lithium (Li^+), antimony (Sb^{5+}), tantalum (Ta^{5+}) ions, etc., as dopants in the KNN system can dramatically lower the orthorhombic-tetragonal phase transition to occur at or near room temperature [56]. In this work, both lead-free undoped $\text{K}_{0.5}\text{Na}_{0.5}\text{NbO}_3$ and (Li, Ta, Mn)-doped $\text{K}_{0.5}\text{Na}_{0.5}\text{NbO}_3$ are studied under the application of electric field for comparison with the lead-based PZT ferroelectric materials.

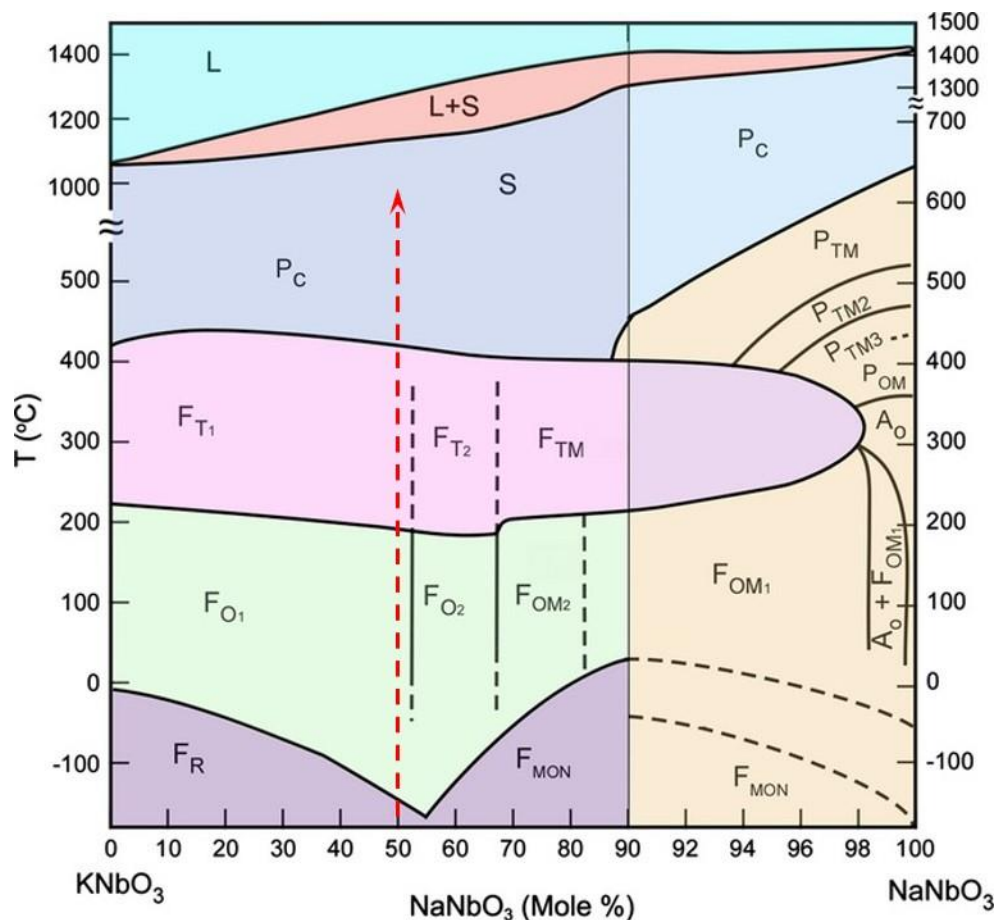


Figure 1-4 Phase diagram of KNbO₃-NaNbO₃ solid solutions. Reprinted with permission from Li, Jing-Feng, *et al.* Journal of the American Ceramic Society 96.12 (2013): 3677-3696.

1.3. Characterization Methods

Electric field-induced microstructural changes in ferroelectrics can be probed in multiple characterization instruments, such as transmission electron microscopy (TEM) [57]–[59], atomic force microscopy (AFM) [60]–[63], piezoresponse force microscopy (PFM) [64]–[66], Raman spectroscopy [67]–[69], etc. Another important and powerful approach is x-ray diffraction (XRD) that has been broadly exploited for investigating material behaviors in polycrystalline ferroelectrics in response to electric field. In the simplest construction, a laboratory-scale powder diffractometer can be employed in conjunction with an *in situ* electric field cell [33], [70]–[72].

Under the application of electric fields, XRD helps investigate the microstructural changes in ferroelectrics. This is done through the investigation of lattice distortions, domain reorientation, and phase transitions, with respect to various angles to the applied field direction and different field amplitudes. Specifically, the intrinsic lattice distortion can be studied by observing peak position shifts in 2θ angle; domain reorientation can be probed by measuring intensity changes between degenerate reflections corresponding to the specific polarization directions in ferroelectric phases; and phase transitions can be investigated by observing peak position and intensity changes as well as appearance or disappearance of certain reflections [22], [73]–[75].

A laboratory-based X-ray diffractometer often uses a point detector or a linear detector in Bragg-Brentano geometry (reflection geometry), hence the *in situ* experiments conducted with applied electric field are only sensitive to scattering vectors parallel to the field direction. The collected XRD patterns at an applied field provide information about the d-spacing changes (i.e., elastic strains) and preferred orientation (i.e., domain fraction changes) only in the direction parallel to the electric field. However, as demonstrated by Jones *et al.*, the preferred orientation induced by ferroelectric/ferroelastic domain reorientation produces a crystallographic texture that often necessitates a more rigorous texture characterization approach [76]. Most of the polycrystalline ferroelectric ceramics investigated via these techniques are initially randomly oriented and exhibit an electric field-induced fiber symmetry (i.e., transversely isotropic) after electrical poling. To completely describe the texture, an entire orientation distribution function (ODF) that describes the relative probability of all crystallographic orientations in 3-dimensional Euler space can be calculated [77]–[79]. However, due to the sample symmetry, it is not necessary to calculate an entire ODF. At minimum, however, characterizing domain texture in these

materials often relies on integrating more information than is available in a single diffraction pattern [80], [81].

Synchrotron-based XRD is an increasingly common alternative to laboratory-based diffractometers for research in the field of ferroelectrics. The approach is advantageous because of its high-energy, tunable microscopic beam sizes, intense photon flux, and high-resolution characteristics. For ferroelectric studies, not only powder can be probed, but also ferroelectric thin films and monolithic ceramics can be examined using a synchrotron source [82]–[86]. With the employment of a two-dimensional (2D) area detector in Debye-Scherrer geometry (transmission geometry), a synchrotron-based XRD provides the necessary capabilities to experimentally determine a pole figure representing the crystallographic direction parallel to a polarization vector. For example, 001 pole figure for tetragonal perovskites or 111 pole figure for rhombohedral perovskites [87]. This geometry enables the characterization of an entire uniaxial pole figure by evaluating the Bragg peak intensities as a function of azimuthal direction (φ), i.e. the change in intensity relative to angle to the electric field direction.

1.4. Motivation of the Research

Under the application of an external voltage, a ferroelectric ceramic is assumed and expected to experience a homogeneous electric field. This implies that a material will undergo the same field amplitude and direction between two parallel electrodes throughout a sample. Such an assumption enables the study of electric field-induced microstructural changes in monolithic ferroelectrics with respect to various angles to the macroscopic field direction with synchrotron-based XRD experiments. However, it is worth noting that an inhomogeneous electric field, i.e. different field amplitudes and directions, can develop at certain regions or throughout a ferroelectric sample with an externally applied voltage. For example, Chang *et al.* illustrates how

electric field concentrations that develop at the edges of patterned nanocomposite electrodes on PMN-PT single crystals, which is referred to as a “fringe effect”, can facilitate the nucleation of small reversible domains in local regions near the electrode edges because of the higher field magnitudes [64], [88]. Do *et al.* highlights the excessive non-180° domain switching that occurs near electrode edges of a PZT-based thin film capacitor, emphasizing the role of electric field concentration regions in ferroelectric applications [89]. Moreover, the electric field concentrations can extensively develop near the interdigitated electrode edges in multilayer ceramic actuators (MLCAs) [90]–[92]. MLCAs are ubiquitous in ferroelectric applications as they are commonly used in commercial transducers, sensors, and fuel-injectors due to their low driving voltage, high-strain generation, and quick response time. Specifically, as presented in Figure 1-5, a finite element analysis (FEA) conducted by Caleb Mooney predicts that the electric field concentration near an interdigitated electrode edge is at least 10 times higher than that between the interdigitated electrodes, and unique local electric fields are distributed in the passive zones (dead zones). Passive zones are the regions in an MLCA device that are electrically inactive and will not undergo mechanical deformation in response to an externally applied voltage. Due to the electric field gradients near the interdigitated electrode edge, non-uniform strain will develop around the electrode termination region, which results in an inhomogeneous stress distribution. Therefore, with externally applied voltage, the inhomogeneous electric field-induced microstructural changes are expected to be spatially non-uniform in distinguished regions inside of a MLCA. However, there exists a lack of understanding of the fundamental mechanisms that drive inhomogeneous electric field or field concentration-induced microstructural changes, not only in MLCAs, but also in monolithic ferroelectric ceramics.

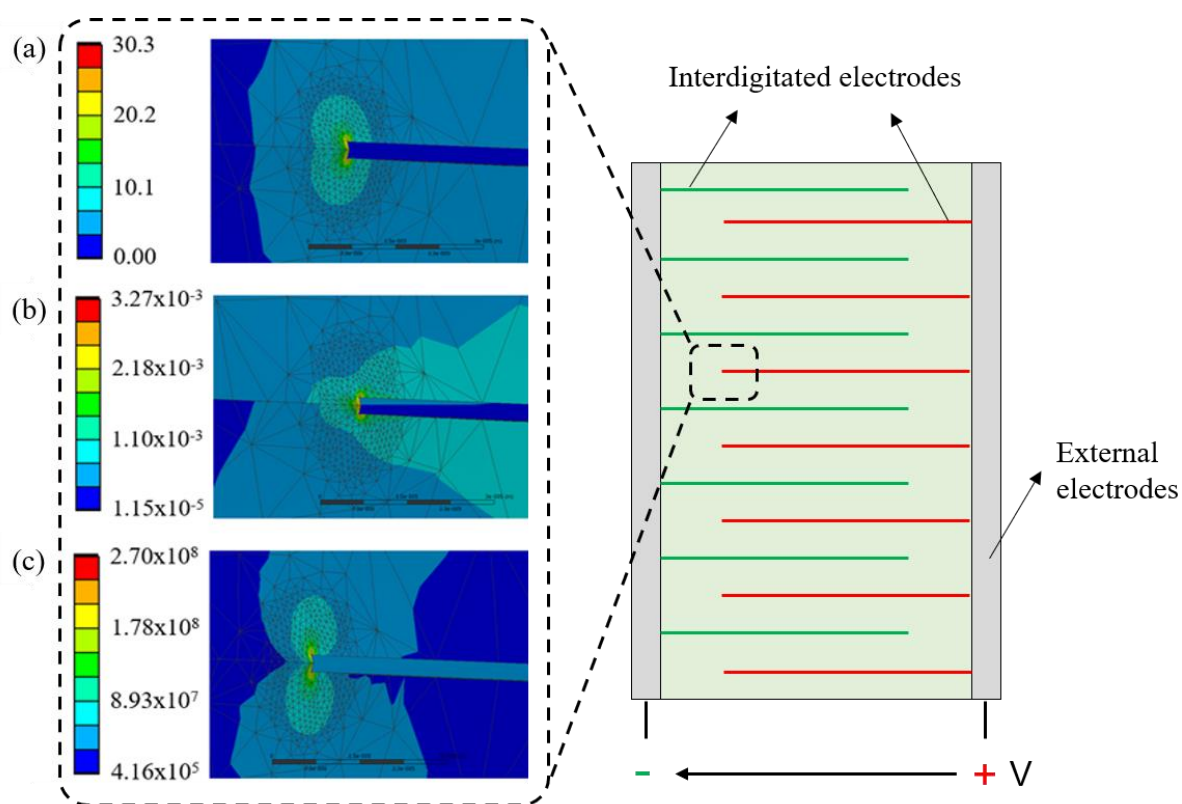


Figure 1-5 Two dimensional FEA results of inhomogeneous (a) electric field [kV/mm], (b) strain, and (c) principal stress [Pa] distributions around an interdigitated electrode edge in a KNN-based MLCA under the application of 3 kV/mm. The interdigitated electrode spacing is 53 μm . Courtesy of Caleb Mooney for the FEA work.

This research seeks to investigate the domain behaviors and phase transitions in lead-based and lead-free ferroelectric ceramics undergoing homogeneous and inhomogeneous electric field by employing synchrotron-based *in situ* high-energy XRD with tunable micron-scale beam sizes. Because of the complexity of investigating MLCAs *in situ*, this dissertation uses the monolithic polycrystalline ferroelectric samples with varied top and bottom electrode ratios to investigate the inhomogeneous electric field-induced electromechanical responses in ferroelectric materials. By employing the high-energy monochromatic x-ray beam and area detector methods, this work demonstrates the value of a synchrotron-based *in situ* XRD approach to characterize inhomogeneous domain reorientation and phase evolutions in ferroelectric materials. Specifically,

Chapter 2 introduces the synchrotron-based XRD experiment setup, materials, and sample geometries used in this research. Chapter 3 presents the results from homogeneous field-induced microstructural changes in various materials and demonstrates that the complete evaluation of all directions relative to the electric field direction is necessary to thoroughly assess field-induced material behaviors in ferroelectrics. Chapter 4 will focus on elaborating upon the inhomogeneous electric field-induced microstructural changes in the partial electrode samples, showing the calculated local electric field directions in each x-ray scanned pixel. Chapter 5 will conclude the important research findings and scientific conclusions about inhomogeneous electric field-induced domain reorientation and phase transitions in ferroelectric materials, and their impacts in future ferroelectric studies as well as applications for next generation MLCA designs.

Chapter 2: *In Situ* Experimental Setup and Data Analysis

2.1. Overview

This chapter elaborates upon the value of using the synchrotron-based high-energy XRD characterization method with applied electric fields to characterize field-induced microstructural changes in ferroelectric ceramics. With the employment of an area detector, a complete evaluation of all azimuthal orientations relative to the macroscopic direction of the applied electric field has proved essential to thoroughly assess the field-induced changes to stable phases and domain textures. A brief data analysis procedure for studying the field-induced domain texture is introduced by using a commercial PZT-EC-65 ferroelectric material with a tetragonal phase. This analysis procedure will be used for all the lead-based and lead-free ferroelectric materials in Chapters 3 and 4.

2.2. Samples

1% niobium (Nb) doped PZT (Nb-PZT) pellets of varied compositions, including Nb-PbZr_{0.50}Ti_{0.50}O₃ (Nb-PZT 50/50), Nb-PbZr_{0.53}Ti_{0.47}O₃ (Nb-PZT 53/47), and Nb-PbZr_{0.56}Ti_{0.44}O₃ (Nb-PZT 56/44) were provided by PI Ceramic (PI Ceramic GmbH, Lederhose, Thuringia, Germany). The Nb-PZT-based pellets were fabricated under the project, “Computergestuetzte Multi-skalenmodellierung zur virtuellen Entwicklung polykristalliner ferroelektrischer Materialien” (COMFEM) [93]. The Nb⁵⁺ dopants substitute the Zr⁴⁺ or Ti⁴⁺ in the perovskite B-sites, resulting in the generation of A-site vacancies to form PZT materials into soft ferroelectrics [94], [95]. Compared to a hard ferroelectric ceramic, the soft ferroelectric ceramics exhibit lower coercive field, a higher dielectric loss, and more readily permit domain wall motion under the application of electric fields [96]. In general, the crystal structures of both Nb-PZT 50/50 and Nb-PZT 53/47 are considered to be single-phase tetragonal (*P4mm*) in the

virgin state, where the latter composition is closer to the MPB [86]. In the case of Nb-PZT 56/44 composition, it has a single rhombohedral phase ($R3m$) in the virgin state.

In addition to lead-based ferroelectric materials, lead-free KNN-based materials were also investigated in the synchrotron-based experiments. Undoped $K_{0.50}Na_{0.50}NbO_3$ (undoped KNN) pellets were provided by Prof. Barbara Malič's group at the Jožef Stefan Institute, Slovenia. With its rhombohedral-orthorhombic phase transition around -123°C , and its orthorhombic-tetragonal phase transition occurring at approximately 210°C , the undoped KNN has a single orthorhombic phase in the virgin state at room temperature [56].

Another lead-free material examined in the synchrotron-based experiment was lithium (Li^+), tantalum (Ta^{5+}), and manganese (Mn^{2+}) doped $K_{0.50}Na_{0.50}NbO_3$ (doped KNN) ferroelectric ceramic, which was also provided by PI Ceramic. The addition of Li^+ and Ta^{5+} significantly lower down the orthorhombic-tetragonal phase transition below the room temperature, i.e. the doped KNN material has a single tetragonal phase ($P4mm$) at room temperature. Moreover, KNN-based ceramics often contain electron holes induced by K and Na evaporations in high-temperature sintering, which results in high current leakage under the application of external fields [97]. To decrease the leakage current, it is effective to substitute Nb^{5+} in the perovskite B-site with Mn^{2+} dopant in order to absorb the positively charged holes by increasing Mn valence ($\text{Mn}^{2+} - \text{Mn}^{4+}$) [97].

2.3. Electrode Configuration and Scan Patterns

For each composition of Nb-PZT-based and KNN-based materials, three kinds of samples and scan patterns were measured in the beamline experiments. Figure 2-1(a) shows the schematic of a sample in the full-electrode configuration, in which a $500\ \mu\text{m} \times 500\ \mu\text{m}$ X-ray beam was centered in the middle of the sample. Under the application of an external voltage, this sample is expected to have a homogeneous electric field between the top and bottom electrodes. Such a sample geometry has been commonly used to study material behavior in function of applied electric fields in multiple *in situ* high-energy XRD research [19], [86], [98]–[101]. The results from samples with the full-electrode configuration will be shown and discussed in Chapter 3.

Figure 2-1(b) illustrates a partial-electrode sample geometry. Under the stimulus of an external voltage, the sample is expected to experience inhomogeneous electric fields near the electrode termination region, which is the central section of the sample near where the top electrode ends, and in the dead zone, which is the portion shown on the left where there is no top electrode. The experiment described as “whole bar scan” used an approximately $500\ \mu\text{m} \times 500\ \mu\text{m}$ X-ray beam to study the spatially dependent behavior in different partial-electrode samples. It is worth noting that $500\ \mu\text{m} \times 500\ \mu\text{m}$ and $500\ \mu\text{m} \times 450\ \mu\text{m}$ beam sizes (horizontal \times vertical, H \times V) were chosen for the experiments based on the thicknesses of the samples used, i.e. depending on whether the samples were slightly greater or less than 1 mm in height. By doing so, the X-ray scattering from electrodes and the sample stage could be mitigated. No significant differences in results were observed between the two beam sizes for the purpose of this experiment.

The schematic presented in Figure 2-1(c) illustrates what is referred to as an “electrode edge scan” experiment in a higher spatial resolution. A much smaller X-ray beam size, $200\ \mu\text{m} \times 200\ \mu\text{m}$, was adopted to scan the electrode termination region to investigate the material behavior

with respect to field concentration. The results from partial-electrode samples in either “whole bar scan” or “electrode edge scan” experiments will be shown and discussed in Chapter 4.

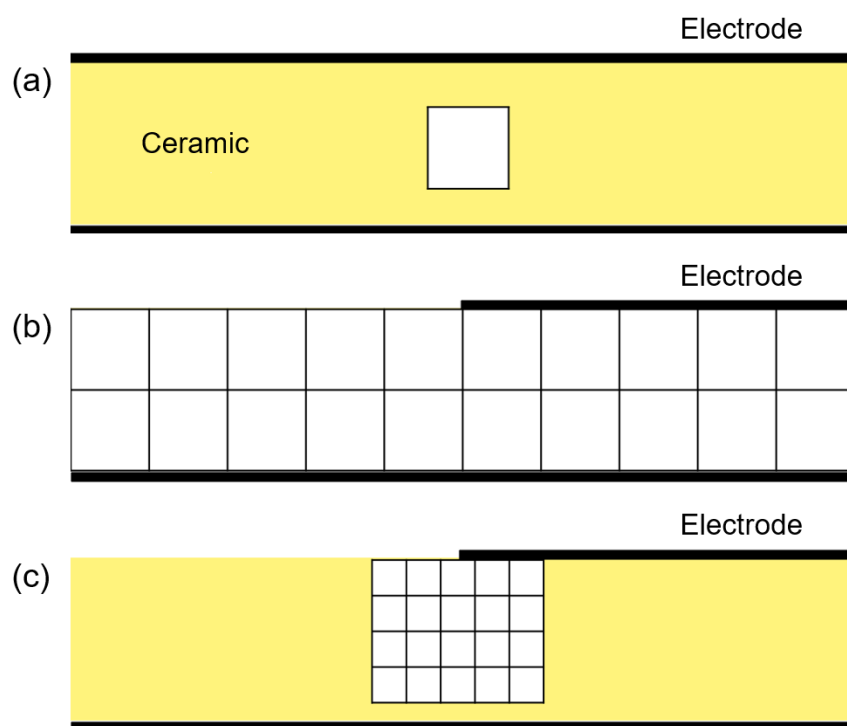


Figure 2-1 X-ray scan patterns for the synchrotron-based experiments in beamline 11-ID-C, showing the full-electrode sample with (a) center scan, and the partially electroded sample with (b) whole bar scan, and (c) electrode edge scan.

2.4. Experiment Description

The synchrotron-based *in situ* high-energy XRD with applied electric fields was carried out in the beamline 11-ID-C at the advanced photon source (APS). Figure 2-2 shows a schematic of the experimental setup for the *in situ* high-energy XRD, which illustrates the electrode configurations for both (a) full-electrode samples and (b) partial-electrode samples. The X-ray beam had an energy of 105.7 keV, equivalent to a wavelength of 0.1173 Å, which penetrated ceramic bars of listed sample dimensions, easily through the Debye-Scherrer geometry, i.e., transmission geometry. Some key beamline parameters are summarized in Table 1 [102].

Table 1 Specifications of beamline 11-ID-C.

Source (upstream)	3.3 Undulator (Undulator A)
Source (downstream)	2.3 Undulator
Monochromator Type	Laue Si (311) 1.8-degree fixed
Energy Range	105.7 keV
Resolution ($\Delta E/E$)	5×10^{-3}
Flux (Photons/second)	1×10^{11} @ 105.7 keV
Beam size, horizontal x vertical (H x V)	
Unfocused	0.2 mm x 0.2 mm

Rectangular bars of dimensions approximately 5 mm x 1 mm x 1 mm were cut from monolithic Nb-PZT-based and KNN-based ceramic pellets and painted with silver paste on two opposite parallel 5 mm x 1 mm surfaces to form electrodes. The bar was placed on a custom sample stage for the application of electric fields via a high-voltage amplifier (AMS-10B2, Matsusada Precision, Shiga-ken, Japan) that was driven simultaneously by a wavefunction generator (Agilent 33220A, Keysight Technologies, Santa Rosa, CA). For most of the samples, unipolar electric fields

were applied to the specimens using steps of 1 kV/mm up to a 3 kV/mm maximum, which is considered a poling process. For a few specific samples, such as Nb-PZT 53/47, whose composition is close to the MPB, a maximum electric field of 7 kV/mm was applied to the sample, with the same 1 kV/mm step size. The longitudinal piezoelectric coefficient was measured for each sample after the experiment via a wide-range d_{33} Tester (YE2730A d_{33} METER, APC International, Mackeyville, PA) to ensure the samples were polarized during the measurements. 2D Debye-Scherrer ring diffraction patterns were collected on an area detector (XRD1621 amorphous silicon detector, PerkinElmer, Fremont, CA) in transmission geometry.

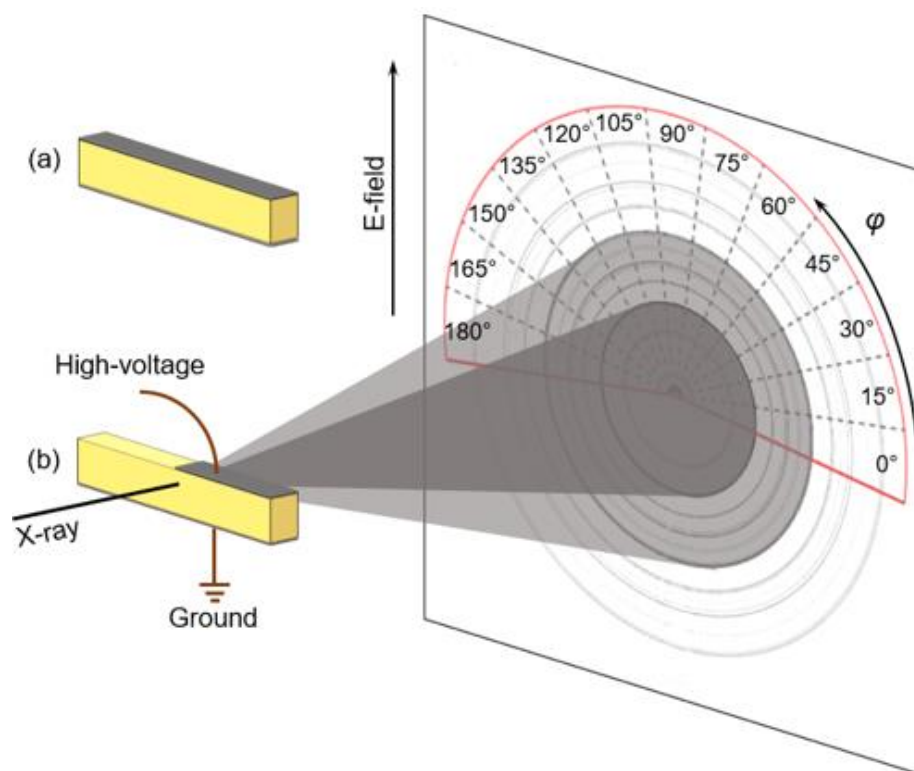


Figure 2-2 Schematics of the synchrotron-based experimental setup in beamline 11-ID-C, APS, using the piezoelectric (a) full-electrode sample, and (b) partial-electrode sample.

Figure 2-3 shows the experimental setup in the beamline hutch at beamline 11-ID-C, APS. The custom sample stage was mounted on a 6-axis Hexapod (H-850, PI motion | positioning,

Auburn, MA) which allowed the stage to move in multiple directions (six degrees of freedom, x , y , z , θ_x , θ_y , θ_z) in microscale incremental steps [103]. The PerkinElmer 2D area detector was placed approximately 1500 mm away from the customized sample stage. It is worth noting that the real sample-to-detector distance needs to be carefully calibrated in data analysis. The high-energy X-ray beam with tunable micro-scale beam sizes entered from the left side, penetrated the sample, and generated Debye-Scherrer cones, which ultimately interacted with the detector to form 2D Debye-Scherrer rings. The custom sample stage was built by the Jones research group for investigating simultaneous microstructural changes of monolithic piezoceramics under the application of electric fields. As shown in Figure 2-4, the sample was placed in a Kapton holder that was filled with Fluorinert (3M™ FC-40), which is an electrically insulating liquid to prevent dielectric arcing during the experiments. High voltage was applied to the sample through the top pin electrode.

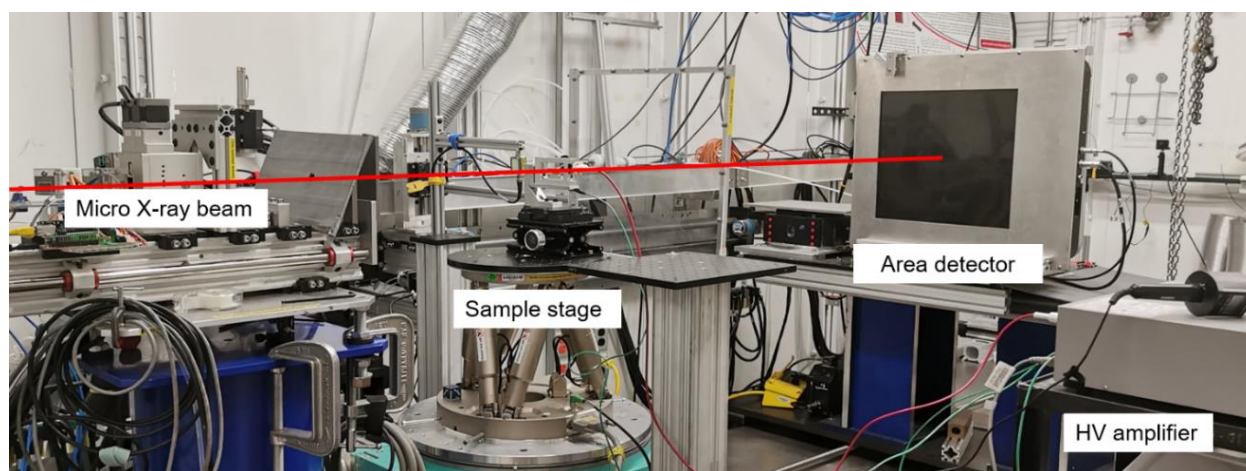


Figure 2-3 Layout for the custom sample stage and the 2D area detector in beamline 11-ID-C, APS.

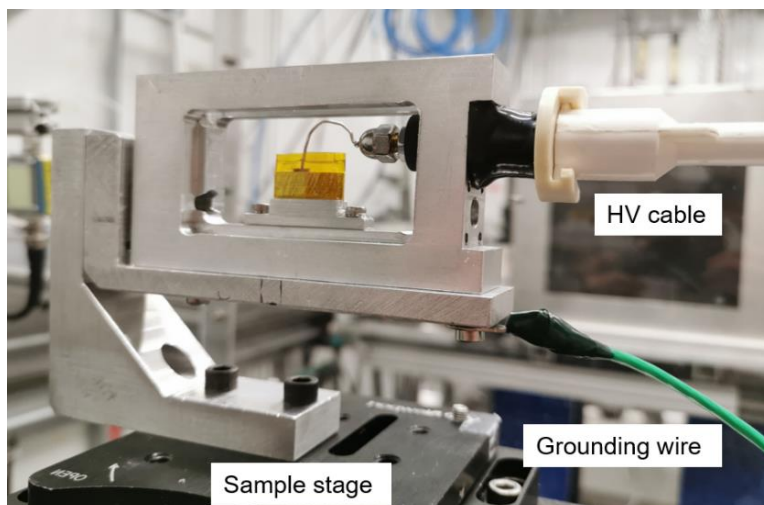


Figure 2-4 The custom sample stage with connections to a HV cable and a grounding wire. The piezoceramic sample is placed in the Kapton tube.

2.5. Data Reduction

For the collected Debye-Scherrer rings, also referred to as 2D XRD patterns, the radial direction represents the 2θ angle, and the azimuthal angle (φ) represents the angle relative to the macroscopic electric field, as shown in Figure 2-2. The diffraction rings are the reflections from different crystallographic planes, and their radii relate to the 2θ angles through Bragg's Law. The electric field-induced microstructural changes are recorded on the 2D XRD pattern, and it is influenced by the local electric field direction. For example, for a pattern collected in an experiment using the full-electrode sample (Figure 2-1(a)), the electric field is considered to be homogeneous and normal to the electrodes. Hence the field-induced microstructural changes would reflect on the Debye-Scherrer rings symmetrically along the vertical and horizontal axes. However, if the local electric field direction in a scanned pixel is not parallel to the macroscopic electric field direction (normal to the top and bottom electrodes), the field-induced structural changes should be asymmetrical along the vertical and horizontal axes, i.e. it is influenced by the

local electric field direction in the pixels undergoing an inhomogeneous field. Such pixels can be found in the dead zone in a partial-electrode sample.

Regardless of whether the local electric field direction of the scanned pixel is parallel to the macroscopic field direction or not, it is reasonable to study only either the top half or the bottom half of a 2D XRD pattern since they both contain the full orientation-dependent information of microstructural changes within a 180° azimuthal range. In this dissertation, the top half of the obtained 2D XRD patterns is used in the data reduction and analysis. As seen in Figure 2-5(a), the top half of the obtained 2D XRD pattern is divided into 13 sectors along the azimuthal direction, where each sector has an integration width of 15° . The 90° sector is parallel to the electric field direction and contains scattering information from scattering vectors oriented approximately parallel to the electric field. The 0° and 180° sectors are horizontal and contain scattering information from scattering vectors perpendicular to the electric field direction. Data from all 13 sectors is used in this work. Data reduction can be conducted by using several software packages, such as Fit2D [104], General Structure Analysis System (GSAS, GSAS-II) [105], [106], Material Analysis Using Diffraction (MAUD) [107], Total Pattern Analysis Solution (TOPAS) [108], and FullProf Suite [109]. Fit2D is used in data reduction for this dissertation and Appendix A explains the process using commercial PZT-EC-65 ferroelectric material as an example.

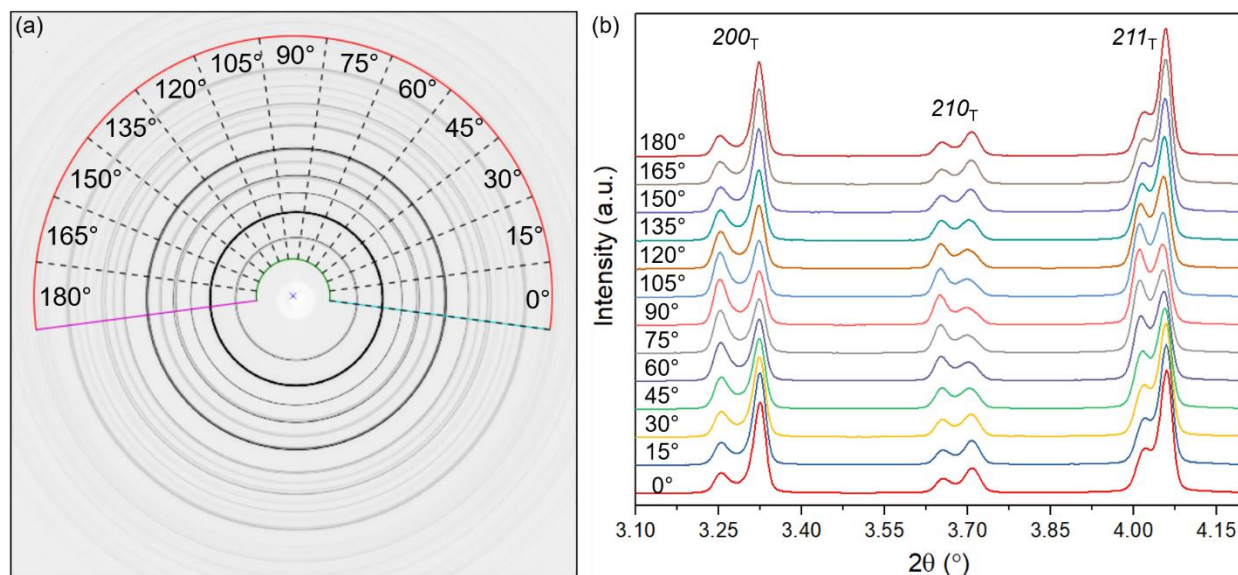


Figure 2-5 (a) The divided sectors in a 2D XRD pattern, and (b) integrated 1D plots from different azimuthal sectors for the tetragonal phase commercial PZT-EC-65 ferroelectric sample with the full-electrode configuration at 3 kV/mm.

Two complementary methods are commonly applied to represent and analyze the reduced 1D data. The first is to analyze data in a given azimuthal sector as a function of the electric field magnitude. Figure 2-6 shows representative contour plots analyzed in this way for a tetragonal phase commercial PZT-EC-65 ferroelectric material. By representing the data in this way, variations in peak intensity can be observed, such as the relative intensity changes of the 002_T and 200_T reflections. Under the application of 3kV/mm, the 002_T reflection becomes more intense than the virgin state, which is because $[001]$ is the polarization direction in the tetragonal phase. The other way to represent and analyze the data is to consider the orientation-dependent material behavior at a given electric field amplitude. For example, as shown in Figure 2-7(b) at 3 kV/mm the 002_T reflection is most intense in the 90° azimuthal sector, which represents the direction parallel to the electric field direction. In contrast, the intensity of the 200_T reflection is weakest at 90° and strongest at 0° and 180° .

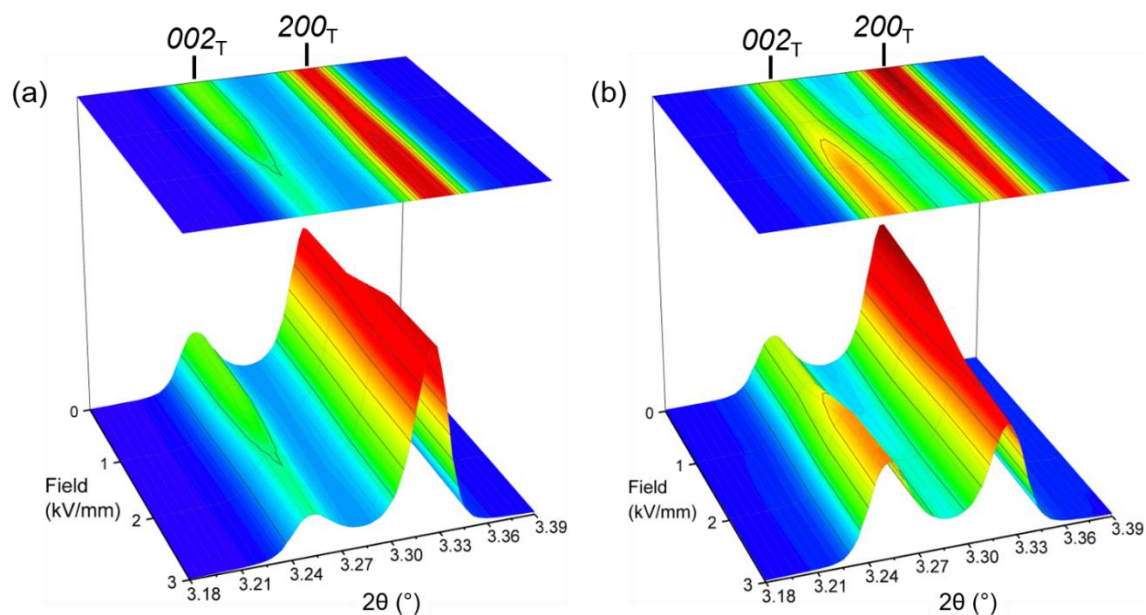


Figure 2-6 Peak intensities as a function of electric field amplitude for the tetragonal phase commercial PZT-EC-65 sample with the full-electrode configuration at (a) 0° , and (b) 90° azimuthal angles.

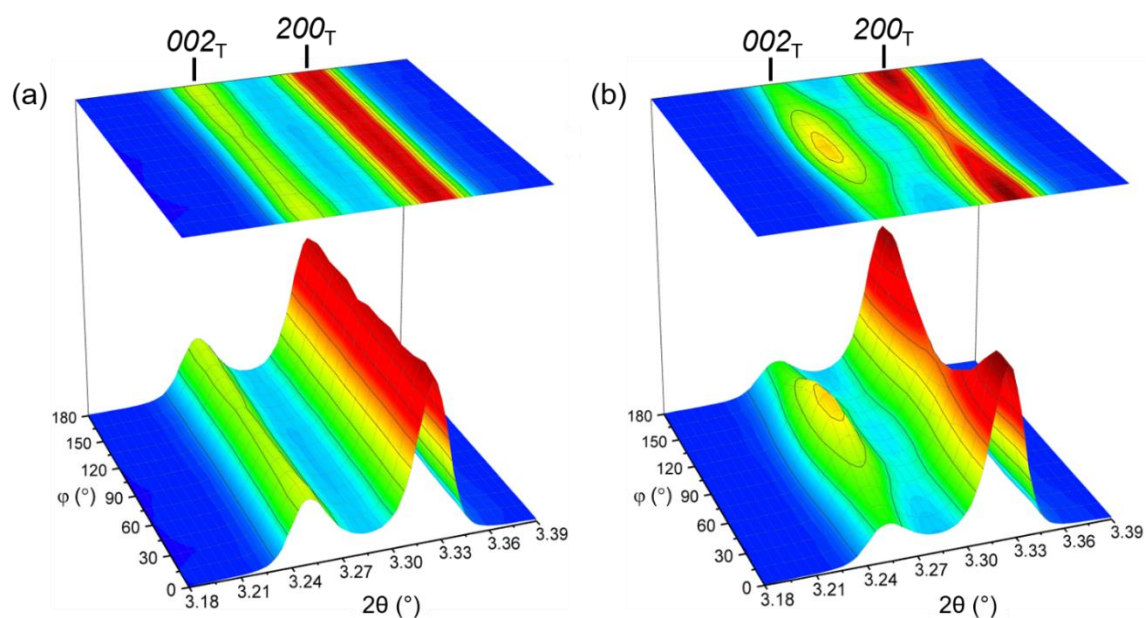


Figure 2-7 Peak intensities as a function of azimuthal angle ϕ for the tetragonal phase commercial PZT-EC-65 sample with the full-electrode configuration in (a) the virgin state, and (b) 3 kV/mm.

2.6. Peak Fitting Analysis

Performing peak fitting analysis on a series of 1D XRD plots from ferroelectric ceramics provides insight into the material's structure-property relationships in response to the external stimuli, such as temperature, stress, electric field, frequency, etc. For example, domain reorientation in ferroelectrics, which is observed from the interchanging intensities in the degenerate peaks, can be analyzed from the fitted intensities. Line Profile Analysis Software (LIPRAS) is a package developed by the Jones Research Group that is capable of fitting multiple XRD plots simultaneously and robustly at all azimuthal angles and electric fields [110]. The software utilizes a least squares regression algorithm to minimize the difference between a modeled plot and the experimental plot. Coupled with a user friendly graphic interface, LIPRAS allows for custom peak fitting options, including combining different types of profile functions and constraining parameters such as full width half maximum (FWHM), 2θ , and intensity [111]. Appendix B discusses the various profile functions for describing reflection shapes in different phases. The detailed analyzing procedures for peak fitting is demonstrated in the software manual in Ref. [110]. The peak fitting analysis conducted in LIPRAS extracts microstructural information from degenerate peaks to calculate ferroelectric/ferroelastic domain texture strength under the application of electric fields, which is a critical parameter for discussing the synchrotron-based experimental results in Chapter 3 and 4.

Chapter 3: Homogeneous Electric Field-Induced Material Behaviors

3.1. Overview

This chapter demonstrates results from samples with full-electrode configuration, as illustrated in Figure 2-1(a), that were examined in synchrotron-based experiments at beamline 11-ID-C, APS. Under the application of high voltage, these samples were expected to have homogeneous electric field between the top and bottom electrodes. A 500 μm x 500 μm monochromatic high-energy X-ray beam was used to scatter the center of each ferroelectric sample. The degree of domain alignment is calculated for the tetragonal and rhombohedral samples. In parallel, the fraction of domain interchange is quantified for the orthorhombic samples. These results from full-electrode samples will be used for comparisons and discussions with those from partial-electrode samples in Chapter 4.

3.2. Nb-PZT-based Materials

3.2.1. Nb-PZT 50/50

Figure 3-1 shows the tetragonal phase 002 and 200 reflections, herein referred to as 002_{T} and 200_{T} , as a function of azimuthal angle φ for the tetragonal phase Nb-PZT 50/50, which is the composition furthest from the MPB. In the virgin state, as shown in Figure 3-1(a), the 002_{T} and 200_{T} peak intensities are nearly constant with respect to the azimuthal angle. However, at the maximum electric field amplitude of 3 kV/mm, as shown in Figure 3-1(b), the 002_{T} and 200_{T} reflections change intensity as a function of azimuthal angle. More specifically, the intensities are shown to interchange, which means that intensity from 002_{T} moves to 200_{T} or vice versa, which is a signature of ferroelectric/ferroelastic domain wall motion at the maximum electric field [76].

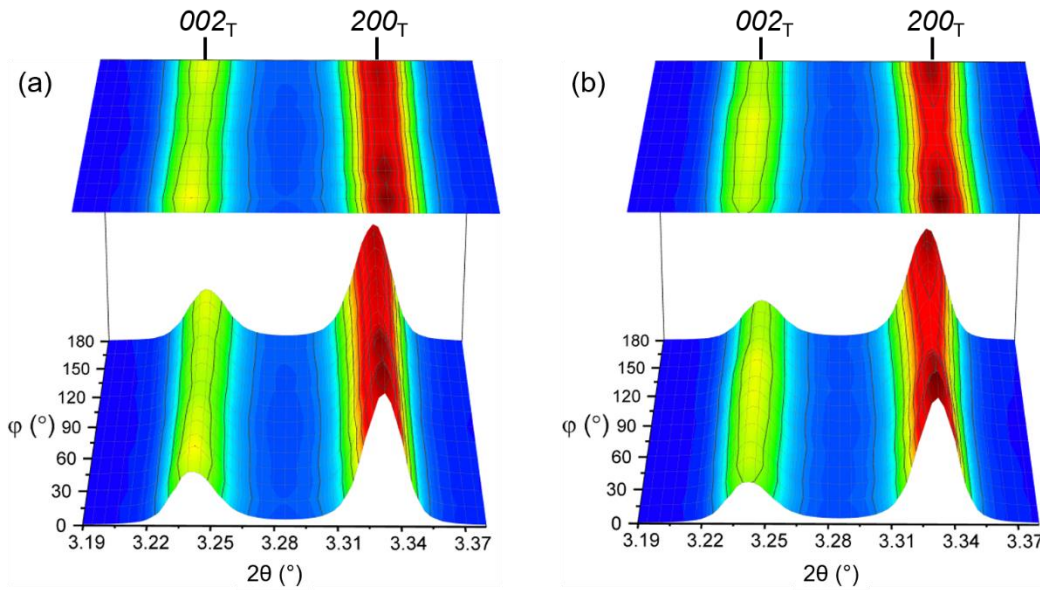


Figure 3-1 Peak intensities as a function of azimuthal angle (φ) for the tetragonal phase Nb-PZT 50/50 sample with the full-electrode configuration in (a) the virgin state and (b) 3 kV/mm.

At a given electric field, the field-induced domain texture can be quantitatively studied by using established equations [17]. Equation (5) calculates the degree of domain alignment, or degree of preferred orientation, in tetragonal ferroelectric material using the degenerate peak intensities,

$$f_{002(MRD)} = 3 \frac{\frac{I_{002}}{I'_{002}}}{\frac{I_{002}}{I'_{002}} + 2 \frac{I_{200}}{I'_{200}}} \quad \text{Equation (5)}$$

where, I_{002} and I_{200} are the integrated peak intensities at a given electric field; I'_{002} and I'_{200} are the integrated peak intensities in the virgin state of a random-oriented tetragonal ferroelectric sample. Multiple of random distribution (MRD) is the unit to describe domain textures. $f_{002} = 1.0$ MRD indicates that the sample is in the virgin state or there is no domain reorientation at a given electric field; $f_{002} = 3.0$ MRD is the maximum theoretical value that indicates the domain reorientation is saturated.

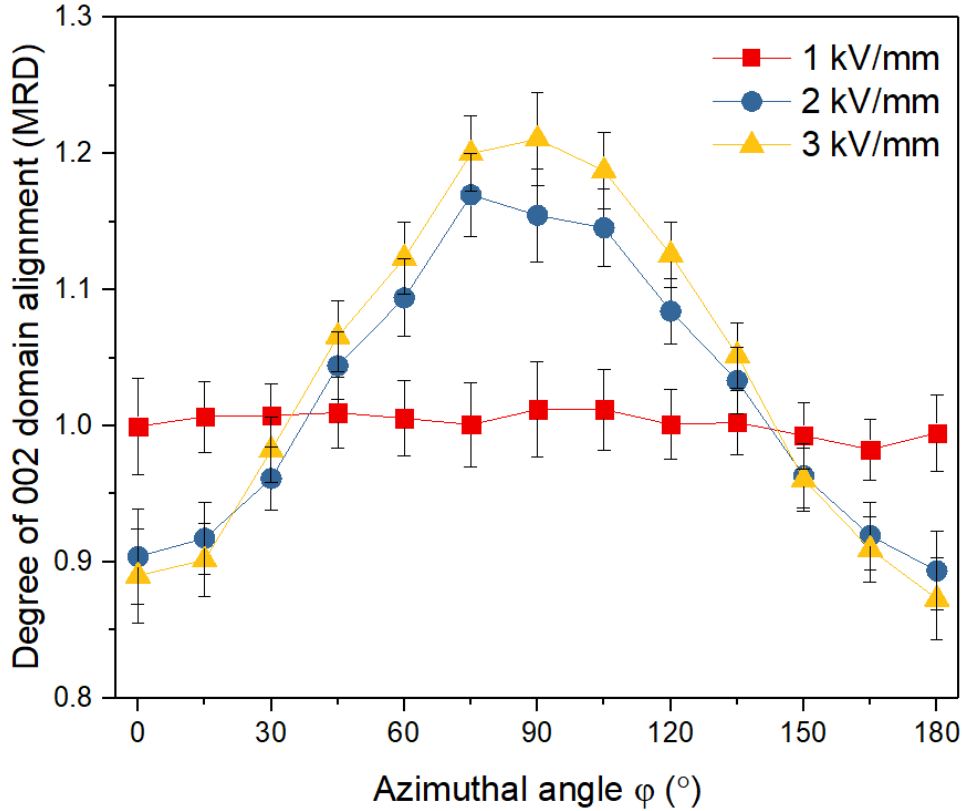


Figure 3-2 The degree of 002 domain alignment of the tetragonal Nb-PZT 50/50 sample with the full-electrode configuration at multiple electric field amplitudes along all azimuthal angles.

By performing the peak fitting analysis in LIPRAS, the intensity of each reflection can be integrated from the 1D XRD plots at all azimuthal angles and all electric fields. Under these circumstances, the domain texture preference corresponding to the $(002)_T$ planes, or the 002 domain texture strength, in the tetragonal phase Nb-PZT 50/50 can be quantified using Equation (5). Figure 3-2 shows the calculated 002 domain texture strength at different electric fields for the Nb-PZT 50/50 sample with the full-electrode configuration. As seen from the plot, the electric field-induced domain texture is not significant at 1 kV/mm since the calculated 002 domain texture strength fluctuates in a very small range around 1.0 MRD at all azimuthal angles, which is reasonable because the coercive field of the Nb-PZT 50/50 composition is approximately 1 kV/mm. However, the 002 domain texture strength become stronger at 2 kV/mm and 3 kV/mm

that both show the strongest domain preference approximately parallel along the direction of macroscopic electric field. More specifically, at the highest electric field of 3 kV/mm, it reaches the maximum degree of 002 domain alignment, 1.21 MRD. An alternative way to think about Figure 3-2 is that it is a 1D slice through a 002 pole figure.

3.2.2. Nb-PZT 53/47

Figure 3-3 presents peak intensities as a function of azimuthal angle for Nb-PZT 53/47, the composition closest to the MPB, in the virgin state and elevated electric fields of 3 kV/mm and 7 kV/mm. The figure shows that, in the virgin state, Nb-PZT 53/47 sample has well-separated 002_T and 200_T reflections in all azimuthal angles. However, by the application of electric field at 3 kV/mm, an additional peak appears between the 002_T and 200_T reflections at approximately the 45° and 135° azimuthal angles, which means a new phase emerges under the field application. Due to the Nb-PZT 53/47 sample having a composition close to the MPB, compositions for which tetragonal and rhombohedral phases coexist, the emerged peak is evidenced to be the 200 reflection in the rhombohedral phase, i.e., 200_R .

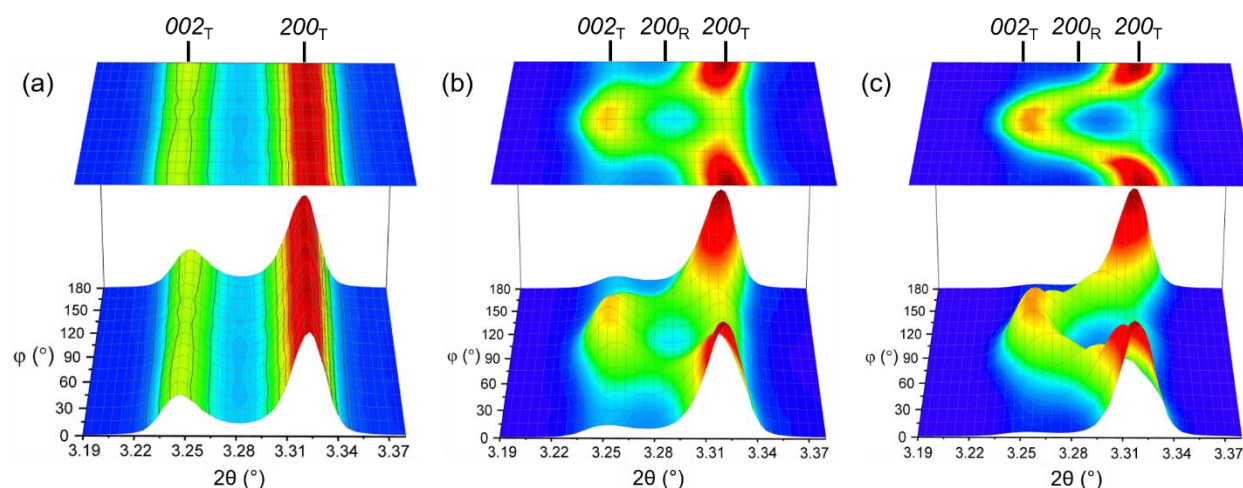


Figure 3-3 Peak intensities as a function of azimuthal angle (φ) for the Nb-PZT 53/47 sample with the full-electrode configuration in (a) the virgin state, (b) 3 kV/mm, and (c) 7 kV/mm.

Although the Nb-PZT 53/47 full-electrode sample presents the emergence of a rhombohedral phase under application of electric fields at approximately the 45° and 135° azimuthal angles, the other azimuthal angles evidence a stable tetragonal phase with domain wall motions apparent from 002_T and 200_T peak intensity interchanges. As the applied electric field reaches to 7 kV/mm, as seen in Figure 3-3(c), the electric field-induced phase transitions at approximately 45° and 135° are amplified since the emerged 200_R reflection becomes more intense.

Not only the phase transitions are amplified around the 45° and 135° orientations, but the domain reorientation is also enhanced at the other azimuthal angles, i.e., field amplitude-dependent material behaviors occur in the Nb-PZT 53/47 composition. Figure 3-4(a) and (c) namely illustrates the domain reorientation in the 0° and 90° azimuthal angles. As shown in Figure 3-4(a), the intensity of 002_T reflection is gradually weakened with increasing the electric field from 0 to 7 kV/mm, which evidences that the 002 domain texture strength is decreased in the 0° azimuthal angle, or the direction perpendicular to the macroscopic electric field; whereas the 002 domain texture strength enhances with increasing the field amplitude in the 90° azimuthal angle, or the direction parallel to the macroscopic electric field. Figure 3-4(b) provides the evolution of 200_R reflection as a function of electric field amplitude along the 45° azimuthal angle, revealing that the induced phase transition from tetragonal to rhombohedral is a field amplitude-dependent response.

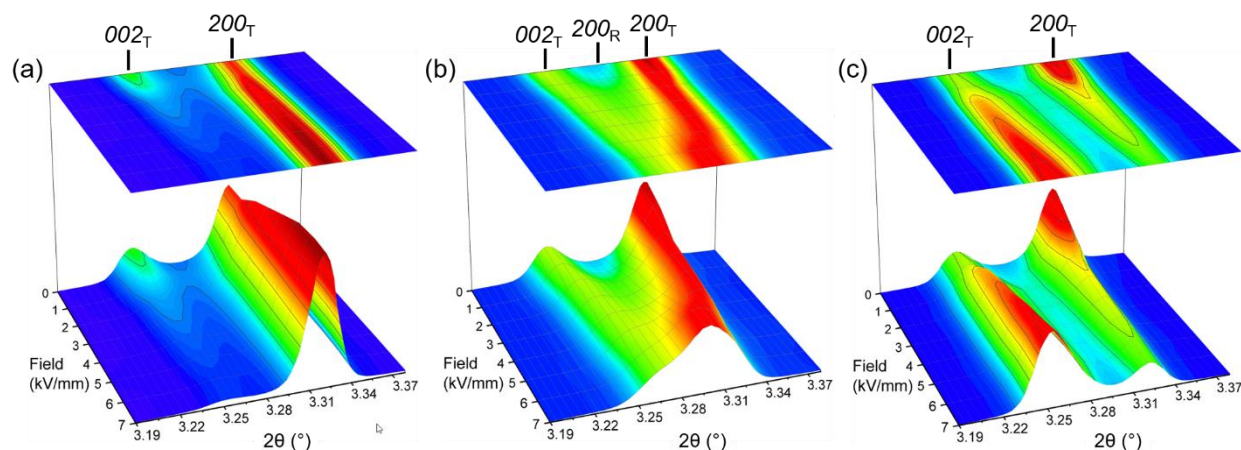


Figure 3-4 Peak intensities as a function of electric field amplitude for the Nb-PZT 53/47 sample with the full-electrode configuration at the (a) 0° , (b) 45° , and (c) 90° azimuthal angles.

To quantitatively probe the domain reorientation behaviors in Nb-PZT 53/47, the degree of 002 domain texture strength along the 0° and 90° azimuthal angles are computed, as plotted in Figure 3-5. The 002 domain texture strength was not calculated in the 45° and 135° azimuthal angles since there are field-induced phase transitions. As shown in Figure 3-5, in the 90° azimuthal angle, the 002 domain texture strength increases from 1.00 MRD in the virgin state to 2.38 MRD in the 7 kV/mm, i.e. a field-induced 002 domain texture strength at the maximum electric field is 2.38 times higher than the virgin state. However, in the 0° azimuthal angle, or in the direction perpendicular to the macroscopic electric field direction, the field-induced 002 domain texture is weakened to 0.14 MRD at 7 kV/mm.

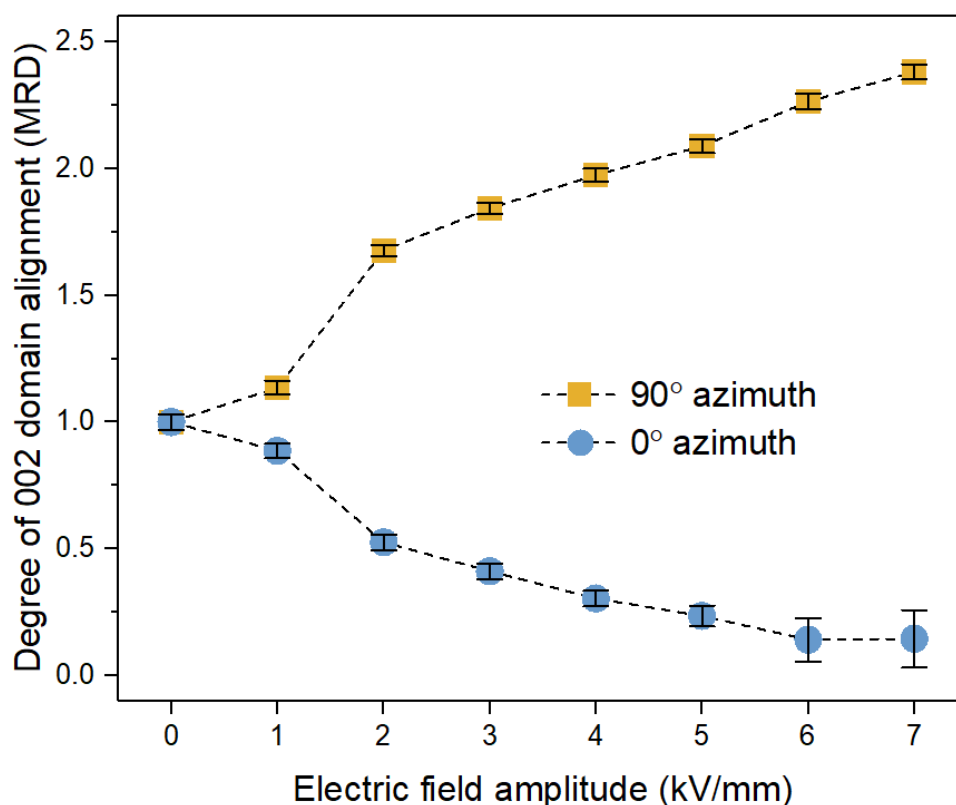


Figure 3-5 The degree of 002 domain alignment of the tetragonal phase Nb-PZT 53/47 sample with the full-electrode configuration as a function of electric field amplitude in the 0° and 90° azimuthal angles.

Figure 3-6 illustrates an important aspect of the orientation-dependent phase selection mechanism in tetragonal Nb-PZT 53/47, by using four simple schematics of unit cells numbered in (a)-(d). As a polycrystalline piezoceramic, the grains and ferroelectric domains are initially oriented in all possible crystallographic orientations equally, i.e. random orientation. The hexagons represent grains in the sample with non-180° domain walls (dash lines) separating the adjacent ferroelectric/ferroelastic striped domains. Two of these orientations are shown in Figure 3-6, one that represents a crystallographic orientation with a [001] oriented vertically (Figure 3-6(a)), and the other orientation with the [001] oriented at approximately 45° to the vertical direction (Figure 3-6(b)). In the virgin state of these orientations illustrated in Figure 3-6(a-b), the

phase is tetragonal, as evidenced by unique tetragonality (c/a), or ferroelastic strain. With a strong electric field applied, unit cells in these two orientations are driven to elongate parallel to the macroscopic field direction due to the overall longitudinal piezoelectric distortion of the sample. As illustrated in Figure 3-6(c), the tetragonal orientation shown in blue can elongate parallel to the field direction through the process of domain wall motions; however, the green grain orientation, as shown in Figure 3-6(d), which is initially in the tetragonal phase, changes phase to rhombohedral phase in order to follow the deformation of the sample. The illustration in Figure 3-6 is a simplified 2-dimensional example of a more complex 3-dimensional material response but illustrates why the phase transitions may occur selectively in some crystal orientations but not throughout all orientations in the polycrystalline aggregate.

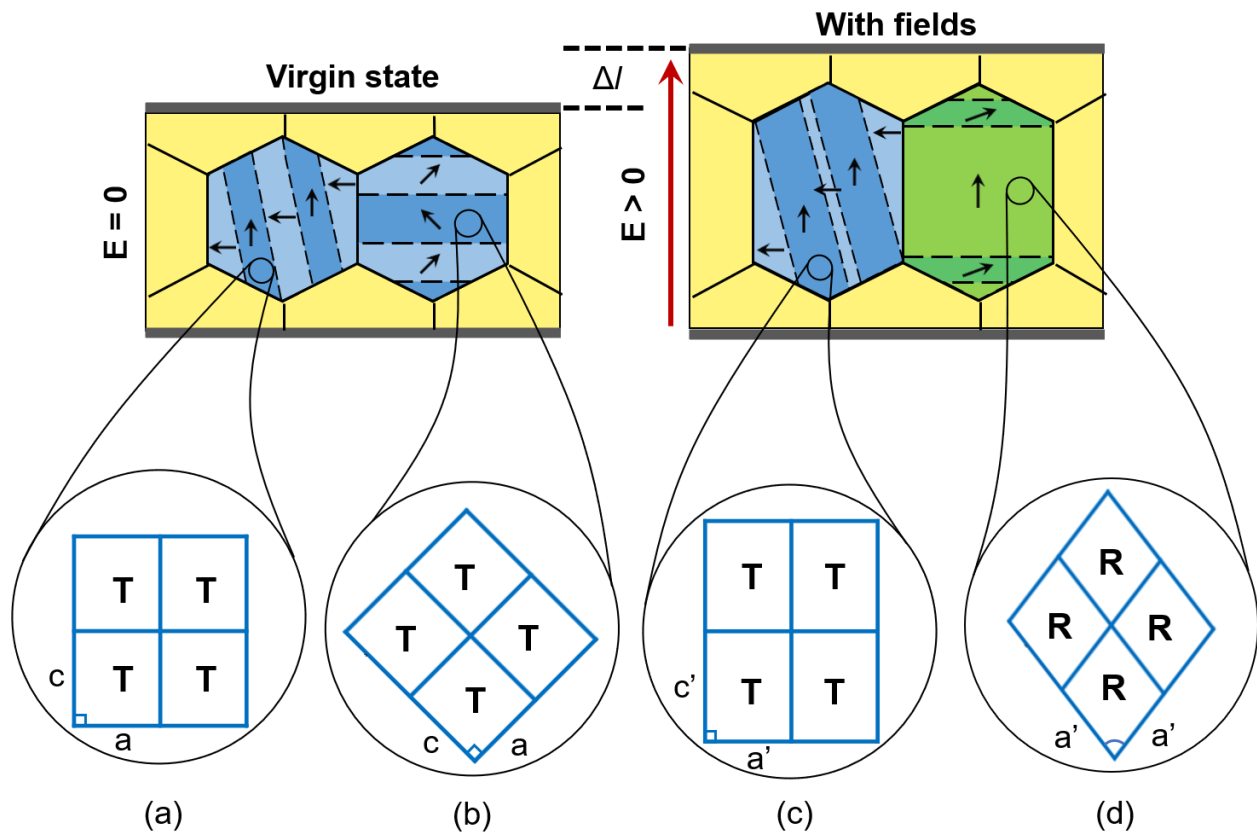


Figure 3-6 In the virgin state, the possible representative tetragonal unit cell orientations in Nb-PZT 53/47 in (a) and (b); under the application of an electric field, the elongated tetragonal unit cells in (c), and the distorted rhombohedral-like unit cells in (d).

To further understand how the orientation-dependent strains relate to the anisotropic phase transition, Figure 3-7 shows the orientation-dependent electric field-induced lattice strains that are parallel to the field direction in both tetragonal phase compositions (Nb-PZT 50/50 and Nb-PZT 53/47) during an applied electric field of 3 kV/mm. Only the 90° azimuthal sector, which is parallel to the field direction, is used in this polar strain analysis which is adopted from prior reports [17], [112]. The radial direction in the polar plot represents the amplitude of field-induced strain. [001] is the crystallographic direction parallel to the field direction, whereas $[hk0]$ represents the crystallographic direction perpendicular to the field direction. The tetragonal unit cell models represent the crystallographic orientations in real space, with the (hkl) plane perpendicular to the

electric field direction. The figure illustrates that both compositions exhibit the highest field-induced lattice strain in orientations in which the [111] directions are parallel to the electric field direction, and the lowest strain in orientations in which the [002] directions are parallel to the electric field direction. However, while orientations in which the [002] directions are parallel to the electric field direction exhibit relatively small strains, these orientations are aligned such that they are favorable for domain wall motion rather than lattice distortion. The orientations with [111] directions closely aligned to the electric field direction are more favorably oriented for lattice strain rather than domain wall motion. However, to accommodate a large deformation strain overall in the sample, the [111]-oriented crystals are also shown to exhibit transitions from the tetragonal to rhombohedral phases.

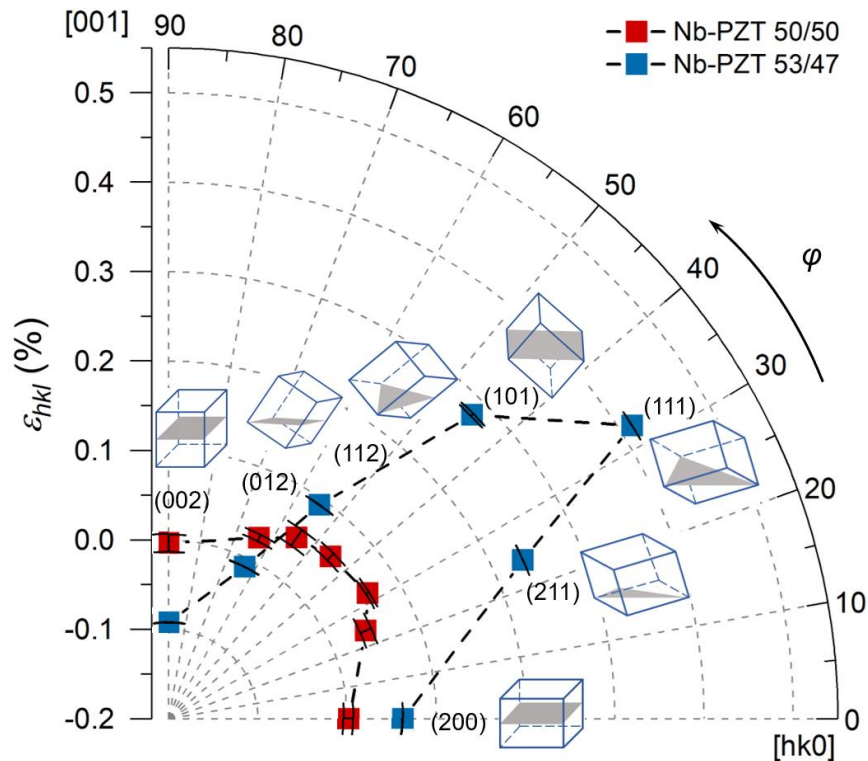


Figure 3-7 Orientation-dependent field-induced lattice strain in Nb-PZT 50/50 and Nb-PZT 53/47 at macroscopic electric field of 3 kV/mm.

Esteves *et al.* demonstrated a variant-selection mechanism that describes how polarization direction impacted the phase composition for an initially randomly-oriented ferroelectric polycrystalline material in a saturated electric field [74]. The simulated result based on 20,000 random orientations is illustrated in an inverse pole figure shown in Figure 3-8. With a saturated electric field applied along the [001] direction, the rhombohedral phase is preferred in the system when the field direction is close to the polarization directions in $\langle 110 \rangle$ and $\langle 111 \rangle$ oriented crystals. That is to suggest, for tetragonal unit cells having $\langle 110 \rangle$ and $\langle 111 \rangle$ plane normal that are more aligned with the [001] normal direction, a rhombohedral phase could be formed at an elevated electric field. Therefore, the orientation-dependent phase transition phenomena can be well explained in the Nb-PZT 53/47 ferroelectric material.

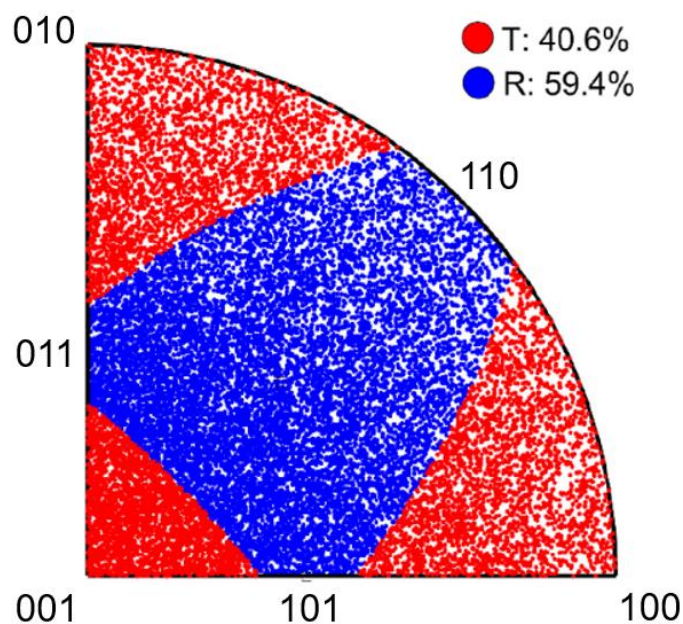


Figure 3-8 Inverse pole figure of a multi-phase simulation of tetragonal and rhombohedral grains, and their resulting phase selection based on variant selection when an electric field is applied along the [001]. Reproduced from Esteves *et al. Acta Mater.*, vol. 132, pp. 96–105, 2017.

In earlier research work, an assumption has sometimes been made that the sectors representing “45 degrees away from the field direction” (e.g., azimuthal angles of 45° and 135° in

Figure 3-5) contain texture-free information that can be utilized for phase fraction calculations and crystal structure refinement, e.g., through the Rietveld method, which facilitated lots of research work using *in situ* laboratory-based XRD with line detectors [22], [113], [114]. For instance, Hinterstein *et al.* and Fan *et al.* both used the 45° orientation to probe the tetragonal-monoclinic phase transition with raised electric fields, assuming it was texture-free and it represented the powder average of the ferroelectric sample [22], [113]. Liu *et al.* selectively analyzed the 0° and 45° orientations to describe the tetragonal-rhombohedral phase transition as activation of the inactive domains at the virgin state in the PZT-based materials [114]. However, in the present work, the results from Nb-PZT 53/47 ferroelectric sample demonstrate that the rhombohedral phase reflections observed in the sectors that are 45° from the electric field direction do not appear in other azimuthal sectors, suggesting strongly the necessity of utilizing an area detector to fully probe orientation-dependent phase transitions and domain reorientation in ferroelectric materials under the application of electric fields.

3.2.3. Nb-PZT 56/44

The polarization direction is parallel to the $\langle 111 \rangle$ directions in a rhombohedral phase ferroelectric material. By the application of electric fields, peak intensity interchange between the 111_R and $11\bar{1}_R$ reflections are observed, as shown in Figure 3-9. At the maximum electric field magnitude of 3 kV/mm, Nb-PZT 56/44 sample has the most intense 111_R reflection along the 90° azimuthal angle; in contrast, it shows the highest intensity of $11\bar{1}_R$ reflection at the 0° and 180° azimuthal angles, which are the directions perpendicular to the macroscopic electric field.

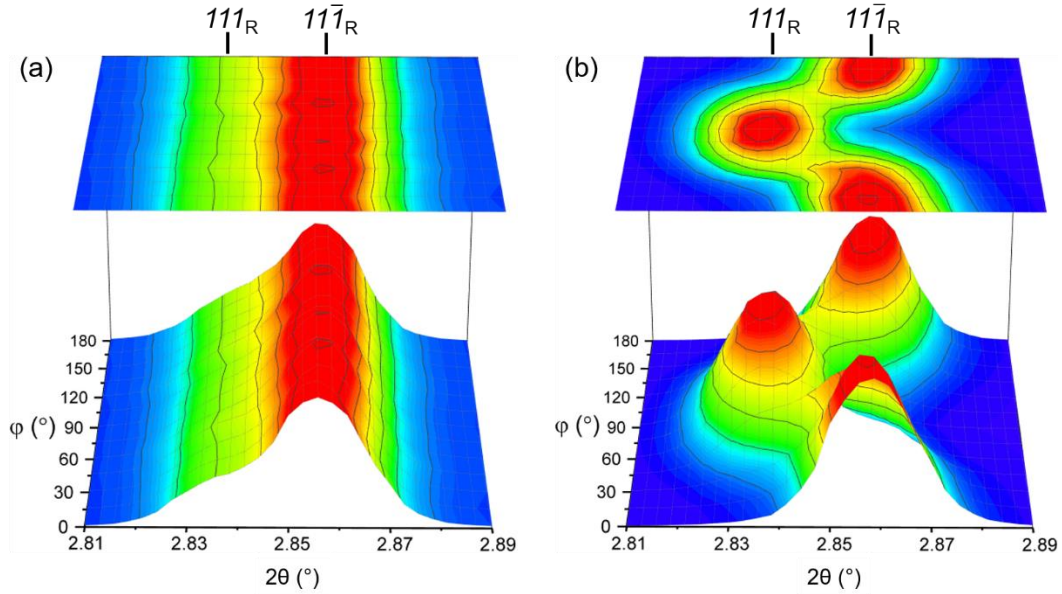


Figure 3-9 Peak intensities as a function of azimuthal angle (φ) for the rhombohedral phase Nb-PZT 56/44 sample with the full-electrode configuration in (a) the virgin state and (b) 3 kV/mm.

Equation (6) is used to calculate the degree of preferred domain orientation corresponding to the $(111)_R$ planes, or the 111 domain texture strength in a rhombohedral phase ferroelectric:

$$f_{111(MRD)} = 4 \frac{\frac{I_{111}}{I'_{111}}}{\frac{I_{111}}{I'_{111}} + 3 \frac{I_{11\bar{1}}}{I'_{11\bar{1}}}} \quad \text{Equation (6)}$$

where, I_{111} and $I_{11\bar{1}}$ are the integrated peak intensities at a given electric field; I'_{111} and $I'_{11\bar{1}}$ are the integrated peak intensities in the virgin state of a random-oriented rhombohedral ferroelectric sample. $f_{111} = 1.0$ MRD indicates that the sample is in the virgin state or there is no domain reorientation at a given electric field; $f_{111} = 4.0$ MRD is the maximum theoretical value that indicates the domain reorientation is saturated in a rhombohedral phase ferroelectric sample at an elevated electric field.

The plot in Figure 3-10 shows the 111 domain texture strength as a function of azimuthal angle. For example, parallel to the macroscopic electric field at 90° azimuthal angle, the $[111]$

polarization direction is preferred by a factor above 3.52 times that found in a random sample, or above 3.52 MRD. It is also instructive to note that the rhombohedral 111 domain texture strength is much higher than the tetragonal 002 domain texture strength. For the domain texture strength in the tetragonal phase Nb-PZT 50/50 sample, the maximum value of the 002 domain alignment is 1.21 MRD, whereas the maximum degree of 111 domain alignment is 3.52 MRD for the rhombohedral phase Nb-PZT 56/44 sample. This is because the rhombohedral phase material has a smaller spontaneous ferroelastic strain and more domain variant options than the tetragonal phase material.

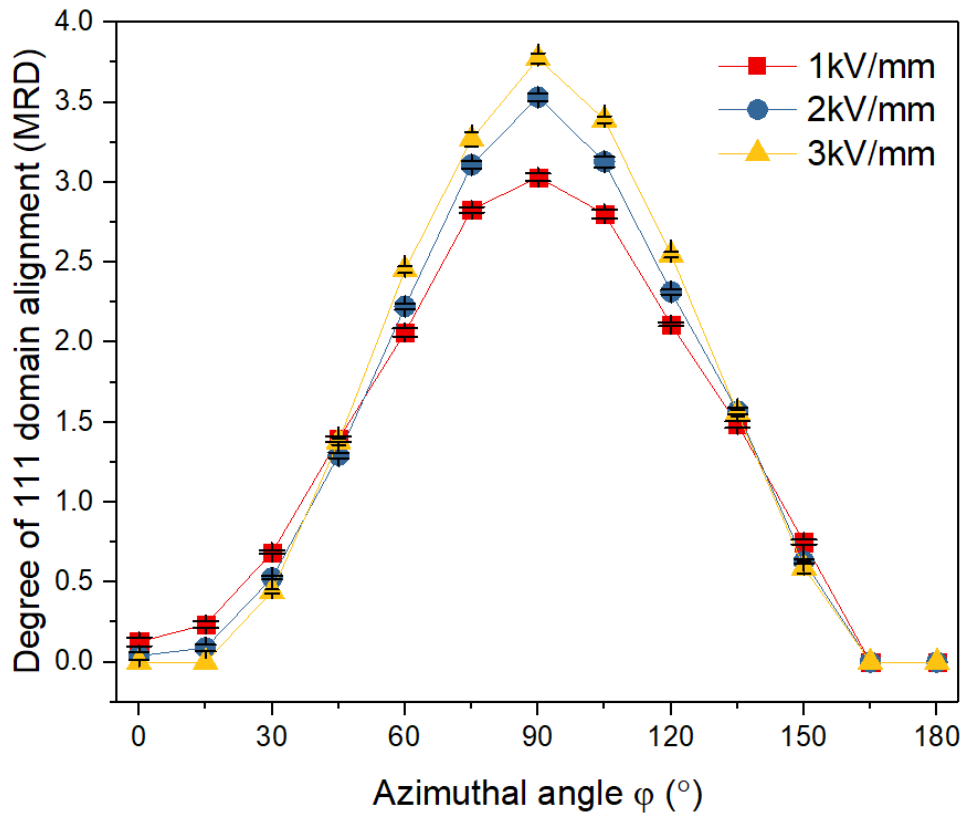


Figure 3-10 The degree of 111 domain alignment of the rhombohedral phase Nb-PZT 56/44 sample with full-electrode configuration at multiple electric field amplitudes along all azimuthal angles.

3.3. KNN-based Materials

3.3.1. Undoped KNN

It is known that the polarization direction in an orthorhombic ferroelectric is parallel to the $\langle hh0 \rangle$ directions, e.g., $\langle 220 \rangle$ directions. Since the orthorhombic structure has three different lattice constants, a , b , c ($a \neq b \neq c$), it is challenging to probe the domain reorientation behaviors from XRD plots with respect to the orthorhombic frame because, for example, the three 220 reflections (202_O , 022_O , and 220_O) are not consecutive in 2θ angles. With the X-ray wavelength fixed at $\lambda = 0.1173 \text{ \AA}$ in beamline 11-ID-C, the 202_O reflection locates at 3.353° , whereas the 022_O and 220_O reflections namely locate at 4.148° and 4.154° in 2θ angle in a 1D XRD plot for the undoped KNN material in its virgin state. From the perspective of crystallographic symmetry, a relationship between the orthorhombic ($Amm2$) and monoclinic (Cm) cells can be established, as illustrated in Figure 3-11. By assuming the lattice constants $a_M = c_M$, where the subscript M denotes the monoclinic frame, an orthorhombic unit cell can be referred to as a pseudo-monoclinic cell by rotating the orthorhombic frame about 45° along the b_O axis [52]. Specifically, the pseudo-monoclinic unit cell volume is approximately half of the orthorhombic cell. As can be described in an alternative structure, domain reorientation behaviors in the orthorhombic phase can be studied in XRD using the pseudo-monoclinic cell reflections.

Table 2 provides a comparison of the calculated lattice parameters in both orthorhombic and pseudo-monoclinic unit cells for the undoped KNN ferroelectric material in the virgin state. As known in a monoclinic phase ferroelectric ceramic, the polarization direction is parallel along the $\langle hh0 \rangle$ orientations, e.g., $\langle 220 \rangle$ directions. Therefore, for the undoped KNN ferroelectric material, the reflection indices with respect to orthorhombic and pseudo-monoclinic unit cell frames are listed in Table 3.

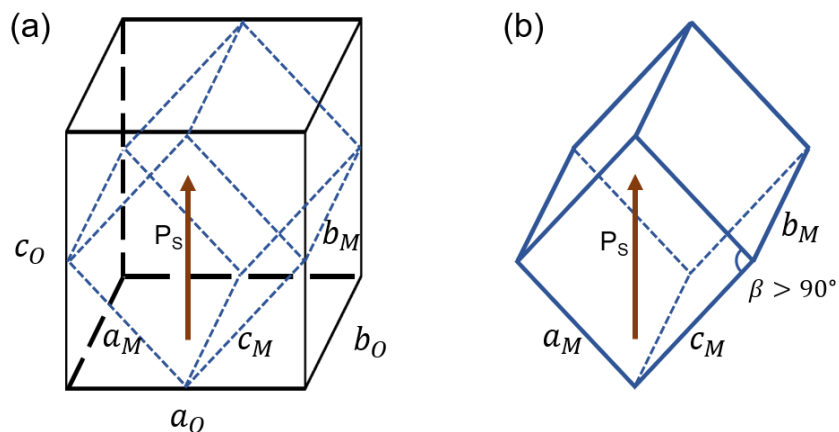


Figure 3-11 Spontaneous polarization directions (P_s) in undoped KNN (a) orthorhombic unit cell and (b) pseudo-monoclinic unit cell.

Table 2 Lattice parameters in undoped KNN material in the virgin state with respect to the orthorhombic and pseudo-monoclinic frames, assuming $a_M = c_M$.

	a (Å)	b (Å)	c (Å)	V (Å ³)	α (°)	β (°)	γ (°)
Orthorhombic	5.656	3.946	5.684	126.86	90	90	90
Pseudo-monoclinic	4.018	3.946	4.018	63.71	90	90.21	90

Table 3 Indices for 220 reflections with respect to the orthorhombic and pseudo-monoclinic frames for undoped KNN material in the virgin state.

Orthorhombic	Pseudo-monoclinic	2θ (°)	d-spacing (Å)
004_O	202_M	4.732	1.421
400_O	022_M	4.770	1.409
222_O	220_M	4.784	1.405

Figure 3-12 presents the intensity interchanges among the 220 reflections as a function of azimuthal angle φ for the undoped KNN material using the pseudo-monoclinic frame. In the virgin state, the intensity of the three reflections is nearly constant at all azimuthal angles. However, with applied electric field of 3 kV/mm, the 202_M peak becomes more intense in the 90° azimuthal angle that is parallel to the macroscopic electric field direction. The increase of 202_M reflection intensity in the 90° azimuthal angle is accompanied with intensity reduction of 022_M and 220_M reflections. These observations from the undoped KNN material are consistent to the results reported from prior work by Iamsasri *et al.* on the Li-doped KNN ferroelectric ceramics, i.e., the domains corresponding to $(202)_M$ planes, or 202 domains, are most preferred under the application of electric field [115].

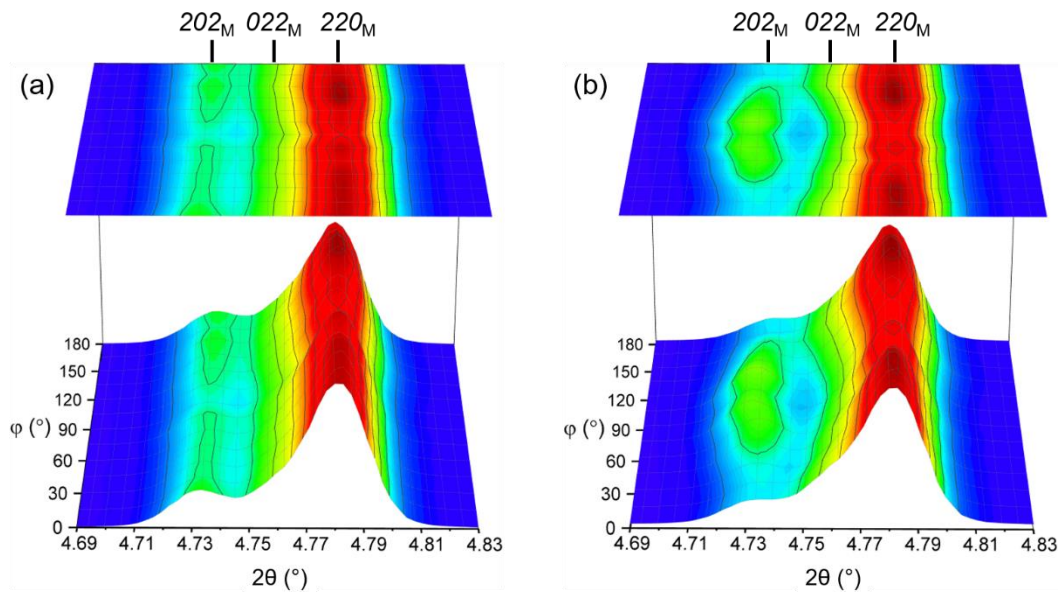


Figure 3-12 Peak intensities as a function of azimuthal angle (φ) for the pseudo-monoclinic (orthorhombic) phase, undoped KNN sample with the full-electrode configuration in (a) the virgin state and (b) 3 kV/mm.

To study the domain reorientation behaviors in an orthorhombic ferroelectric material, Iamsasri *et al.* introduced a method, which calculates the fraction of domain interchange with respect to the pseudo-monoclinic frame between the three different planes instead of calculating the domain texture strength in terms of MRD [115], [116]. Equation (7) describes quantitative interpretation of the fraction of domain interchange, n_{i-j} , from peak i to peak j , under the application of an electric field,

$$n_{i-j} = \frac{R_j - R_i}{R_{202} + R_{022} + R_{220}} \quad \text{Equation (7)}$$

where i, j are indices of reflections 202, 022, and 220; R is the ratio of an integrated reflection intensity at an elevated electric field over the integrated reflection intensity in the virgin state of a random-oriented monoclinic phase ferroelectric sample.

Under the pseudo-monoclinic cell frame, Figure 3-13 shows the fractions of domain interchange among 202, 022, and 220 domains as a function of azimuthal angles at the maximum electric field of 3 kV/mm. Along the 90° azimuthal angle that is parallel to the macroscopic electric field direction, the greatest fraction of domain interchange happens from 022 to 202 domains ($n_{022-202}$), which is followed by the fraction of domain interchange from 220 to 202 domains ($n_{220-202}$). The calculated results indicate quantitatively that the 202 domains are most preferred under the application of electric fields in the pseudo-monoclinic (orthorhombic) phase undoped KNN material. These are important observations that can be used for determining the unique local electric field direction in a scanned pixel for the undoped KNN partial-electrode samples in Chapter 4.

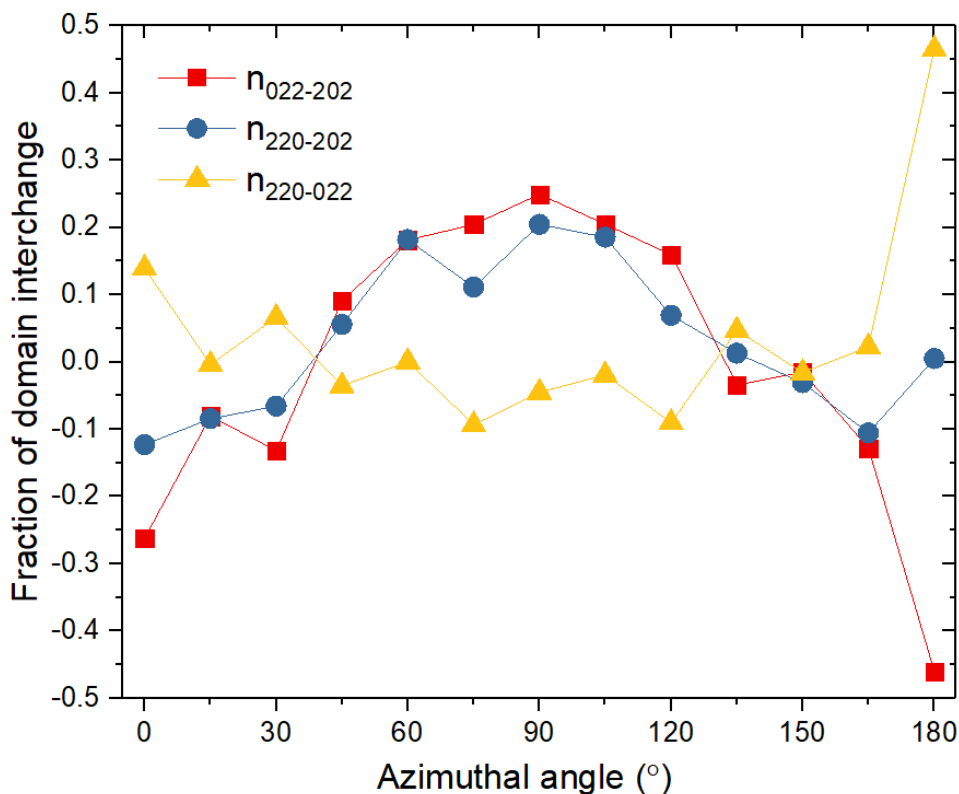


Figure 3-13 The fraction of domain interchange in the pseudo-monoclinic (orthorhombic) phase, undoped KNN sample with the full-electrode configuration as a function of electric field amplitude along all azimuthal angles.

3.3.2. Doped KNN

As introduced earlier, the Li-, Ta- and Mn-doped KNN ferroelectric ceramic has a single tetragonal ($P4mm$) phase at room temperature, for which the domain reorientation behaviors can be studied intensity interchanges between the 002_T and 200_T reflections. Figure 3-14 shows the intensity interchanges of 002_T and 200_T reflections as a function of azimuthal angles. In the virgin state, the 002_T and 200_T reflections are generally separated along all azimuthal angles despite higher intensities at the 90° azimuth. At an elevated electric field of 3 kV/mm, as shown in Figure 3-14(b), the intensity of the 002_T reflection becomes higher along the 90° azimuthal angle that is parallel to the macroscopic field direction in the full-electrode sample. In contrast, the 200_T

reflection decreases drastically in intensity along the 90° azimuthal angle. These observations are characteristic signatures of ferroelectric/ferroelastic domain switching. In comparison with the tetragonal phase Nb-PZT 50/50 that is shown in Figure 3-1, there exist fairly high intensity along the azimuthal angles between the 002_T and 200_T reflections that may be contributed from diffuse scattering of domain walls, which deserves careful peak fitting when performing line profile analysis in LIPRAS.

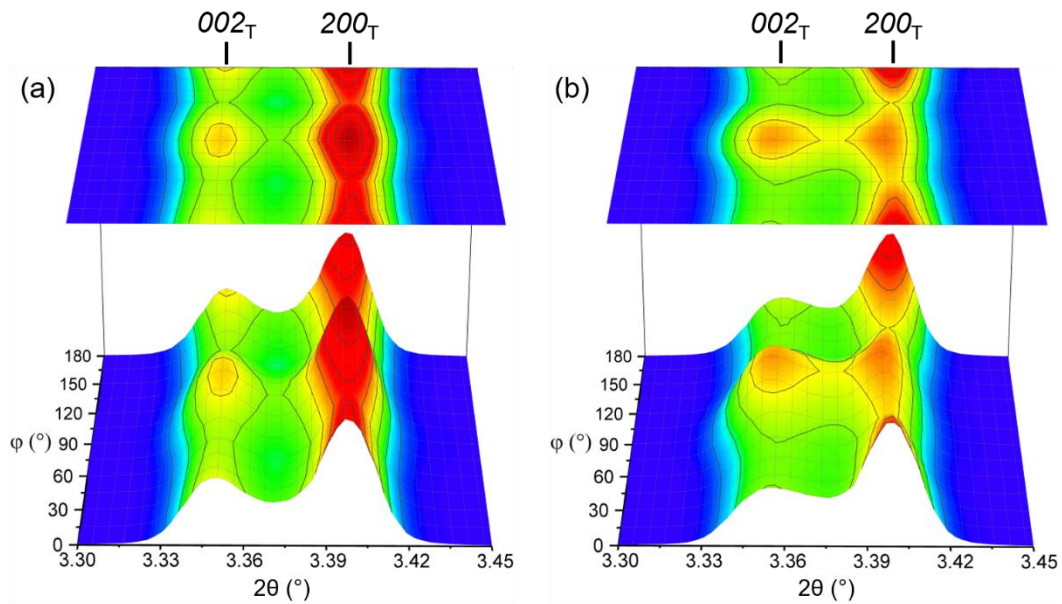


Figure 3-14 Peak intensities as a function of azimuthal angle (ϕ) for the tetragonal phase, doped KNN sample with the full-electrode configuration in (a) the virgin state and (b) 3 kV/mm.

Figure 3-15 provides the calculated the domain texture strength corresponding to the 002_T planes as a function of electric field amplitudes and azimuthal angles. As shown from the plots, along the azimuths approximately parallel to the macroscopic field direction, the 002 domain texture strength becomes stronger as a function of applied electric fields, which is because the polarization direction in tetragonal phase is parallel along the $[001]$ crystallographic orientation. The plot shows that the calculated highest domain texture strength is approximately 1.54 MRD

along the macroscopic field direction, which is higher than the value of 1.21 MRD observed in Nb-PZT 50/50. This is because the doped KNN ceramic has smaller spontaneous ferroelastic strain which permits the domain reorient easier.

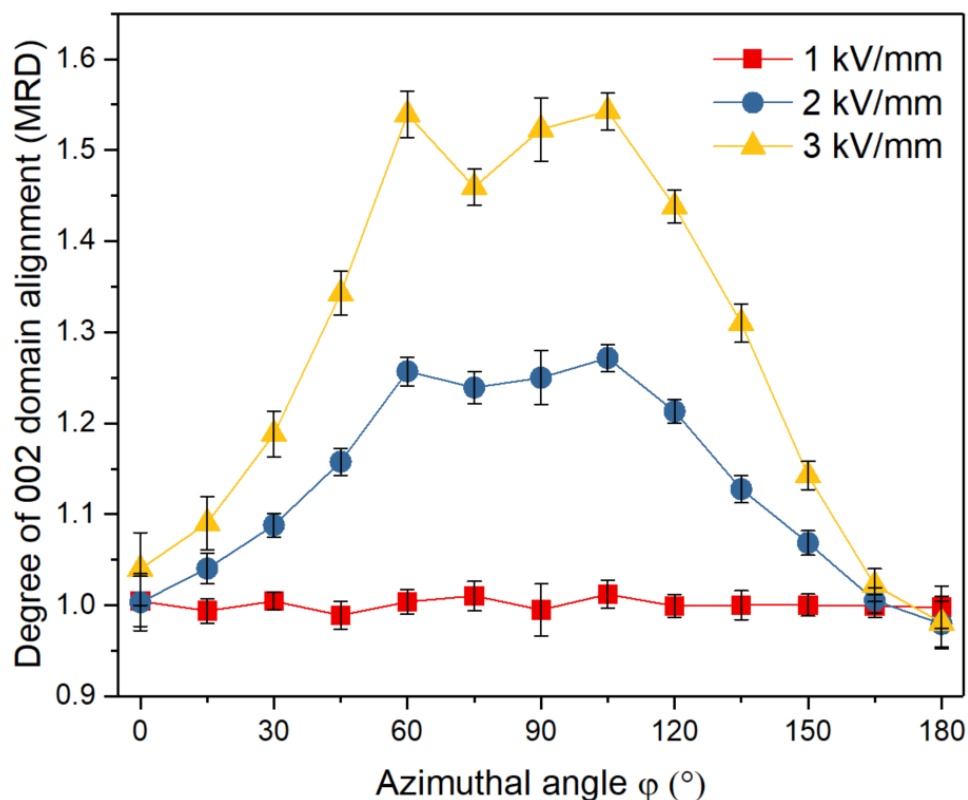


Figure 3-15 The degree of 002 domain alignment of the tetragonal phase, doped KNN sample with the full-electrode configuration at multiple electric fields along all azimuthal angles.

3.4. Summary

This chapter elaborates upon the results from ferroelectric samples with the full-electrode configuration which were examined in synchrotron-based *in situ* high-energy XRD experiments at beamline 11-ID-C, APS. With a high voltage applied to a fully electroded ferroelectric sample, the electric field between the top and bottom electrodes is expected to be homogeneous, i.e. uniform electric field direction and amplitude. The experiment utilized an intense monochromatic X-ray beam in size of 500 μm x 500 μm to scatter the middle of the sample, which helped

investigate microstructural changes in the materials in response to different field amplitudes. With the employment of a PerkinElmer 2D area detector, the experiment enables the characterization of orientation-dependent material behaviors for ferroelectric ceramics with differed crystallographic phases. To study the ferroelectric/ferroelastic domain reorientation, the degree of domain alignment corresponding to $\{200\}$ and $\{111\}$ planes are calculated for tetragonal phase and rhombohedral phase samples, respectively. More specifically, the most preferred 002 domain orientation in a tetragonal phase material, including Nb-PZT 50/50, Nb-PZT 53/47, and doped KNN samples, is parallel to the macroscopic direction of applied electric field; the most preferred 111 domain orientation in a rhombohedral phase, i.e., in the Nb-PZT 56/44 composition, is also parallel to the macroscopic field direction. Furthermore, the fraction of domain interchange is determined for the orthorhombic sample, i.e., undoped KNN ferroelectric ceramic in this research. Along the macroscopic direction of the applied electric field, it shows that the domains corresponding to $(202)_M$ reflections most preferred, which is consistent with the observations by Iamsasri *et al* [115].

In addition to the study of domain reorientation, this chapter particularly discusses the results from lead-based Nb-PZT 53/47, which is a ferroelectric PZT composition near the MPB region that is initially in a single tetragonal ($P4mm$) phase. However, the material experiences an orientation-dependent phase transition in selective azimuthal angles into co-existing tetragonal ($P4mm$) and rhombohedral ($R3m$) phases during and after electric field application. Specifically, with increasing the electric field magnitude to 7 kV/mm, the phase transition behavior is dramatically amplified. More specifically, the role of crystal orientation on the phase selection process is elucidated, as shown in Figure 3-6. The results prove that a complete orientation-dependent characterization method is needed to sufficiently observe and characterize the phase

changes. It is only some crystal orientations that change phases, for example an orientation where the [110] or [111] direction of a tetragonal phase crystal is parallel to the macroscopic field direction. In single crystals, these orientations are sometimes called “domain engineered” because they do not exhibit domain switching. The observations in the Nb-PZT 53/47 composition highlight that these selective orientations can change phases as a way to deform in a polycrystal. Another way to emphasize the importance of this effect is to say that, if this experiment were conducted in a conventional laboratory-based X-ray diffractometer, this orientation-dependent phase transition would be invisible.

Chapter 4: Inhomogeneous Electric Field-Induced Material Behaviors

4.1. Overview

This chapter presents results from the partially electroded ferroelectric samples, including both lead-based and lead-free materials demonstrated in Chapter 3. The partial-electrode samples were examined using two different scan patterns, namely “whole bar scan” pattern and “electrode edge scan” pattern, as illustrated in Figure 2-1(b) and (c). The results about orientation-dependent and position-sensitive domain reorientation and phase transitions induced by inhomogeneous electric fields are demonstrated.

4.2. Whole Bar Scan

In the whole bar scan experiments on the ferroelectric partial-electrode samples, the monochromatic high-energy X-ray beam scattered the sample successively at various positions in each applied electric field amplitude. The scanned pixels are labeled, as shown in Figure 4-1, to better describe the experimental results in this section. Take P_{2-10} for instance, “P” is short for pixel, the subscription “2-10” stands for the pixel position in the “2nd row and 10th column”. Under the application of an external voltage, the electric field is expected to be spatially-dependent throughout the partial-electrode sample. More specifically, on the right side of the sample, between the electrodes, the pixels are expected to experience more homogeneous electric fields. This region covered with top and bottom electrodes can be referred to as the “active region”. However, on the left side of the sample, outside the full-electrode region, the pixels are expected to undergo inhomogeneous electric fields or unique local electric fields. The region that is only covered with bottom electrode is called “passive region”, which is also referred to as “dead zone”.

					Electrode				
P_{1-1}	P_{1-2}	P_{1-3}	P_{1-4}	P_{1-5}	P_{1-6}	P_{1-7}	P_{1-8}	P_{1-9}	P_{1-10}
P_{2-1}	P_{2-2}	P_{2-3}	P_{2-4}	P_{2-5}	P_{2-6}	P_{2-7}	P_{2-8}	P_{2-9}	P_{2-10}

Figure 4-1 The whole bar scan pattern in ferroelectric partial-electrode samples with labeled pixels.

4.2.1. Nb-PZT-based Materials

As demonstrated in Chapter 3, under the application of a homogeneous electric field, the full-electrode ferroelectric samples exhibit the strongest domain texture in the 90° azimuthal angle, which is parallel to the macroscopic direction of the applied electric field. However, since the pixels in the passive region are expected to undergo unique local electric fields, the strongest domain texture should align along a unique azimuthal angle in each pixel. By determining the most preferred domain orientation, the local electric field direction in each scanned pixel can be quantitatively inferred.

Take the Nb-PZT 50/50 partial electrode sample, which has a single tetragonal phase in the virgin state, as an example for demonstrating the analysis process. Under the homogeneous electric field, as presented in Figure 3-2, the fully electroded Nb-PZT 50/50 sample shows the most preferred 002 domain texture along the macroscopic direction of applied electric field with a quantified texture strength of 1.21 MRD. In the Nb-PZT 50/50 partial-electrode sample, the 002 domain texture strength is calculated for each scanned pixel at different applied electric fields. By doing so, the local electric field direction can be inferred by locating the azimuthal angle with the strongest 002 domain texture. Take P_{2-10} in the active region, P_{1-5} next to the electrode edge, and P_{1-1} in the passive region for examples. The three pixels are used as representative pixels

illustrating the results for both Nb-PZT and KNN-based partial electrode samples that were examined in the “whole bar scan” pattern. As seen from Figure 4-2(a), the 002_T and 200_T reflections generally have constant intensities in all azimuthal angles in the virgin state for P_{2-10} . However, with the electric field elevated to 3 kV/mm, as shown in Figure 4-2(d), the 002_T reflection exhibits the highest intensity in the 90° azimuthal angle and weakest intensity in the 0° and 180° azimuthal angles. In contrast, the 200_T reflection behaves in the opposite way. The comparison in Figure 4-2 suggests that the local electric field in P_{2-10} is parallel to the macroscopic direction of applied electric field.

P_{1-5} locates in the passive region that is close to the top electrode edge, where is expected to undergo a unique local electric field. Figure 4-2(b) and (e) present peak intensity changes at all azimuthal angles obtained from P_{1-5} in the tetragonal phase Nb-PZT 50/50 partial-electrode sample for its virgin state and 3 kV/mm, respectively. In comparison with the virgin state, the reflections have obvious intensity interchanges at an elevated electric field of 3 kV/mm. However, as seen in Figure 4-2(e), the highest 002_T intensity appears in the lower 30° azimuthal angle. It suggests the direction of local electric field in P_{1-5} is parallel to the 30° azimuthal angle, i.e., 60° away from the macroscopic direction of the applied electric field.

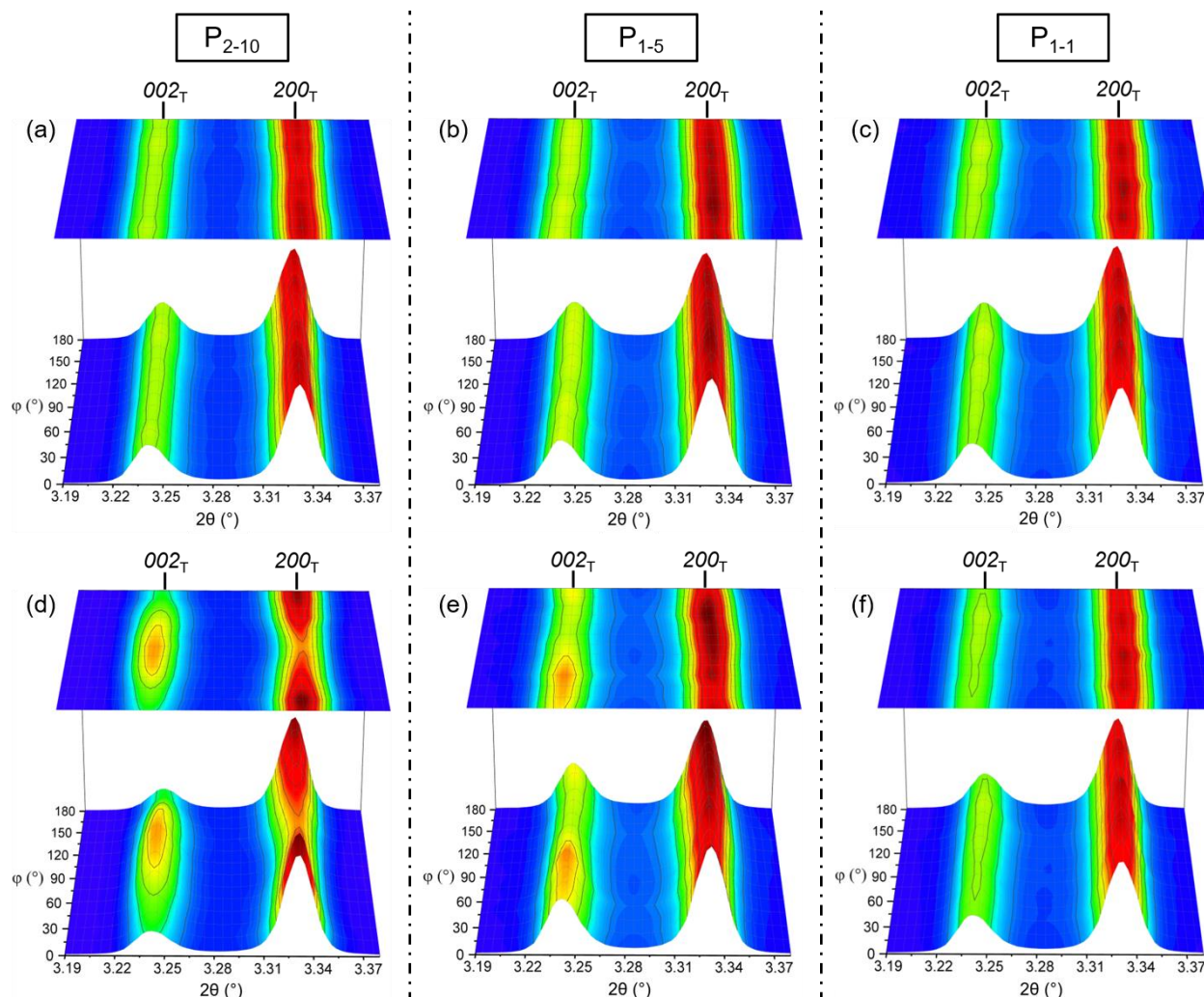


Figure 4-2 Peak intensities as a function of azimuthal angle (ϕ) for P_{2-10} , P_{1-5} , and P_{1-1} in the tetragonal phase Nb-PZT 50/50 partial-electrode sample with the whole bar scan pattern. Plots (a), (b), (c) present the peak intensities in the virgin state, and (d), (e), (f) show the interchanged intensities at 3 kV/mm for P_{2-10} , P_{1-5} , and P_{1-1} , respectively.

Though the local field direction can be inferred by the azimuthal angle that exhibits the highest intensity of 002_T reflection, the determination can be challenging if the electric field amplitude is not strong enough, resulting in a less obvious domain texture exhibited on the XRD plots. For example, as shown in Figure 4-2(c) and (f), the intensity interchanges between 002_T and 200_T reflections are less significant between the virgin state and poled state, which is because that P_{1-1} locates at the corner in the passive region of the partial electrode sample and undergoes a

negligible local electric field. Such a situation makes it difficult to determine the local electric field direction from the contour plots.

As previously stated in Equation (5) from Chapter 3, the most preferred domain orientation can be quantitatively calculated in terms of MRD for the tetragonal phase. The calculations are performed for the data collected from each individual pixel in the ferroelectric partial-electrode sample at each applied electric field amplitude. As shown in Figure 4-3, the 002 domain texture strength is calculated for these three representative pixels from the tetragonal phase Nb-PZT- 50/50 partial electrode sample in the maximum electric field amplitude of 3 kV/mm. The figure presents reasonable a small error for each data point collected at different azimuthal angles. For P₂₋₁₀, it shows that the highest degree of domain alignment appears in the 90° azimuthal angle that is parallel to the macroscopic direction of the applied electric field. In addition, the highest degree of 002 domain alignment in P₁₋₅ is shown parallel along the 30° azimuthal angle. However, the calculated degree of 002 domain alignment for P₁₋₁ is approximately of one for all azimuthal angles, with the maximum $f_{002} = 1.01$ MRD along the 105° orientation. This evidences that, with an external high-voltage applied to the tetragonal phase Nb-PZT 50/50 partial-electrode sample, the domain reorientation is negligible in P₁₋₁ because of the inappreciable local electric field. These quantitatively calculated results of orientation-dependent domain texture strength for the three representative pixels are consistent with the observations from the contour plots shown in Figure 4-2, suggesting that the field-induced domain reorientation strongly depends on the local electric field directions and amplitudes.

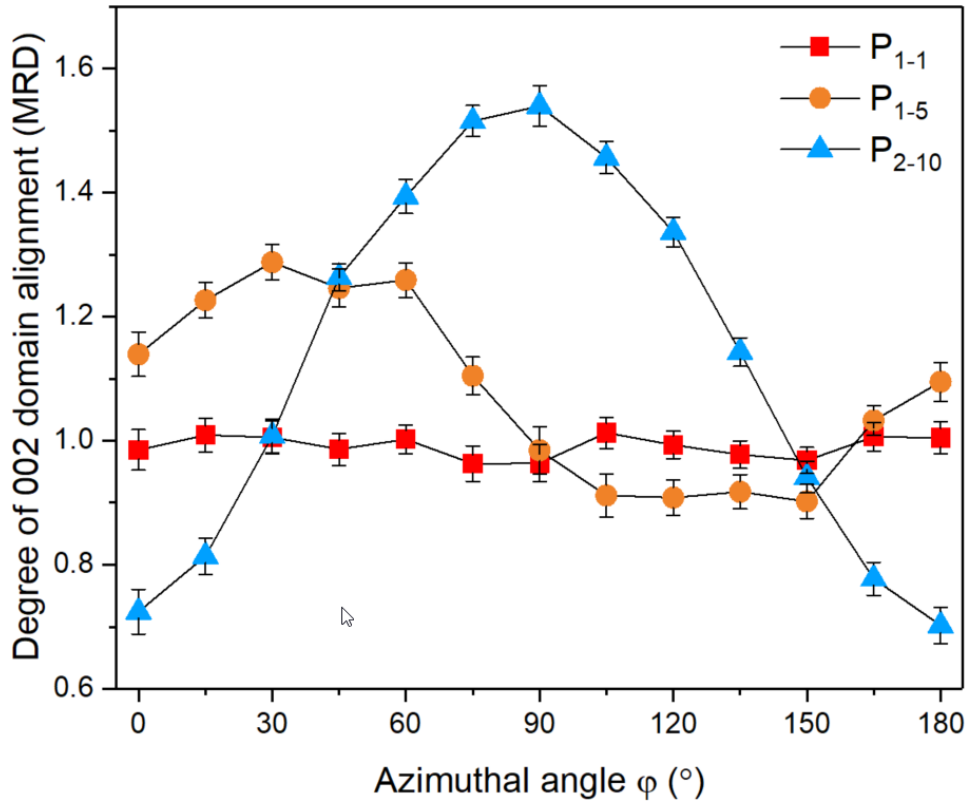


Figure 4-3 The degree of 002 domain alignment (MRD) of representative pixels P_{2-10} , P_{1-5} , and P_{1-1} in the tetragonal phase Nb-PZT 50/50 partial-electrode sample with the whole bar scan pattern at 3 kV/mm.

With the macroscopic electric field of 3 kV/mm applied to the tetragonal phase Nb-PZT 50/50 partial-electrode sample, the local electric field direction in each individual pixel can be inferred by computing its maximum extent of 002 domain alignment, f_{002} . Figure 4-4(a) shows the computed maximum f_{002} for each scanned pixel in the Nb-PZT 50/50 partial-electrode sample at the macroscopic electric field of 3 kV/mm. The color represents the maximum calculated 002 domain texture strength in each scanned pixel. The darker the color, the higher the domain texture strength in the pixel. The arrows represent the local electric field inferred from the calculation, where the direction of an arrow stands for the field direction in a pixel. Moreover, the arrow lengths are linearly linked with values shown in the legend.

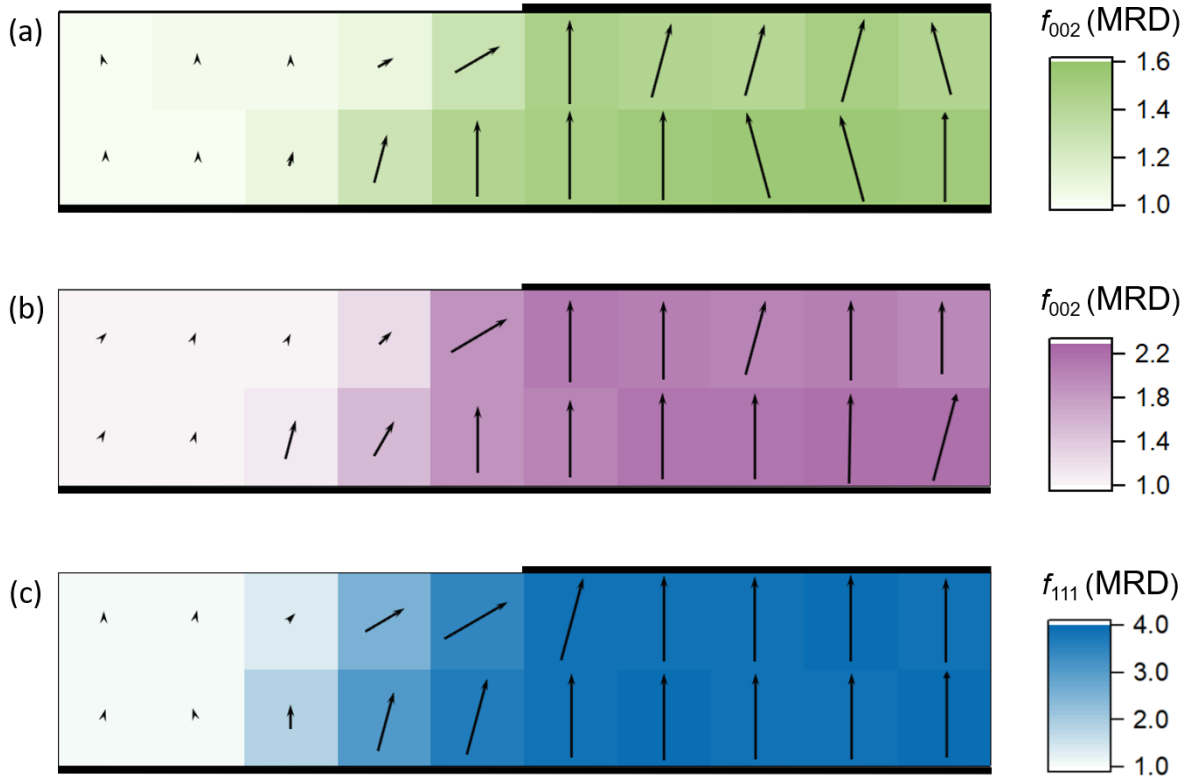


Figure 4-4 Under the application of 3 kV/mm, the calculated maximum domain texture strength in each scanned pixel for the partial-electrode samples with lead-based composition of (a) Nb-PZT 50/50, (b) Nb-PZT 53/47, and (c) Nb-PZT 56/44.

Additionally, Figure 4-4(b) and (c) present the calculated maximum domain texture strength for the Nb-PZT 53/47 and Nb-PZT 56/44 partial-electrode samples, respectively. Appendix C includes supplementary figures of contour plots and calculated domain texture strength at all azimuthal angles for the representative pixels, P_{2-10} , P_{1-5} , and P_{1-1} in the partial-electrode samples, to observe intensity interchanges of 200 and 111 reflections as well as texture preferences for the latter two lead-based compositions in Figure 4-4. Appendix D present summarized tables of computed maximum domain texture strength and inferred local field orientation in each pixel for the samples in Figure 4-4.

As shown in Figure 4-4 for the three Nb-PZT-based partial-electrode samples, the color changes throughout the samples are quite analogous, meaning that the inhomogeneous electric

field-induced domain reorientation behaviors between the top and bottom electrodes are similar despite of composition and phase for Nb-PZT-based ferroelectric materials. Specifically, for a partial-electrode sample, in the active region underneath the top electrode, the colors are alike due to the homogeneous electric fields. However, in the passive region or dead zone, the color intensity starts to fade because the local electric fields are weaker. The arrows that represent the most preferred domain orientation also change, reflecting the direction of the local electric field in each scanned pixel.

4.2.2. KNN-based Materials

Lead-free undoped and doped KNN-based partial-electrode samples were also examined in the *in situ* high-energy XRD experiment using the whole bar scan pattern at beamline 11-ID-C, APS. As discussed earlier, the undoped KNN material has a single orthorhombic phase ($Amm2$) that can be described by using the pseudo-monoclinic (Cm) frame. Under the application of a homogeneous electric field in the full-electrode sample, the fraction of domain interchange is computed for the undoped KNN material, showing the most preferred 202 domain texture parallel along the 90° azimuthal angle, i.e. the macroscopic field direction. However, like what have been observed in the Nb-PZT-based partial-electrode samples, the electric field is expected to be inhomogeneous in the KNN-based partial-electrode samples.

Figure 4-5 presents the intensity interchanges among 202_M , 022_M , and 220_M reflections for three representative pixels in the partial-electrode sample, namely P_{2-10} in the active region, P_{1-5} next to the top electrode edge, and P_{1-1} at the corner in the passive region. In the virgin state, as seen from Figure 4-5(a)-(c), the three representative pixels generally have constant intensity of 202_M , 022_M , and 220_M reflections in all azimuthal angle. With a macroscopic electric field of 3kV/mm applied to the undoped KNN partial-electrode sample, the peak intensity changes

differently for the three representative pixels. As seen from Figure 4-5(d) for P_{2-10} , the strongest 202 domain texture is shown in the 75° azimuthal angle that is approximately parallel to the macroscopic field direction. This is because P_{2-10} locates in the active region between electrodes in the partial-electrode sample that is expected to experience a homogeneous electric field.

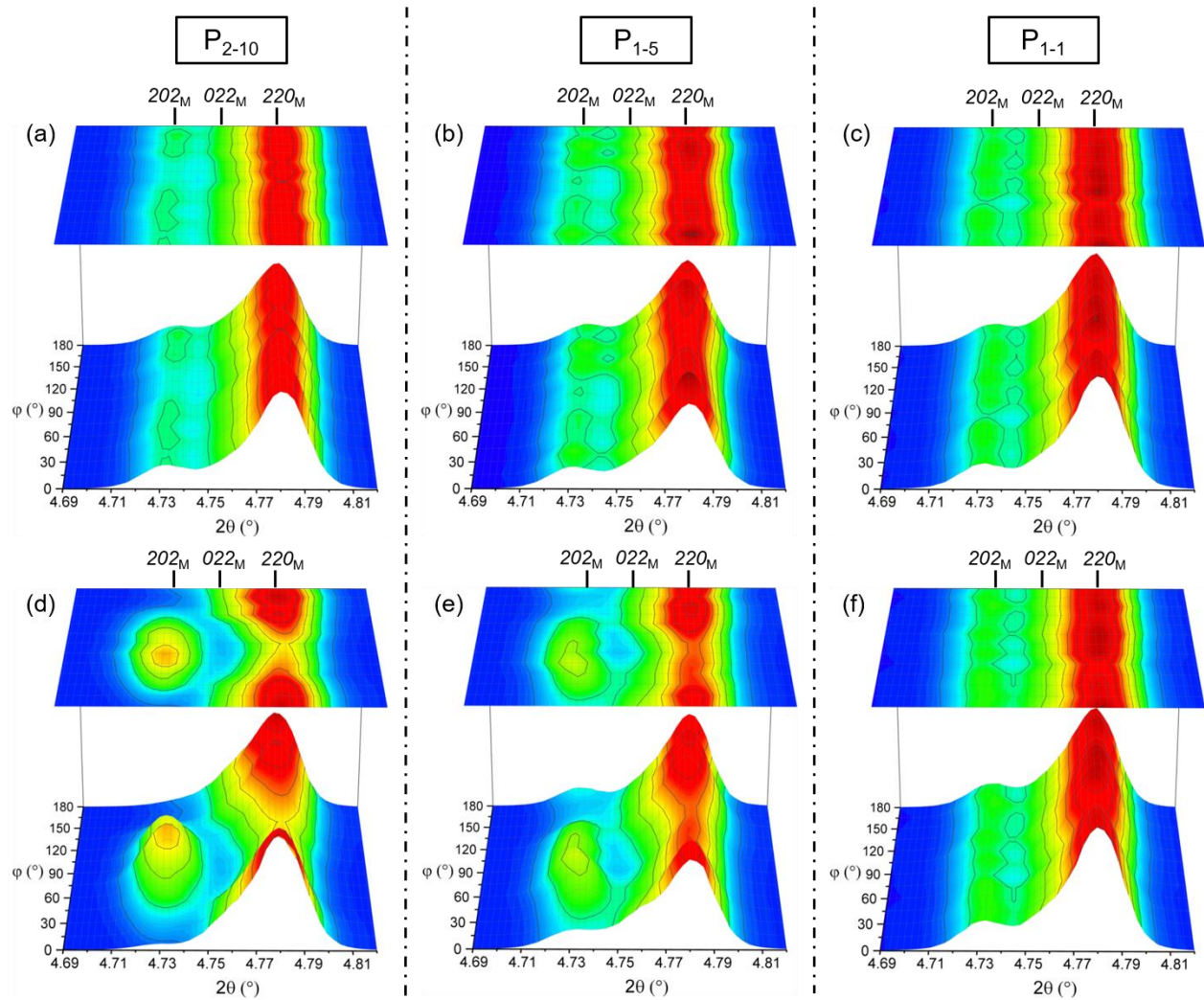


Figure 4-5 Peak intensities as a function of azimuthal angle (φ) for P_{2-10} , P_{1-5} , and P_{1-1} in the pseudo-monoclinic (orthorhombic) phase, undoped KNN partial-electrode sample with the whole bar scan pattern. Plots (a), (b), (c) present the peak intensities in the virgin state, and (d), (e), (f) show the interchanged intensities at 3 kV/mm for P_{2-10} , P_{1-5} , and P_{1-1} , respectively.

In comparison with P_{2-10} , the domain reorientation in P_{1-5} is much weaker as illustrated among peak intensity interchanges in Figure 4-5(e). Specifically, the maximum intensity of 202_M reflection in P_{1-5} is not as strong as observed in P_{2-10} , suggesting that the local electric field in P_{1-5} is weaker than that in P_{2-10} . In addition, as shown in Figure 4-5(e), the most preferred 202 domain orientation is changed to a lower 60° azimuthal angle in the macroscopic electric field of 3 kV/mm. These observations in P_{1-5} suggest that the local electric field amplitude is lower than 3 kV/mm with a field direction towards the electrode edge, which is similar to the result concluded from Nb-PZT-based partial-electrode samples. As for P_{1-1} , in comparison with its virgin state shown in Figure 4-5(c), there is little peak intensity changes at an elevated macroscopic electric field as seen from Figure 4-5(f). This is because P_{1-1} locates at the corner in the passive region, where is expected to undergo the least electric field throughout the partial-electrode sample.

To quantitatively determine the local electric field in each scanned pixel, fraction of domain interchange, including $n_{022-202}$, $n_{220-202}$, and $n_{220-022}$, are computed for all azimuthal angles and macroscopic electric field amplitudes. As discussed in Chapter 3, the 202 domains are most preferred along the electric field direction in a pseudo-monoclinic (orthorhombic) phase KNN material. Under the application of an electric field, both 022 and 220 domains tend to reorient, resulting in an increase of 202 domain volume. Therefore, the local electric field direction in a scanned pixel can be inferred by observing the unique azimuthal angle that exhibits the highest fraction of domain interchange from 022 to 202 domains, i.e., $n_{022-202}$, or the highest fraction of domain interchange from 220 to 202 domains, i.e., $n_{220-202}$. For the undoped KNN partial-electrode sample, both $n_{022-202}$ and $n_{220-202}$ are calculated to determine and compare the local electric field direction for each pixel. Figure 4-6 presents the computed $n_{022-202}$ and $n_{220-202}$ at all azimuthal angles for the representative pixels with a macroscopic electric field of 3 kV/mm. For P_{2-10} that locates in

the active region, as shown in Figure 4-6(a), the calculated $n_{022-202}$ and $n_{220-202}$ both have the highest value along the 75° azimuthal angle, which quantitatively suggests the local electric field direction is approximately parallel along the macroscopic field direction. This is consistent with observations from the contour plot shown in Figure 4-5(d) for P_{2-10} . Figure 4-6(b) provides the computed fractions of domain interchange for P_{1-5} along different crystallographic orientations, showing the highest $n_{022-202}$ and $n_{220-202}$ along 60° and 75° azimuthal angle, respectively. Figure 4-6(c) shows the calculated fractions of domain interchange in P_{1-1} with respect to azimuthal angle. The computed $n_{022-202}$ and $n_{220-202}$ both show similar small values along all azimuthal angles, suggesting the local electric field amplitude in P_{1-1} is weaker than the other investigated pixels.

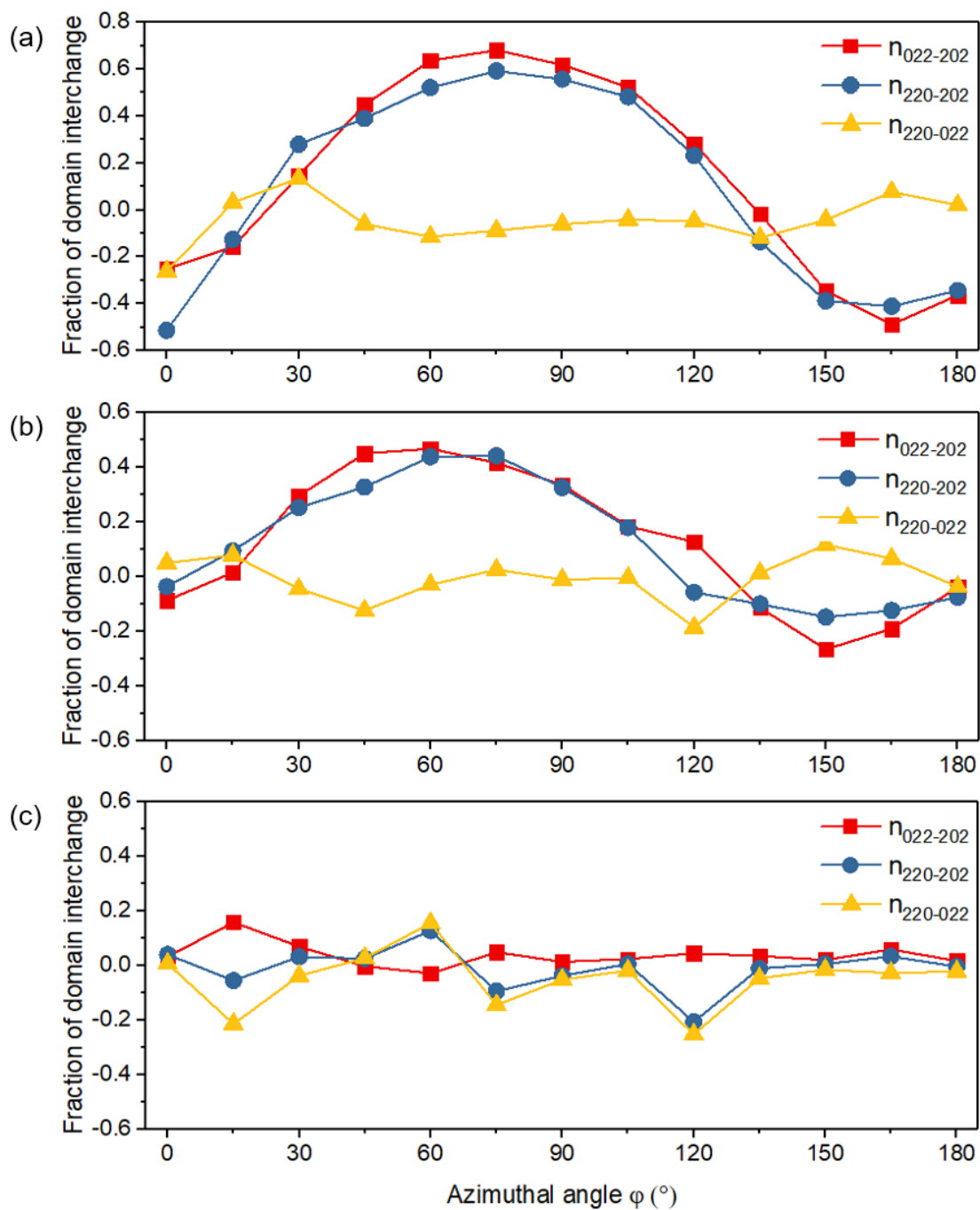


Figure 4-6 Fraction of domain interchange in representative pixels (a) P₂₋₁₀, (b) P₁₋₅, and (c) P₁₋₁ in the pseudo-monoclinic (orthorhombic) phase, undoped KNN partial-electrode sample with the whole bar scan pattern at 3 kV/mm.

Figure 4-7 presents the maximum $n_{022-202}$ and $n_{220-202}$ in each scanned pixel with a macroscopic electric field of 3 kV/mm applied to the undoped KNN partial-electrode sample. The color intensity reflects the calculated maximum extent of 202 domain texture strength while the arrow direction represents the angular orientation of the strongest domain alignment, suggesting that it is the direction of local electric field within a scanned pixel. In the undoped KNN partial-electrode sample, similar phenomena are observed in Nb-PZT-based materials: The data in the active region (between top and bottom electrodes) on the right-hand side is generally uniform, whereas data in the passive region on the left-hand side evidences the change in local electric field direction and decreased fraction of domain interchange. However, comparing to Nb-PZT-based partial-electrode samples, the data in the passive region exhibit a more homogeneous trend.

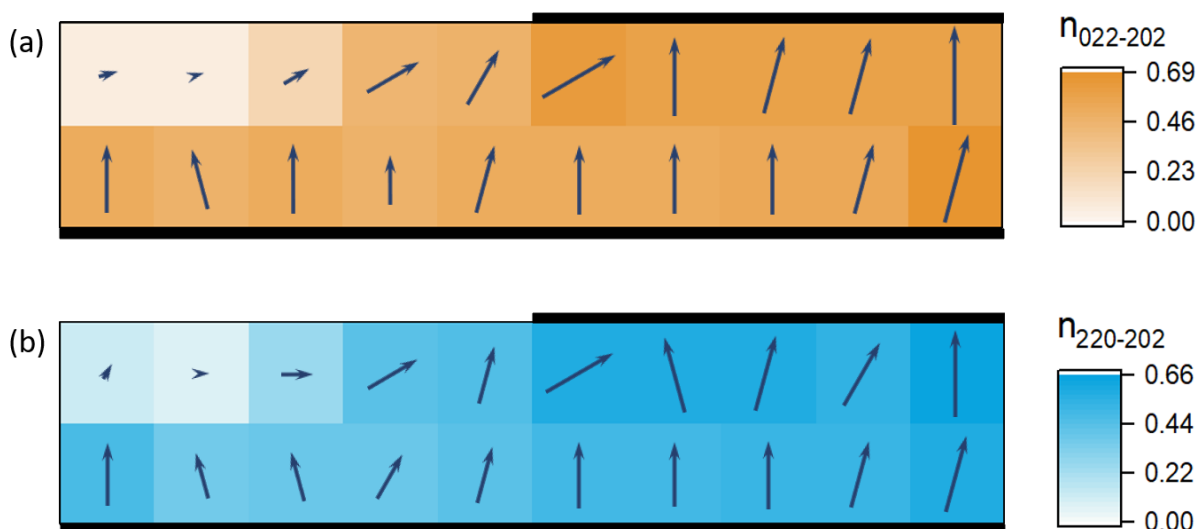


Figure 4-7 Under the application of 3 kV/mm, the calculated maximum fraction of domain interchange (a) $n_{022-202}$, and (b) $n_{220-202}$, in each scanned pixel for the pseudo-monoclinic (orthorhombic) phase, undoped KNN partial-electrode sample with the whole bar scan pattern.

While the previously introduced KNN sample was undoped, the following content in this section will focus on elaborations upon results from a (Li, Ta, Mn)-doped KNN partial-electrode sample. As discussed in Chapter 3 with the homogeneous electric field application, this doped

KNN material has a single tetragonal ($P4mm$) phase that shows the most preferred 002 domain orientation along the macroscopic field direction. The doped KNN partial-electrode sample was also examined using the same experimental setup with the whole bar scan pattern as applied to the other ferroelectric materials. Figure 4-8 presents the computed maximum degree of 002 domain alignment in each scanned pixel under the application of 3 kV/mm. The result shows that the domain switching behavior is orientation-dependent near the top electrode edge, i.e., electrode termination region. In the active region between the electrodes, the most preferred 002 domain orientation is more parallel to the macroscopic field direction despite slightly differed texture strength. In the passive region, the calculated degree of 002 domain alignment is not strong, suggesting the local electric field is weak. For more information, Appendix C provides contour plots for representative pixels, and Appendix D shows a summarized table of maximum f_{002} and inferred local field direction for all scanned pixels in the doped KNN partial-electrode sample.

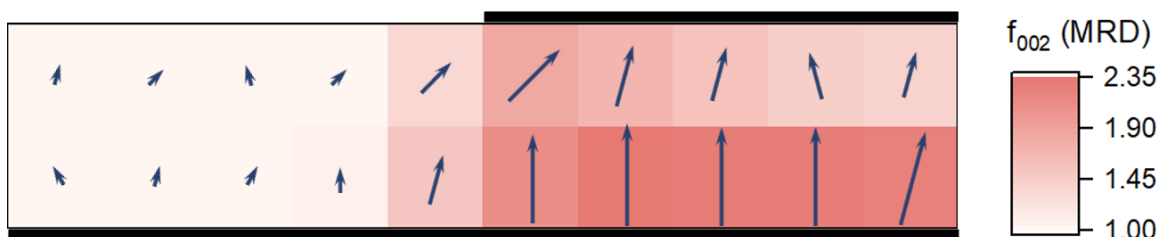


Figure 4-8 Under the application of 3 kV/mm, the calculated maximum 002 domain texture strength in each scanned pixel for the tetragonal phase, doped KNN partial-electrode sample with the whole bar scan pattern.

4.2.3. Discussion

The partial-electrode samples were tested in beamline 11-ID-C at APS by a high-energy X-ray beam to scan the sample at various positions and multiple electric field amplitudes. From the study of full-electrode samples in Chapter 3, it is concluded that the most preferred domain orientation is parallel along the 90° azimuthal angle, which is the direction of macroscopic electric

field. However, for both lead-based Nb-PZT and lead-free KNN partial-electrode samples, the domain reorientation behavior is evidenced to be orientation-dependent and spatially dependent. For the data obtained from a partial electrode sample, the most preferred domain orientation is computed for each scanned pixel to infer the local electric field direction. For the investigated partial-electrode samples, Appendix C shows more contour plots and domain texture strength quantification at all azimuthal angles for representative pixels and Appendix D provides summarized tables of the highest domain texture strength or maximum fraction of domain interchange with their corresponding azimuthal angles.

In general, for all ferroelectric partial-electrode samples (lead-based and lead-free) examined in beamline 11-ID-C using the whole bar scan pattern, the results illustrate that the domain texture strength in the active region (between the electrodes) is more homogeneous due to a homogeneous electric field. Moreover, the domain reorientation in the electrode termination region shows a strong orientation-dependent behavior, suggesting the local electric fields near the electrode edge are quite inhomogeneous. In the passive zone (outside the fully electroded region), the local electric fields are proved to be weak. The arrows that represent the most preferred domain orientation also change, reflecting the direction of the local electric field.

Besides the synchrotron-based high-energy XRD experiments performed in beamline 11-ID-C, finite element analysis (FEA) was also carried out on partial-electrode samples in order to predict the electric field inhomogeneity throughout the sample. FEA was conducted using ANSYS software with its microelectromechanical systems (MEMS) extension, which simulated the electric field distribution in a 2D partial-electrode sample of the same geometry used in a synchrotron-based XRD experiment. To compare the difference of electric field distribution between a lead-based and a lead-free partial-electrode sample, FEA was performed individually

using properties of a commercial ferroelectric material PZT-5A from Ref. [117] and properties of a KNN-based single crystal from Ref. [118].

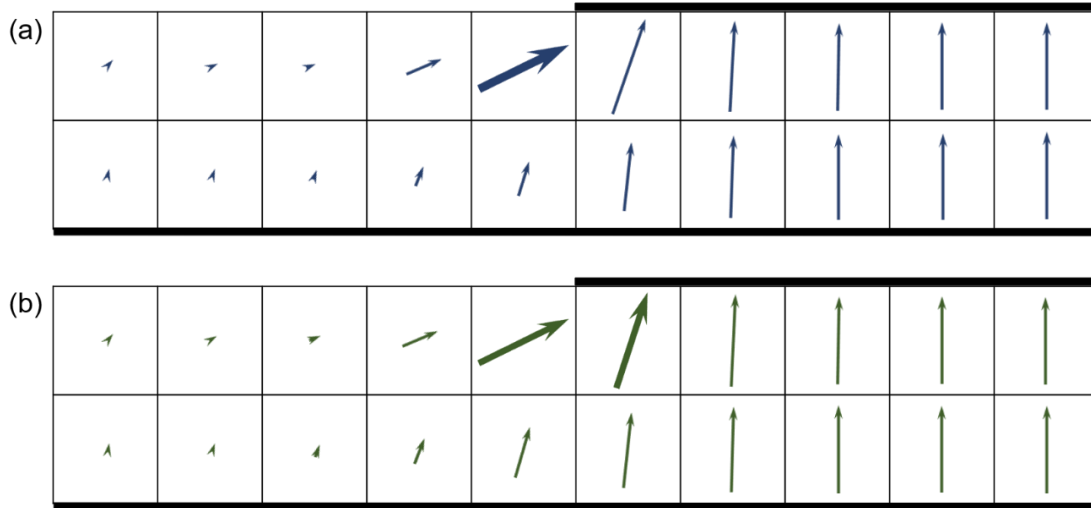


Figure 4-9 FEA results of simulated local electric field vector for each pixel in a (a) Nb-PZT-based, and a (b) KNN-based partial-electrode sample. The macroscopic electric field is set as 3 kV/mm in the simulation. Courtesy of Stephen Funni for the FEA work.

Figure 4-9(a) and (b) show the averaged electric field vector for each scanned pixel in the Nb-PZT-based and KNN-based partial-electrode samples, respectively. In each pixel shown in Figure 4-9, the direction of a vector represents the local electric field orientation, and the length of a vector (except for bold vectors) linearly links with the simulated field amplitude. For the FEA result of a Nb-PZT-based partial-electrode sample, as shown in Figure 4-9(a), the simulated field amplitude is in a wide range between 0 and 100.6 keV. However, except for that the bold electric field vector in P_{1-5} is 100.6 kV/mm, the highest field magnitude in the other pixels is less than 3.6 kV/mm. This is suggesting that there is an expected high-electric field concentration next to the electrode edge in a Nb-PZT-based partial-electrode sample. As for the KNN-based partial-electrode sample, the two bold electric field vectors in P_{1-5} and P_{1-6} namely has a magnitude of 6.7 kV/mm and 6.1 kV/mm, respectively, and the rest pixels commonly have a field magnitude

less than 3.1 kV/mm. As shown in Figure 4-9, the simulated electric fields in the active region are more aligned to parallel along the macroscopic field direction, i.e., homogeneous electric fields. However, in the passive region, the simulated electric fields in pixels are orientation-dependent and spatially dependent.

Figure 4-10(a) presents correlations between the quantitatively calculated domain texture strength and the simulated electric field amplitudes from FEA work. As seen from the figure, for tetragonal phase materials, including Nb-PZT 50/50, Nb-PZT 53/47, and doped KNN, their computed domain texture strength is linearly linked with the simulated field amplitudes from the same probed pixel. Specifically, all three tetragonal phase materials exhibit domain texture strength lower than the saturation limit, i.e., $\max f_{002}=3.0$ MRD. As for the rhombohedral phase Nb-PZT 56/44, the calculated domain texture strength also shows a linear correlation with the simulated field amplitude less than 2 kV/mm. Due to the maximum $f_{111} = 4.0$ MRD in a rhombohedral phase material, the domain texture strength tends to saturate when the electric field goes above 2 kV/mm in Nb-PZT 56/44. This is because a rhombohedral phase material has more domain variant options and a smaller ferroelastic strain than the tetragonal phase, resulting in easier domain reorientation.

Figure 4-10(b) shows correlations between the fraction of domain interchange and simulated electric field magnitude from FEA. The two fraction parameters, $n_{022-202}$ and $n_{220-202}$, present non-linear correlations with the simulated electric field magnitudes. However, it is observed that either fraction parameter has values fluctuate around 0.5 at all simulated field amplitudes. From Figure 4-7, the orthorhombic phase undoped KNN partial-electrode sample shows similar color intensity for domain fraction interchange in the passive region, suggesting a less heterogeneous domain reorientation behavior. However, as simulated field vectors shown in

Figure 4-9(b), the electric field amplitudes in the passive region are apparently non-uniform. This could be the reason that experiment result and simulation data is not linearly correlated.

Figure 4-11 provides correlations between experiment inferred electric field direction and simulated field angle from FEA for probed pixels for (a) Nb-PZT-based and (b) KNN-based partial-electrode samples. In each figure, the dash line in each figure represents that the simulated field direction is same to the experiment inferred field direction. The closer to the dash line, the better the correlation is. As seen from Figure 4-11(a) and (b), both Nb-PZT-based and KNN-based materials present reasonable correlations as the datapoints distributed around the dash line. To summarize, for either a Nb-PZT-based or a KNN-based partial-electrode sample, the simulated electric field directions from FEA correlate well with the field directions inferred from the *in situ* high-energy XRD experiments. Specifically, for Nb-PZT-based partial-electrode samples, the simulated electric field amplitudes can well-predict the extent of domain switching.

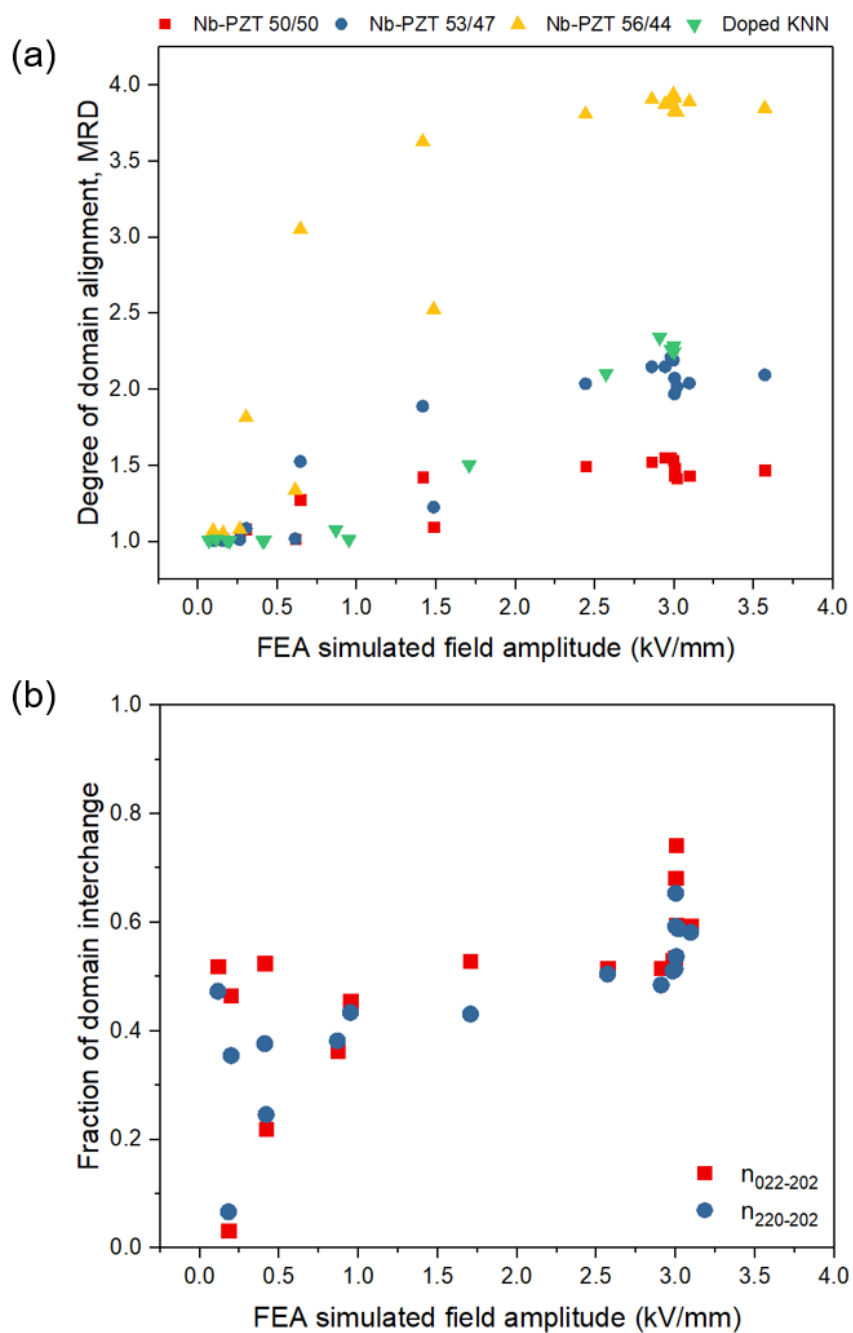


Figure 4-10 Correlations between the simulated electric field amplitudes from FEA and (a) degree of domain alignment in tetragonal and rhombohedral phase materials, and (b) fraction of domain interchange in orthorhombic phase material. (Note: Pixels with high simulated electric field values are not used in correlations)

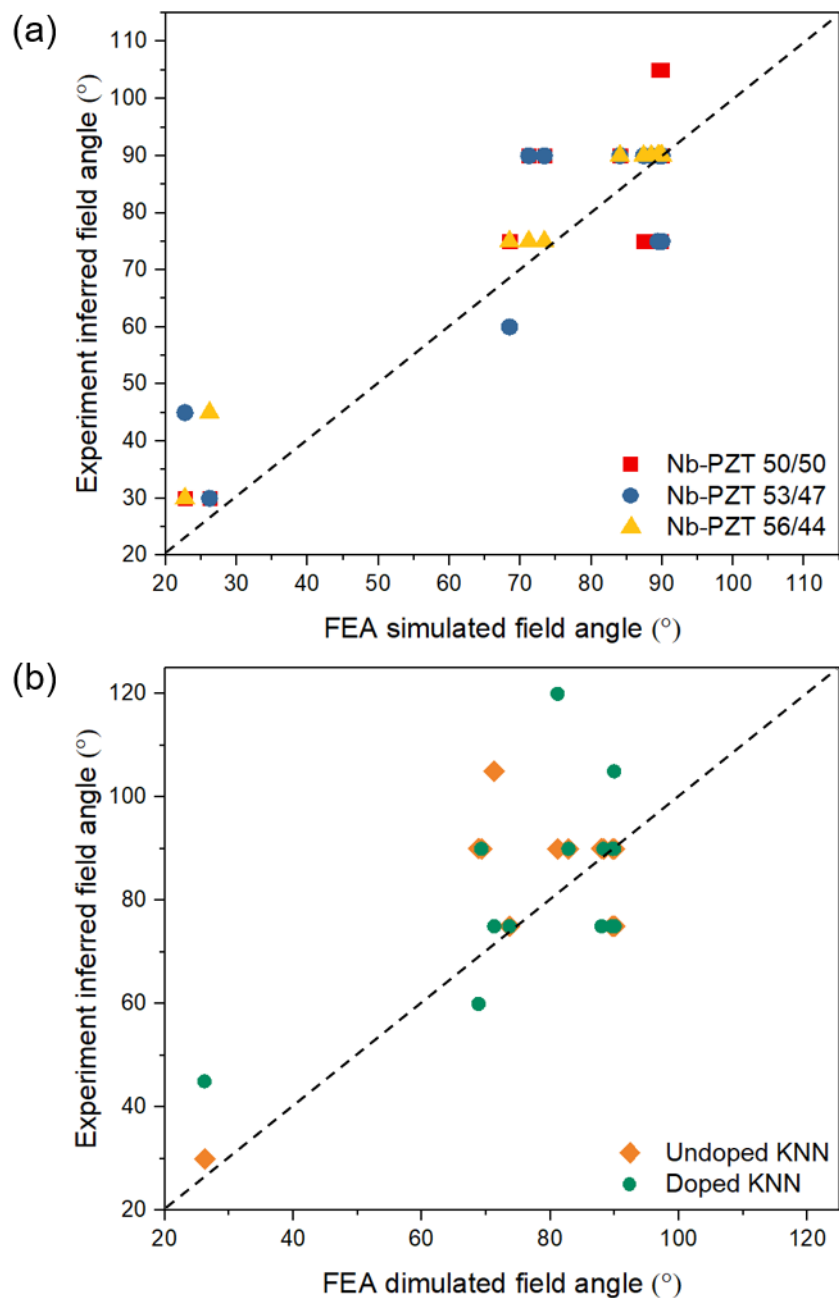


Figure 4-11 Correlations between the experimentally inferred electric field directions and simulated electric field directions from FEA in (a) Nb-PZT-based, and (b) KNN-based partial-electrode samples. (Note: Pixels exhibiting extremely low domain reorientation are not used in correlations)

4.3. Electrode Edge Scan

As shown from the FEA results in Figure 4-9 on partial-electrode samples either using lead-based or lead-free materials, there are significant electric field concentrations around the top electrode edge, which are expected to influence the field-induced ferroelectric/ferroelastic domain switching and phase transitions. For the *in situ* high-energy XRD experiment at beamline 11-ID-C, an additional scan pattern referred to as “electrode edge scan” was utilized on both lead-based and lead-free partial-electrode samples in this research. The experiment utilized a 200 μm x 200 μm monochromatic high-energy X-ray beam to sequentially scan the electrode termination region in a partial-electrode sample under the application of various electric fields. Peak pitting analysis was performed on the obtained data from each scanned pixel to probe the most preferred domain texture orientation.

As elaborated upon the partial-electrode samples using the whole bar scan pattern, the local electric field direction in each scanned pixel can be determined by computing the maximum 002 or 111 domain texture strength for a tetragonal or a rhombohedral phase ferroelectric material, respectively; in parallel, as for an orthorhombic phase partial-electrode sample, the local electric field direction in a scanned pixel can be inferred by calculating the highest fraction of domain interchange, e.g., either $n_{022-202}$ or $n_{220-202}$. To better demonstrate the experimental results, the pixels in the “electrode edge scan” pattern are labeled as shown in Figure 4-12. Take P_{4-5} for example, “P” is short for pixel, the subscription “4-5” represents the pixel position in the “4th row and 5th column”.

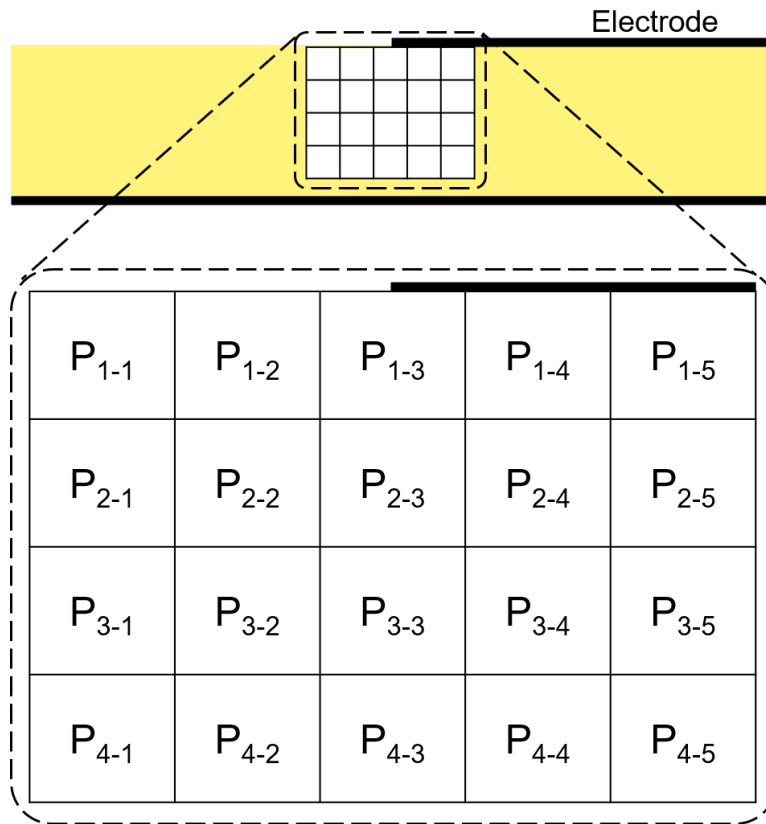


Figure 4-12 The electrode edge scan pattern used in ferroelectric partial-electrode samples with labeled pixels.

4.3.1. Nb-PZT-based Materials

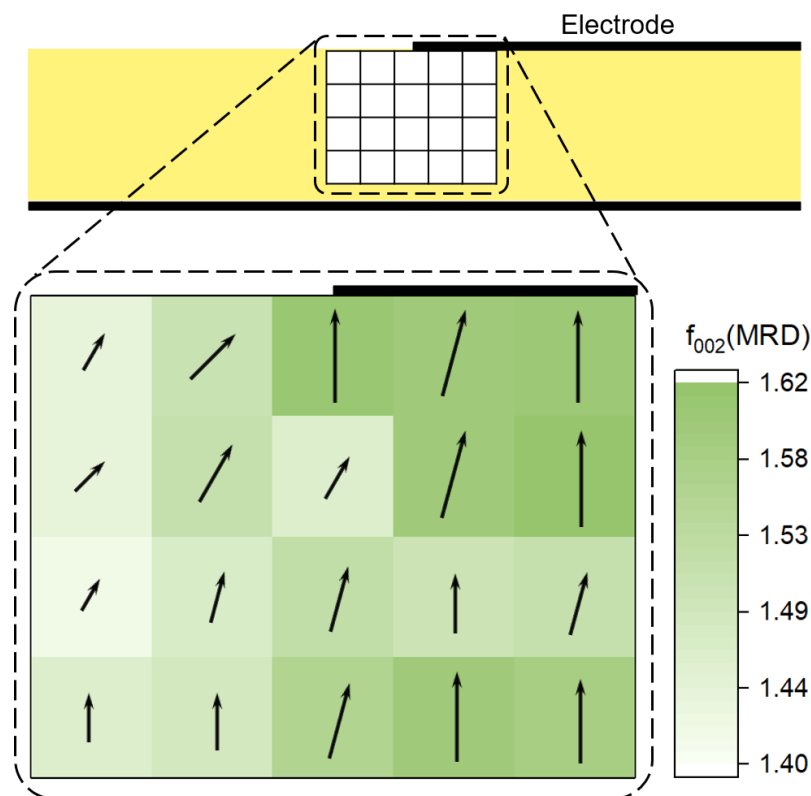


Figure 4-13 Under the application of 3 kV/mm, the calculated maximum degree of 002 domain alignment in the electrode termination region of the tetragonal phase Nb-PZT 50/50 partial-electrode sample.

Figure 4-13 presents the computed most preferred 002 domain texture strength for each scanned pixel in the Nb-PZT 50/50 partial electrode sample using the electrode edge scan pattern under the application of 3 kV/mm. As elucidated in previous section, the color in each pixel represents the calculated maximum degree of 002 domain alignment, whereas the arrow stands for the inferred local field direction with its length linearly links with values shown in the legend. The figure reveals that there exists field intensification near the electrode edge since the calculated 002 domain texture strength is higher, as illustrated in a darker color. Outside the fully electroded area,

it shows apparent orientation-dependent domain switching behaviors because of the differed arrow orientations and obvious color changes.

Similar observations are found in the rhombohedral phase Nb-PZT 56/44 partial-electrode sample, as shown Figure 4-14, which presents the intensified 111 domain texture near the electrode edge and spatially dependent and orientation-dependent domain switching phenomena in the electrode termination region.

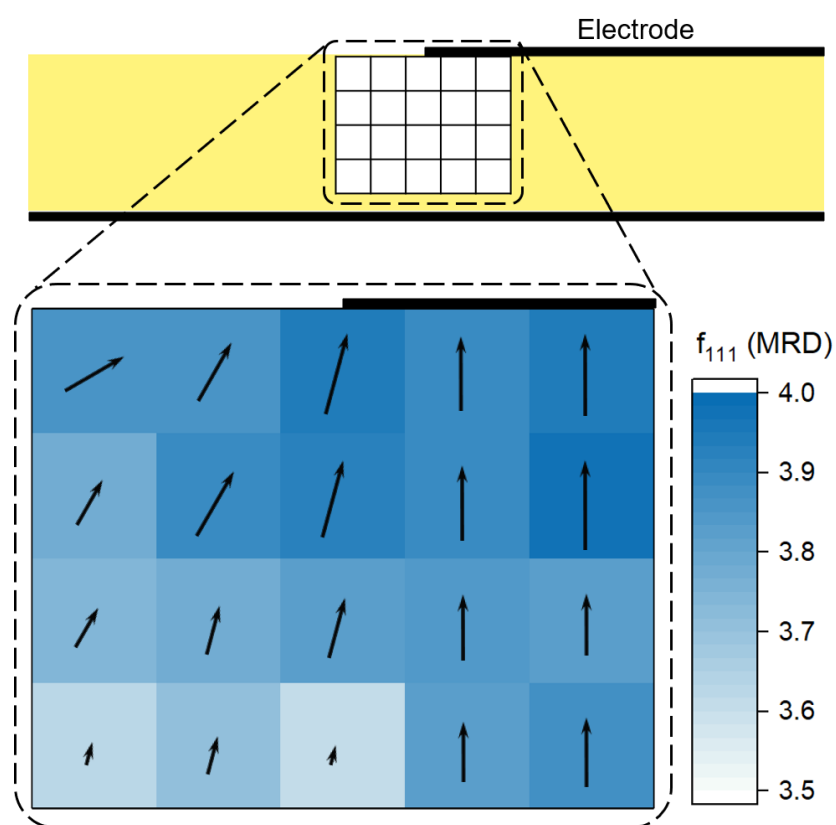


Figure 4-14 Under the application of 3 kV/mm, the calculated maximum degree of 111 domain alignment in the electrode termination region of the rhombohedral phase Nb-PZT 56/44 partial-electrode sample.

It is concluded in Chapter 3 that the Nb-PZT 53/47 exhibits orientation-dependent phase transitions from tetragonal to rhombohedral around 45° and 135° azimuthal angles under the application of homogeneous electric fields in a fully electroded sample. Specifically, this phase

transition behavior is field amplitude-dependent. Since the FEA results predict that field concentrations exist near the electrode edge, a hypothesis can be made that the orientation-dependent phase transition would be amplified in the electrode termination region of a Nb-PZT 53/47 partial-electrode sample.

Figure 4-15 shows a comparison of peak intensity changes of two representative pixels, P_{4-5} and P_{1-4} , from the electrode termination region in the Nb-PZT 53/47 partial-electrode sample. As shown from Figure 4-15(a) and (b), both pixels show well-separated 001_T and 100_T reflections without orientation-dependence in the virgin state. The reason to use 001_T and 100_T reflections here is because a little scattering from silver electrode is shown on the XRD plots which exhibits a 111_{Ag} peak falling between the 002_T and 200_T reflections. When the macroscopic electric field is elevated to 3 kV/mm, as shown in Figure 4-15(c) and (d), domain switching and orientation-selective phase transitions occur by observing the peak intensity interchange and appearance of 100_R between the 001_T and 100_T reflections. More specifically, the intensity of 100_R reflection is much more intense in Figure 4-15(d), suggesting the tetragonal-to-rhombohedral phase transition in P_{1-4} is intensified. This is more evidenced by comparing the evolution of 100_R reflection in P_{4-5} and P_{1-4} along the 45° azimuthal angle as function of electric field amplitude, as shown in Figure 4-15(e) and (f). Under the application of 3 kV/mm, the 100_R reflection in the 45° azimuthal angle is stronger in P_{1-4} than in P_{4-5} , meaning that the local electric field amplitude in P_{1-4} is higher.

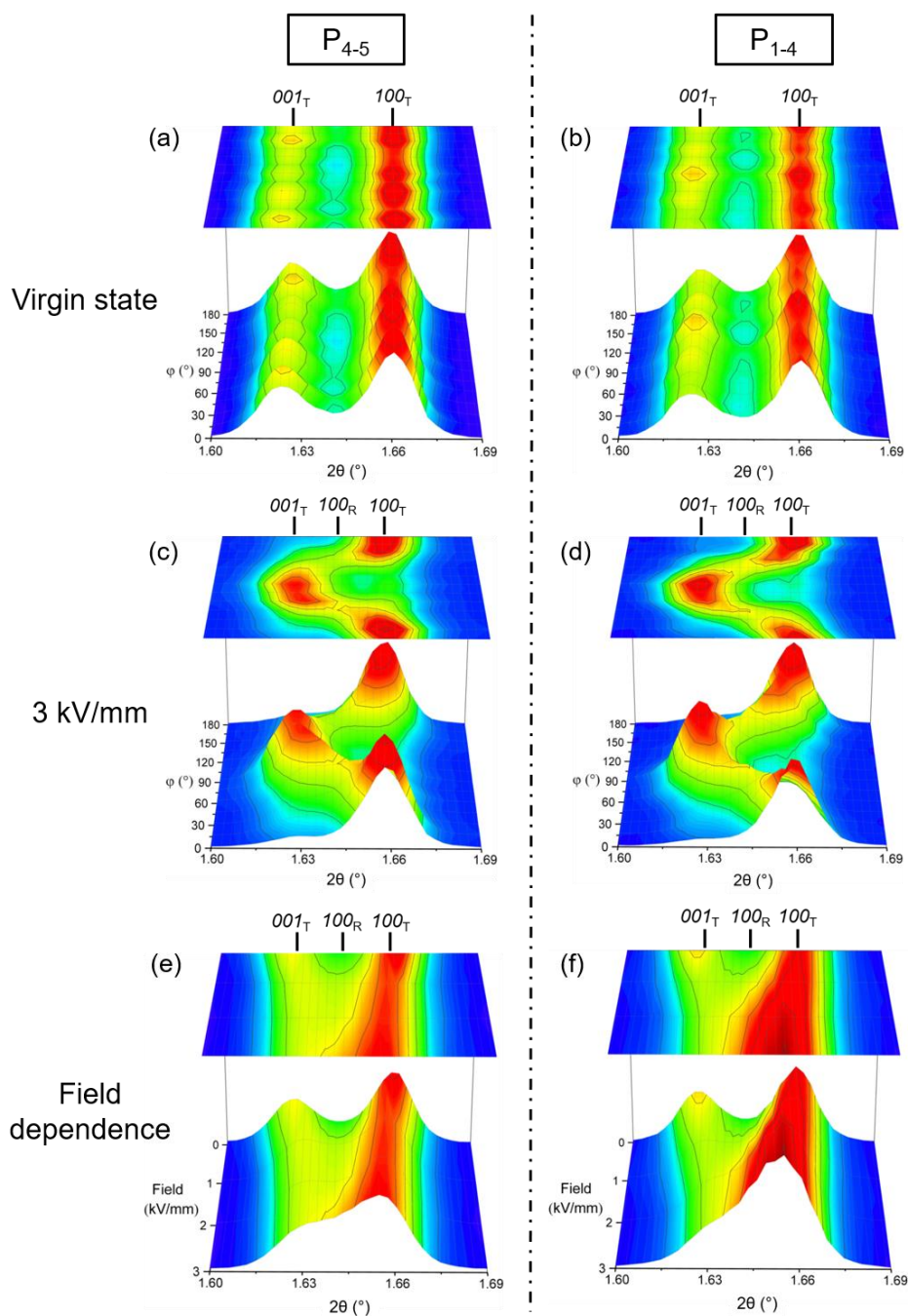


Figure 4-15 Peak intensities as a function of azimuthal angle (ϕ) for representative pixels P_{4-5} and P_{1-4} in the Nb-PZT 53/47 partial-electrode sample with the electrode edge scan pattern. Plots (a) and (b) show the peak intensities in the virgin state, (c) and (d) show the interchanged intensities at a macroscopic electric field of 3 kV/mm, (e) and (f) show the field-dependent intensity interchanges along the 45° azimuthal angle, for P_{4-5} and P_{1-4} , respectively.

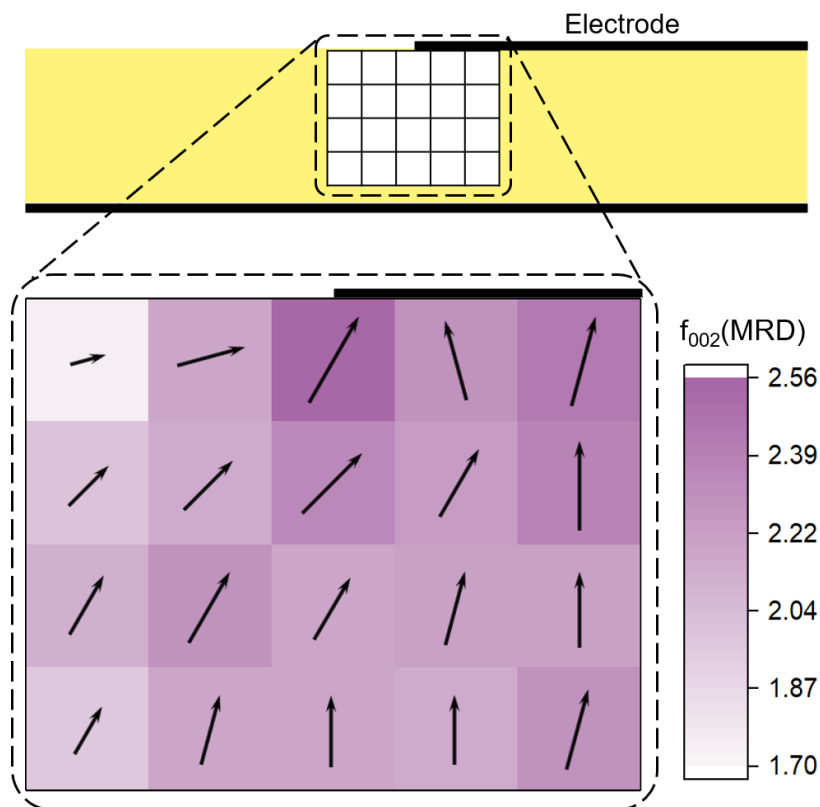


Figure 4-16 Under the application of 3 kV/mm, the calculated maximum degree of 002 domain alignment in the electrode termination region of the tetragonal phase Nb-PZT 53/47 partial-electrode sample.

Figure 4-16 presents the calculated strongest 002 domain texture strength in each scanned pixel from the electrode termination region in the Nb-PZT 53/47 partial-electrode sample. The maximum degree of 002 domain alignment is about 2.55 MRD in the electrode edge scan experiment, which is higher than the maximum value of 2.21 MRD from the partial-electrode sample experiment using the whole bar scan pattern. This evidences that, in the electrode edge scan experiment with a higher spatial resolution (smaller pixel size), the electric field is more concentrated as approaching the electrode edge. This is due to the huge electric field amplitude gradient around the electrode edge, which results in a less averaged field amplitude in a small pixel than in a large pixel. Moreover, similar observations of orientation-dependent and spatially

dependent and domain reorientation in the electrode termination region are found in the Nb-PZT 53/47 partial electrode sample as seen in the other two Nb-PZT-based samples using the same sample configuration.

4.3.2. KNN-based Materials

There are two KNN-based materials, namely pseudo-monoclinic (orthorhombic) phase undoped KNN and tetragonal phase doped KNN, investigated using the partial-electrode sample configuration with the electrode edge scan pattern. The results in this section will be initially elaborated upon the undoped KNN partial-electrode sample (Figure 4-17) and then focus on discussions of the doped KNN material (Figure 4-18).

As demonstrated in the previous section, the local electric field directions in a pseudo-monoclinic (orthorhombic) phase undoped KNN partial-electrode sample can be inferred by calculating the maximum fraction of domain interchange. Since the 202 domains are most preferred in the undoped KNN with applied electric fields, both $n_{022-202}$ (fraction change from 022 to 202 domains) and $n_{220-202}$ (fraction change from 220 to 202 domains) are computed for each scanned pixel from the electrode termination region in the undoped KNN partial-electrode sample. Figure 4-17 shows the comparison of using the calculated maximum $n_{022-202}$ and $n_{220-202}$ with inferred local electric field direction in each scanned pixel. Figure 4-17(a) and (b) both show similar spatially dependent and orientation-dependent domain switching phenomena. Except for pixels near the electrode edge having weaker 202 domain texture strength and differed local field direction, the other pixels generally exhibit similar 202 domain texture strength and local field orientations that are approximately parallel to the macroscopic field direction. This suggests that in a pseudo-monoclinic (orthorhombic) phase partial-electrode sample, the local electric fields in the electrode termination region are less heterogeneous.

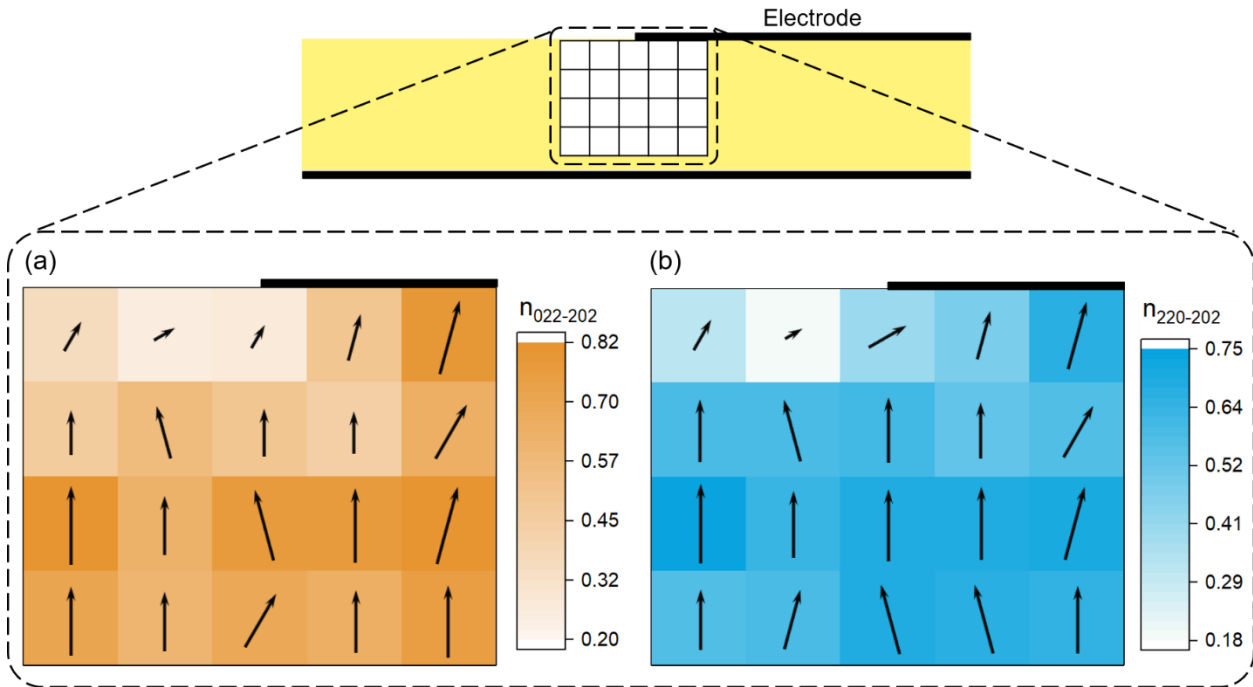


Figure 4-17 Under the application of 3 kV/mm, the calculated maximum fraction of domain interchange (a) $n_{022-202}$, and (b) $n_{220-202}$, in the electrode termination region of the pseudo-monoclinic (orthorhombic) phase, undoped KNN partial-electrode sample.

As for the tetragonal phase doped KNN partial-electrode sample, Figure 4-18 presents the calculated maximum degree of 002 domain alignment in each scanned pixel from the electrode termination region with an applied macroscopic field of 3 kV/mm. Like what is observed in other tetragonal phase materials, the domain reorientation behaviors in the electrode termination region in the doped KNN partial-electrode sample exhibit apparent orientation-dependence and position-dependence. Specifically, the strengthened 002 domain texture strength indicates the local field concentrations near the electrode edge.

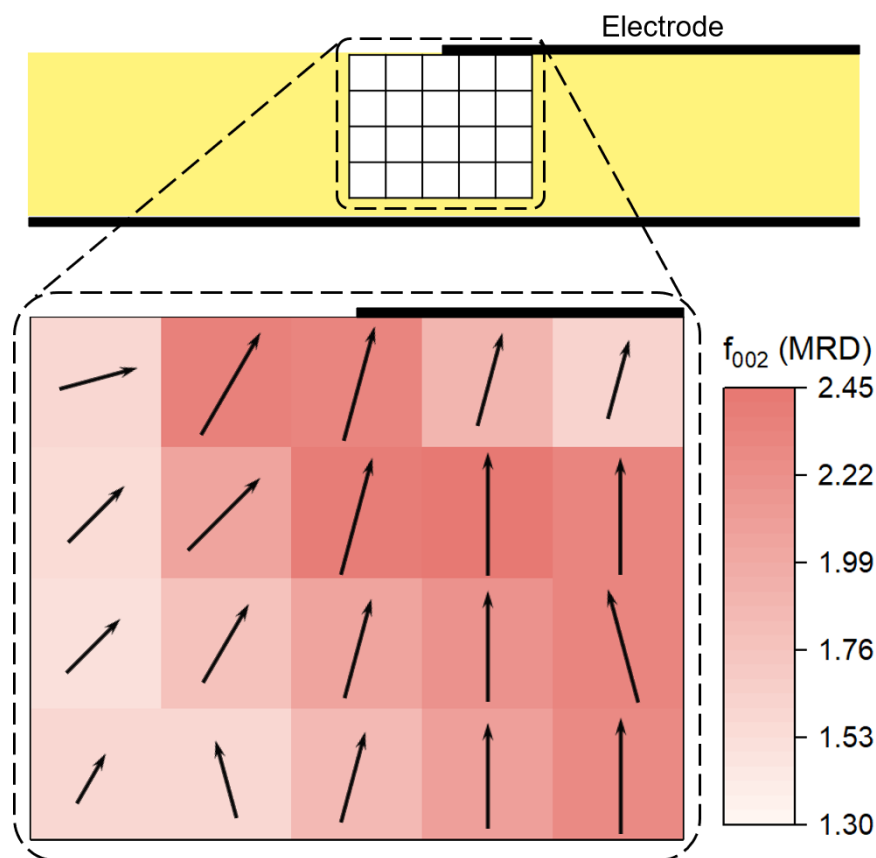


Figure 4-18 Under the application of 3 kV/mm, the degree of 002 domain alignment in the electrode termination region of the tetragonal phase, doped KNN partial-electrode sample.

4.3.3. Discussion

FEA of simulated electric fields in the 2D lead-based and lead-free partial-electrode samples predicts orientation-dependent and position-sensitive domain switching behaviors. The simulated high electric field concentration is expected to amplify the microstructural changes, including domain reorientation and phase transitions, near the electrode edge in the partial-electrode samples. This hypothesis motivates the experiments on partial-electrode samples using the electrode edge scan pattern in a higher spatial resolution (smaller pixel). The results from the Nb-PZT-based partial-electrode samples present strong orientation-dependence and position-dependence of local electric field in each probed pixel. Specifically, the Nb-PZT 53/47

partial-electrode sample shows amplified phase transitions in selective angular directions which underlines the fact of field concentration near the electrode edge. Similar domain switching behaviors are also observed in the tetragonal phase doped KNN partial-electrode sample in its electrode termination region. However, for the pseudo-monoclinic (orthorhombic) phase undoped KNN partial-electrode sample, the domain reorientation phenomena are less heterogeneous in the majority scanned pixels except for the first row near the top electrode.

Instead of using a $500\ \mu\text{m} \times 500\ \mu\text{m}$ (or $500\ \mu\text{m} \times 450\ \mu\text{m}$) X-ray beam in the “whole bar scan” experiments, the electrode edge scan experiments utilized a smaller beam size, $200\ \mu\text{m} \times 200\ \mu\text{m}$, to scan the electrode termination regions in various partial-electrode samples. Comparing to a large pixel near the electrode edge, a small pixel is expected to have a less averaged local electric field amplitude. It is known that the local field amplitude in each pixel will become higher as the pixel position approaching towards the electrode edge. Specifically, the local field amplitude should have a higher maximum value in smaller pixels than in larger pixels. This explains why a higher domain texture strength is observed in the electrode edge scan experiments.

Table 4 summarizes the calculated maximum domain texture strength and maximum fraction of domain interchange in different experiments with applied macroscopic electric field of 3 kV/mm. As seen from the table, the full-electrode samples have the lowest domain texture strength no matter which material or crystallographic phase it is. This is because the full-electrode samples were not fully poled since the total experimental time is less than 10 minutes for each composition, resulting in weaker domain textures. However, for partial-electrode samples with the whole bar scan pattern, the total experimental time is more than 2.5 hours for each composition, which means the samples are fully polarized and exhibit stronger domain textures. Moreover, the partial-electrode samples with the electrode edge scan patterns show the highest domain texture

strength (similar experimental time to whole-bar scan tests), which is resulted from the field concentration near the electrode edge.

Table 4 Under the macroscopic electric field of 3 kV/mm, the calculated maximum domain texture strength (in tetragonal, rhombohedral) and maximum fraction of domain interchange (in orthorhombic) in different sample geometries.

Material	Phase	Domain reorientation	Full-electrode sample	Whole-bar scan	Electrode-edge scan
Nb-PZT 50/50	Tetragonal	Max f_{002}	1.21	1.55	1.61
Nb-PZT 53/47	Tetragonal, near MPB	Max f_{002}	1.84	2.21	2.55
Nb-PZT 56/44	Rhombohedral	Max f_{111}	3.77	3.94	3.97
Undoped KNN	Orthorhombic (pseudo-Monoclinic)	Max $n_{022-202}$	0.26	0.74	0.82
		Max $n_{220-202}$	0.25	0.65	0.75
Doped KNN	Tetragonal	Max f_{002}	1.54	2.34	2.40

The concluding results from the partial-electrode samples in this work provide some new insight that can be used to reassess or complement some early research work. For example, Chang *et al.* simulates the electric field magnitude distribution near electrode edges on a PMN-PT single crystal, showing high field concentration around the electrode edges that is referred to as “fringe effect” [64]. This “fringe effect” facilitates new nucleation of small domains and increases the domain density near the electrode edges, which is considered to have contributions to the enhanced d_{33} value. To complement the findings by Chang *et al.*, the experimentally inferred electric field orientations from a partial-electrode sample in the present work suggest that the newly formed small domains are supposed to have polarization directions towards the electrode edges. Specifically, the strong electric field gradient around the electrode edges on the PMN-PT single crystal would also generate a strain gradient, resulting in significant spatially dependent ceramic

deformation that facilitates the microcrack generation near the electrode edges to cause device failure. As Chang *et al.* implies that the newly formed small domains have contributions to the high piezoelectric response in a PMN-PT single crystal, it worth noting that the field concentration-induced lattice distortion, which is considered as intrinsic contribution to macroscopic piezoelectric strain, may also give credits for the enhanced d_{33} . Specifically, a hypothesis can be made for a polycrystalline ferroelectric ceramic with a near MPB composition, the macroscopic strain measured at an electrode edge could be much higher than other places (e.g., beneath the electrode, or in the passive region) because, theoretically, intrinsic contribution of field-induced lattice distortion, extrinsic contribution of domain wall motion, and volumetric strain induced by phase transition, will be all influenced by the field concentration near the electrode edge.

In the PZT-based thin film capacitor, Do *et al.* observes an increased 002_T reflection density near the electrode rim but no change in the region without covered electrode, suggesting an excessive non- 180° ferroelectric/ferroelastic domain switching near the electrode rim [89]. However, based on the position-sensitive and orientation-dependent domain reorientation observed from partial-electrode samples, one can conclude that the non- 180° domain reorientation also near the electrode rim in the capacitor is spatially dependent. Even in the passive region without covered electrode, there should exist 002 domains with the strongest texture orientation tilts toward the electrode rim. Specifically, the closer to the electrode rim, the more domain reorientation can occur.

Esteves *et al.* investigated the microstructural changes in a MPB composition PZT-based MLCA by employing a $500\ \mu\text{m} \times 500\ \mu\text{m}$ X-ray beam to scan the center of the sample (the active region in the MLCA) in response to electrical and mechanical loading [74]. Parallel to the

macroscopic field direction, Esteves *et al.* shows quantitatively calculated phase fraction changes between tetragonal ($P4mm$) and rhombohedral ($R3m$) with respect to various macroscopic electric field amplitudes and different pre-stresses. For example, at pre-stress of 2 MPa (same loading direction to macroscopic electric field), the rhombohedral phase fraction increases from 25% in the unpoled state to 60% at 3 kV/mm. Undoubtedly, domain reorientation is also observed with respect to the external stimuli. However, these are observations in the active region inside a MLCA, where is expected to have homogeneous electric fields between the interdigitated electrodes. If the high-energy X-ray beam were used to scan the interdigitated electrode termination region or the passive region, the field-/stress-affected phase fractions and domain orientation preference would be different because of the local field/stress inhomogeneities.

In general, this work proves that the electric field inhomogeneity exists in a partial-electrode sample, not only concluded from the high-energy XRD experiments, but also summarized from the simulated field distribution in FEA studies. Specifically, the *in situ* high-energy XRD provides a novel characterization approach to spatially probe a ferroelectric material/device in response to an electric load. The employment of an area detector also allows the full-orientation investigation on microstructural changes with respect to various azimuthal angles.

4.4. Summary

To summarize, this chapter elaborates upon results from the *in situ* high-energy XRD experiments on various partial-electrode samples which are examined using a whole bar scan pattern and an electrode edge scan pattern. Under the application of a macroscopic electric field of 3 kV/mm, the domain reorientation in a partial-electrode sample presents strong orientation-dependence and position-dependence, which is evidenced by calculated domain texture strength and inferred local electric field directions in scanned pixels. Specifically, near the

electrode edge of most tested partial-electrode samples, the field-induced domain texture strength is amplified because of the field concentration. More specifically, for the Nb-PZT 53/47 partial-electrode sample, the tetragonal-to-rhombohedral phase transitions along selective azimuthal angles are observed to be amplified due to the local field concentration near the electrode edge. Finite element analysis performed in ANSYS predicts the averaged electric field amplitude and direction in each scanned pixel in the partial electrode sample, which shows a good correlation with the experiment inferred field direction.

Chapter 5: Conclusions and Future Work

5.1. Conclusions

This research utilizes synchrotron-based high-energy XRD to investigate the microstructural changes in ferroelectric materials in response to homogeneous or inhomogeneous electric fields. Both Nb-PZT-based and KNN-based materials are studied by measuring various kinds of samples and X-ray scan patterns. The results demonstrated in this research provide fundamental knowledge of domain reorientation and phase transitions induced by field inhomogeneities in ferroelectric devices. The illustrated experimental setup of *in situ* high-energy XRD and the elucidated data analysis methods in this research present a novel characterization strategy for probing spatially dependent and orientation-dependent material behaviors.

Chapter 3 demonstrates the *in situ* high-energy XRD results on different ferroelectric full-electrode samples which are expected to undergo homogeneous electric fields. For tetragonal and rhombohedral phase materials, the preferred domain orientation is quantitatively determined by calculating the 002 and 111 domain texture strength, respectively. In parallel, for an orthorhombic phase material, the fraction of domain interchange is studied with respect to a pseudo-monoclinic cell frame. The results show that, parallel along the macroscopic electric field direction, the 002, 111, and 202 domains are most preferred in tetragonal, rhombohedral, and orthorhombic phase, respectively. Moreover, by investigating Nb-PZT 53/47 which is close to MPB, not only is domain reorientation, but also an orientation-dependent phase transition from tetragonal to rhombohedral are observed.

In Chapter 4, the spatially dependent microstructural changes are discussed in the partial-electrode samples in response to electric field inhomogeneities. Due to the electrode discontinuity, there exist huge electric field concentrations near the electrode edge. Since domain

textures are sensitive to field directions, the local electric field directions in scanned pixels can be quantitatively inferred from the measurements. In the experiments of using partial-electrode sample with the whole bar scan pattern, the results generally show a more homogeneous domain texture in the active region between electrodes. However, the field-induced domain textures are strongly orientation-dependent and position-sensitive in the scanned pixels in the passive region, reflecting the inhomogeneous local electric fields, i.e., non-uniform field directions and amplitudes. For the experiments on partial-electrode samples via scanning the electrode termination region, it generally shows the field concentration amplified domain texture strength in different compositions. Specifically, for the Nb-PZT 53/47 (near MPB) partial-electrode sample, the field-induced orientation-dependent phase transitions are amplified.

Besides the synchrotron-based XRD experiments, FEA was also conducted in this research to simulate field, strain, and stress inhomogeneities in MLCAs and partial-electrode samples. The simulation in a KNN-based MLCA provides a motivation to study electromechanical behaviors in response to the field inhomogeneity, whereas the simulated electric fields in partial-electrode samples provide a theoretical model to compare with the experimental data. Although the FEA is simplified that misses many electromechanical effects in reality, the model is good at predicting electric field directions and relative amplitudes of domain texture strength in the partial-electrode samples. More importantly, the experimentally inferred local electric field directions are well-correlated with the simulated electric field vectors in pixels throughout the whole bar. Therefore, FEA in ANSYS with the MEMS extension offers a method to reassess or complement the conclusions from previous work. For example, simulating field directions and amplitudes around an electrode edge to deepen the understanding of “fringe effect” [64], or modeling

concentrated fields near an interdigitated electrode in a MLCA to further investigate the field-amplified phase fraction change and domain switching [74].

To summarize, the research in this dissertation utilizes the synchrotron-based high-energy XRD with an area detector to characterize homogeneous and inhomogeneous electric field-induced domain reorientation and phase transitions in various ferroelectric materials. The revealed fundamental knowledge from partial-electrode samples helps understand some aspects of the orientation-dependent and spatially dependent microstructural changes in a multilayered ferroelectric device. Specifically, for a ferroelectric MLCA, the microstructural changes in response to the macroscopic electric field are expected to be significantly different in the active region, in the passive region, and around the interdigitated electrode edges. More specifically, the excessive domain switching and field concentration-amplified phase transitions near the interdigitated electrode edges should be drawn great attention in MLCAs or thin film multilayered ceramic capacitors (MLCCs).

5.2. Suggestions for Future Work

The research in this dissertation elaborates upon inhomogeneous electric field-induced microstructural changes in lead-based Nb-PZT and lead-free KNN materials. It would be beneficial to perform similar experiments on other material systems, such as $[x\text{Ba}(\text{Zr},\text{Ti})\text{O}_3-(1-x)(\text{Ba},\text{Ca})\text{TiO}_3]$ (BZT-BCT) [37]–[40], and $[x\text{Na}_{0.5}\text{Bi}_{0.5}\text{TiO}_3-(1-x)\text{BaTiO}_3]$ (NBT-BT) [41]–[44], which helps enrich the fundamental knowledge on field inhomogeneity influenced material behaviors in ferroelectrics. Specifically, since lead-based materials are gradually restricted in electronic applications because of the toxicity, more efforts should be spent on investigating lead-free materials in order to seek excellent alternatives for next-generation ferroelectric devices.

Ferroelectric applications often operate in a wide temperature range, which is supposed to have impacts on microstructural changes in the materials. For lead-based materials, such as Nb-PZT, it would be interesting to systematically study the position-sensitive and temperature-dependent domain reorientation and phase fraction changes in the partial-electrode samples in response to different loads. Moreover, as for lead-free KNN-based materials, many research have been carried out in past decades to form rhombohedral-tetragonal (R-T) phase boundary, or to shift rhombohedral-orthorhombic (R-O) and orthorhombic-tetragonal (O-T) phase boundaries near room temperature for superior piezoelectric response [119]–[122]. Specifically, these phase boundaries in KNN-based materials are considered as characteristics of polymorphic phase transitions (PPT), which are both composition and temperature-dependent. Therefore, the study of temperature-dependence on KNN-based partial-electrode samples under field application is also a challenge and an opportunity to develop in-depth understanding material behaviors.

Not only can electric fields, but also stress loads can induce domain switching and phase fraction changes in ferroelectric ceramics. Both and Kauffmann *et al.* and Esteves *et al.* reported the compressive pre-stress enhanced non-180° domain switching in PZT-based ferroelectric ceramics [67], [74]. In the *in situ* high-energy XRD in beamline 11-ID-C, it would be fascinating to install a customized sample stage to allow probing domain reorientation and phase fraction changes in ferroelectric partial-electrode samples in response to a combination of electric field and mechanical load. The obtained results would deepen the knowledge of spatially dependent microstructural changes with respect to inhomogeneities of electric field and mechanical stress.

REFERENCES

- [1] W. D. Callister and D. G. Rethwisch, *Materials science and engineering: an introduction*, vol. Vol. 9. New York: Wiley, 2018.
- [2] C. B. Carter and M. G. Norton, *Ceramic materials: Science and engineering*. Springer New York, 2013.
- [3] N. Setter, “Piezoelectric materials in devices: extended reviews on current and emerging piezoelectric materials, technology, and applications,” 2002.
- [4] W. Heywang, K. Lubitz, and W. Wersing, *Piezoelectricity*, vol. 114. 2008.
- [5] P. Dineva, D. Gross, R. Müller, and T. Rangelov, “Dynamic Fracture of Piezoelectric Materials,” vol. 212, 2014.
- [6] J. Valasek, “Piezo-electric and allied phenomena in Rochelle salt,” *Phys. Rev.*, vol. 17, no. 4, pp. 475–481, 1921.
- [7] J. L. Jones, “The effect of crystal symmetry on the maximum polarization of polycrystalline ferroelectric materials,” *Mater. Sci. Eng. B Solid-State Mater. Adv. Technol.*, vol. 167, no. 1, pp. 6–11, 2010.
- [8] D. Damjanovic, “Ferroelectric, dielectric and piezoelectric properties of ferroelectric thin films and ceramics,” *Reports Prog. Phys.*, vol. 61, no. 9, pp. 1267–1324, 2002.
- [9] M. E. Lines, A. M. Glass, and G. Burns, *Principles and applications of ferroelectrics and related materials*. Physics Today, 1978.
- [10] M. Acosta *et al.*, “BaTiO₃-based piezoelectrics: Fundamentals, current status, and perspectives,” *Applied Physics Reviews*, vol. 4, no. 4. American Institute of Physics Inc., 01-Dec-2017.
- [11] D. Damjanovic, “Ferroelectric, dielectric and piezoelectric properties of ferroelectric thin

- films and ceramics,” *Reports Prog. Phys.*, vol. 61, no. 9, p. 1267, 1998.
- [12] D. Damjanovic, “Contributions to the piezoelectric effect in ferroelectric single crystals and ceramics,” *J. Am. Ceram. Soc.*, vol. 88, no. 10, pp. 2663–2676, 2005.
- [13] Q. M. Zhang, W. Y. Pan, S. J. Jang, and L. E. Cross, “Domain wall excitations and their contributions to the weak-signal response of doped lead zirconate titanate ceramics,” *J. Appl. Phys.*, vol. 64, no. 11, pp. 6445–6451, 1988.
- [14] M. J. Hoffmann, M. Hammer, A. Endriss, and D. C. Lupascu, “Correlation between microstructure, strain behavior, and acoustic emission of soft PZT ceramics,” *Acta Mater.*, vol. 49, no. 7, pp. 1301–1310, 2001.
- [15] J. E. Daniels, W. Jo, J. Rödel, and J. L. Jones, “Electric-field-induced phase transformation at a lead-free morphotropic phase boundary: Case study in a 93% (Bi_{0.5}Na_{0.5})TiO₃-7% BaTiO₃ piezoelectric ceramic,” *Appl. Phys. Lett.*, vol. 95, no. 3, pp. 93–95, 2009.
- [16] J. L. Jones, M. Hoffman, J. E. Daniels, and A. J. Studer, “Direct measurement of the domain switching contribution to the dynamic piezoelectric response in ferroelectric ceramics,” *Appl. Phys. Lett.*, vol. 89, no. 9, pp. 1–4, 2006.
- [17] A. Pramanick, D. Damjanovic, J. E. Daniels, J. C. Nino, and J. L. Jones, “Origins of electro-mechanical coupling in polycrystalline ferroelectrics during subcoercive electrical loading,” *J. Am. Ceram. Soc.*, vol. 94, no. 2, pp. 293–309, 2011.
- [18] R. Herbiet, U. Robels, H. Dederichs, and G. Arlt, “Domain Wall And Volume Contributions To Material Properties Of Pzt Ceramics,” *Ferroelectrics*, vol. 98, no. 1, pp. 107–121, 1989.
- [19] J. E. Daniels, W. Jo, J. Rödel, V. Honkimäki, and J. L. Jones, “Electric-field-induced

- phase-change behavior in $(\text{Bi}_{0.5}\text{Na}_{0.5})\text{TiO}_3\text{-BaTiO}_3\text{-}(\text{K}_{0.5}\text{Na}_{0.5})\text{NbO}_3$: A combinatorial investigation,” *Acta Mater.*, vol. 58, no. 6, pp. 2103–2111, 2010.
- [20] T. Iamsasri, G. Tutuncu, C. Uthaisar, S. Wongsanmai, S. Pojprapai, and J. L. Jones, “Electric field-induced phase transitions in Li-modified $\text{Na}_{0.5}\text{K}_{0.5}\text{NbO}_3$ at the polymorphic phase boundary,” vol. 024101, no. 2015, pp. 0–7, 2016.
- [21] A. P. Jephcoat, S. J. Milne, T. P. Comyn, A. K. Kleppe, A. J. Royles, and A. J. Bell, “Electric-field-induced phase switching in the lead free piezoelectric potassium sodium bismuth titanate,” *Appl. Phys. Lett.*, vol. 97, no. 13, p. 132909, 2010.
- [22] M. Hinterstein *et al.*, “Structural description of the macroscopic piezo- and ferroelectric properties of lead zirconate titanate,” *Phys. Rev. Lett.*, vol. 107, no. 7, pp. 10–13, 2011.
- [23] P. Muralt, “Ferroelectric thin films for micro-sensors and actuators: a review,” *J. Micromechanics Microengineering*, vol. 10, no. 2, pp. 136–146, Jun. 2000.
- [24] L. E. Cross, “Ferroelectric materials for electromechanical transducer applications,” *Mater. Chem. Phys.*, vol. 43, no. 2, pp. 108–115, 1996.
- [25] P. Muralt and A. Member, “PZT thin films for microsensors and actuators-Where do we stand.pdf,” vol. 47, no. 4, pp. 903–915, 2000.
- [26] S. Gebhardt, L. Seffner, F. Schlenkrich, and A. Schönecker, “PZT thick films for sensor and actuator applications,” *J. Eur. Ceram. Soc.*, vol. 27, no. 13–15, pp. 4177–4180, 2007.
- [27] J. F. Ihlefeld, D. T. Harris, K. Jacob, L. J. J. Maria, and S. Trolier-mckinstry, “Scaling Effects in Perovskite Ferroelectrics: Fundamental Limits and Process-Structure-Property Relations,” vol. 2557, pp. 6–9, 2016.
- [28] X. Du, J. Zheng, U. Belegundu, and K. Uchino, “Crystal orientation dependence of piezoelectric properties of lead zirconate titanate near the morphotropic phase boundary,”

- Appl. Phys. Lett.*, vol. 72, no. 19, pp. 2421–2423, 1998.
- [29] D. V. Taylor and D. Damjanovic, “Piezoelectric properties of rhombohedral Pb(Zr,Ti)O₃ thin films with (100), (111), and ‘random’ crystallographic orientation,” *Appl. Phys. Lett.*, vol. 76, no. 12, pp. 1615–1617, 2000.
- [30] Y. Tan *et al.*, “Unfolding grain size effects in barium titanate ferroelectric ceramics,” *Sci. Rep.*, vol. 5, p. 9953, 2015.
- [31] Q. M. Zhang, H. Wang, N. Kim, and L. E. Cross, “Direct evaluation of domain-wall and intrinsic contributions to the dielectric and piezoelectric response and their temperature dependence on lead zirconate-titanate ceramics,” *J. Appl. Phys.*, vol. 75, no. 1, pp. 454–459, 1994.
- [32] H. JAFFE, “Piezoelectric Ceramics,” *J. Am. Ceram. Soc.*, vol. 41, no. 11, pp. 494–498, 1958.
- [33] C. C. Chung, C. M. Fancher, C. Isaac, J. Nikkel, E. Hennig, and J. L. Jones, “Temperature dependence of field-responsive mechanisms in lead zirconate titanate,” *J. Am. Ceram. Soc.*, vol. 100, no. 9, pp. 4352–4361, 2017.
- [34] V. Kovacova, N. Vaxelaire, G. Le Rhun, P. Gergaud, T. Schmitz-Kempen, and E. Defay, “Correlation between electric-field-induced phase transition and piezoelectricity in lead zirconate titanate films.”
- [35] D. J. Franzbach *et al.*, “Electric-field-induced phase transitions in co-doped Pb(Zr_{1-x}Ti_x)O₃ at the morphotropic phase boundary,” <http://www.tandfonline.com/action/journalInformation?show=aimsScope&journalCode=sta20#.VmBmuzZFCUk>, 2014.
- [36] “Directive 2012/19/EU of the European Parliament and of the Council of 4 July 2012 on

- Waste Electrical and Electronic Equipment,” 2012. .
- [37] J. P. Praveen, T. Karthik, A. R. James, E. Chandrakala, S. Asthana, and D. Das, “Effect of poling process on piezoelectric properties of sol-gel derived BZT-BCT ceramics,” *J. Eur. Ceram. Soc.*, vol. 35, no. 6, pp. 1785–1798, Jun. 2015.
- [38] J. P. Praveen, K. Kumar, A. R. James, T. Karthik, S. Asthana, and D. Das, “Large piezoelectric strain observed in sol-gel derived BZT-BCT ceramics,” *Curr. Appl. Phys.*, vol. 14, no. 3, pp. 396–402, Mar. 2014.
- [39] M. C. Ehmke, J. E. Blendell, and K. J. Bowman, “Electric field effects on piezoelectric and ferroelastic strain in $\text{Ba}(\text{Zr}_{0.2}\text{Ti}_{0.8})\text{O}_3-x(\text{Ba}_{0.7}\text{Ca}_{0.3})\text{TiO}_3$ piezoceramics,” *2013 Jt. IEEE Int. Symp. Appl. Ferroelectr. Work. Piezoresponse Force Microsc.*, pp. 84–86, 2014.
- [40] V. Sreenivas *et al.*, “Structure, dielectric, ferroelectric, and energy density properties of $(1-x)\text{BZT}-x\text{BCT}$ ceramic capacitors for energy storage applications.”
- [41] Q. Zhang, X. Zhao, R. Sun, and H. Luo, “Crystal growth and electric properties of lead-free NBT-BT at compositions near the morphotropic phase boundary,” *Phys. status solidi*, vol. 208, no. 5, pp. 1012–1020, May 2011.
- [42] S. Shanmuga Sundari, B. Kumar, and R. Dhanasekaran, “Synthesis, dielectric and relaxation behavior of lead free NBT-BT ceramics,” *Ceram. Int.*, vol. 39, no. 1, pp. 555–561, Jan. 2013.
- [43] W. P. Cao, W. L. Li, D. Xu, Y. F. Hou, W. Wang, and W. D. Fei, “Enhanced electrocaloric effect in lead-free NBT-based ceramics,” *Ceram. Int.*, vol. 40, no. 7 PART A, pp. 9273–9278, Aug. 2014.
- [44] D. K. Khatua, T. Mehrotra, A. Mishra, B. Majumdar, A. Senyshyn, and R. Ranjan,

- “Anomalous influence of grain size on the global structure, ferroelectric and piezoelectric response of $\text{Na}_{0.5}\text{Bi}_{0.5}\text{TiO}_3$,” *Acta Mater.*, vol. 134, pp. 177–187, 2017.
- [45] X. Wang *et al.*, “Giant piezoelectricity in potassium-sodium niobate lead-free ceramics,” *J. Am. Chem. Soc.*, vol. 136, no. 7, pp. 2905–2910, Feb. 2014.
- [46] K. Xu *et al.*, “Superior Piezoelectric Properties in Potassium–Sodium Niobate Lead-Free Ceramics,” *Adv. Mater.*, pp. 8519–8523, 2016.
- [47] J. Wook *et al.*, “Giant electric-field-induced strains in lead-free ceramics for actuator applications-status and perspective.”
- [48] K. Wang and J. F. Li, “Domain engineering of lead-free Li-modified (K,Na)NbO₃ polycrystals with highly enhanced piezoelectricity,” *Adv. Funct. Mater.*, vol. 20, no. 12, pp. 1924–1929, Jun. 2010.
- [49] J. Wu, D. Xiao, Y. Wang, J. Zhu, P. Yu, and Y. Jiang, “Compositional dependence of phase structure and electrical properties in (K_{0.42} Na_{0.58}) NbO₃ -LiSbO₃ lead-free ceramics,” *J. Appl. Phys.*, vol. 102, no. 11, p. 114113, Dec. 2007.
- [50] J. Rödel, K. G. Webber, R. Dittmer, W. Jo, M. Kimura, and D. Damjanovic, “Transferring lead-free piezoelectric ceramics into application,” *J. Eur. Ceram. Soc.*, vol. 35, no. 6, pp. 1659–1681, 2015.
- [51] Y. Saito *et al.*, “Lead-free piezoceramics,” *Nature*, vol. 432, no. 7013, pp. 84–87, Nov. 2004.
- [52] B. Jaffe, W. Cook, and H. Jaffe, “Piezoelectric ceramics; Academic Press, London; New York,” 1971.
- [53] J. F. Li, K. Wang, F. Y. Zhu, L. Q. Cheng, and F. Z. Yao, “(K, Na) NbO₃-based lead-free piezoceramics: Fundamental aspects, processing technologies, and remaining challenges,”

- J. Am. Ceram. Soc.*, vol. 96, no. 12, pp. 3677–3696, 2013.
- [54] W. Liu and X. Ren, “Large piezoelectric effect in Pb-free ceramics,” *Phys. Rev. Lett.*, vol. 103, no. 25, pp. 1–4, 2009.
- [55] W. Jo *et al.*, “On the phase identity and its thermal evolution of lead free (Bi $1/2$ Na $1/2$)TiO 3 -6 mol BaTiO 3 ,” *J. Appl. Phys.*, vol. 110, no. 7, Oct. 2011.
- [56] J. Wu, D. Xiao, and J. Zhu, “Potassium-sodium niobate lead-free piezoelectric materials: Past, present, and future of phase boundaries,” *Chem. Rev.*, vol. 115, no. 7, pp. 2559–2595, 2015.
- [57] A. Pramanick, A. D. Prewitt, J. S. Forrester, and J. L. Jones, “Domains, domain walls and defects in perovskite ferroelectric oxides: A review of present understanding and recent contributions,” *Crit. Rev. Solid State Mater. Sci.*, vol. 37, no. 4, pp. 243–275, 2012.
- [58] R. A. Eichel, “Characterization of defect structure in acceptor-modified piezoelectric ceramics by multifrequency and multipulse electron paramagnetic resonance spectroscopy,” *J. Am. Ceram. Soc.*, vol. 91, no. 3, pp. 691–701, 2008.
- [59] H. Guo and X. Tan, “Direct observation of the recovery of an antiferroelectric phase during polarization reversal of an induced ferroelectric phase,” *Phys. Rev. B - Condens. Matter Mater. Phys.*, vol. 91, no. 14, p. 144104, Apr. 2015.
- [60] A. Y. Emelyanov, “Coherent ferroelectric switching by atomic force microscopy,” *Phys. Rev. B - Condens. Matter Mater. Phys.*, vol. 71, no. 13, pp. 1–4, 2005.
- [61] A. Gruverman, O. Kolosov, J. Hatano, K. Takahashi, and H. Tokumoto, “Domain structure and polarization reversal in ferroelectrics studied by atomic force microscopy,” *J. Vac. Sci. Technol. B Microelectron. Nanom. Struct.*, vol. 13, no. 3, pp. 1095–1099, May 1995.

- [62] J. X. Zhang *et al.*, “Large field-induced strains in a lead-free piezoelectric material,” *Nat. Nanotechnol.*, vol. 6, p. 16, 2011.
- [63] A. Agronin *et al.*, “Dynamics of ferroelectric domain growth in the field of atomic force microscope,” *J. Appl. Phys.*, vol. 99, no. 10, p. 104102, May 2006.
- [64] W. Y. Chang *et al.*, “Patterned nano-domains in PMN-PT single crystals,” *Acta Mater.*, vol. 143, pp. 166–173, 2018.
- [65] A. Gruverman and S. V. Kalinin, “Piezoresponse force microscopy and recent advances in nanoscale studies of ferroelectrics,” *J. Mater. Sci.*, vol. 41, no. 1, pp. 107–116, 2006.
- [66] S. Jesse, H. N. Lee, and S. V. Kalinin, “Quantitative mapping of switching behavior in piezoresponse force microscopy,” *Rev. Sci. Instrum.*, vol. 77, no. 7, p. 073702, Jul. 2006.
- [67] P. Kaufmann, S. Röhrig, P. Supancic, and M. Deluca, “Influence of ferroelectric domain texture on the performance of multilayer piezoelectric actuators,” *J. Eur. Ceram. Soc.*, vol. 37, no. 5, pp. 2039–2046, 2017.
- [68] S. Pojprapai, J. L. Jones, and M. Hoffman, “Determination of domain orientation in lead zirconate titanate ceramics by Raman spectroscopy,” *Appl. Phys. Lett.*, vol. 88, no. 16, p. 162903, Apr. 2006.
- [69] Q. Zhang, J. Zhai, L. Kong, and X. Yao, “Investigation of ferroelectric phase transition for barium strontium titanate ceramics by in situ Raman scattering,” *J. Appl. Phys.*, vol. 112, no. 12, p. 124112, Dec. 2012.
- [70] I. V. Ciuchi *et al.*, “Field-induced antiferroelectric to ferroelectric transitions in $(\text{Pb}_{1-x}\text{La}_x)(\text{Zr}_{0.90}\text{Ti}_{0.10})_{1-x}/4\text{O}_3$ investigated by in situ X-ray diffraction,” *J. Eur. Ceram. Soc.*, vol. 37, no. 15, pp. 4631–4636, 2017.
- [71] I. V. Ciuchi *et al.*, “Field induced metastable ferroelectric phase in

- Pb_{0.97}La_{0.03}(Zr_{0.90}Ti_{0.10})_{0.9925}O₃ ceramics,” *J. Eur. Ceram. Soc.*, vol. 38, no. 4, pp. 1479–1487, 2018.
- [72] A. Bradeško *et al.*, “Electrocaloric fatigue of lead magnesium niobate mediated by an electric-field-induced phase transformation,” *Acta Mater.*, vol. 169, pp. 275–283, 2019.
- [73] J. L. Jones *et al.*, “Domain wall and interphase boundary motion in a two-phase morphotropic phase boundary ferroelectric: Frequency dispersion and contribution to piezoelectric and dielectric properties,” *Phys. Rev. B - Condens. Matter Mater. Phys.*, vol. 86, no. 2, pp. 1–9, 2012.
- [74] G. Esteves, C. M. Fancher, S. Röhrig, G. A. Maier, J. L. Jones, and M. Deluca, “Electric-field-induced structural changes in multilayer piezoelectric actuators during electrical and mechanical loading,” *Acta Mater.*, vol. 132, pp. 96–105, 2017.
- [75] T. Iamsasri, G. Tutuncu, C. Uthaisar, S. Wongsanmai, S. Pojprapai, and J. L. Jones, “Electric field-induced phase transitions in Li-modified KNN at the polymorphic phase boundary,” *J. Appl. Phys.*, vol. 117, no. 2, p. 024101, 2015.
- [76] J. L. Jones, E. B. Slamovich, and K. J. Bowman, “Domain texture distributions in tetragonal lead zirconate titanate by x-ray and neutron diffraction,” *J. Appl. Phys.*, vol. 97, no. 3, pp. 1–6, 2005.
- [77] J. L. Jones, E. B. Slamovich, K. J. Bowman, and D. C. Lupascu, “Domain switching anisotropy in textured bismuth titanate ceramics,” *J. Appl. Phys.*, vol. 98, no. 10, pp. 0–8, 2005.
- [78] M. Hinterstein *et al.*, “Interplay of strain mechanisms in morphotropic piezoceramics,” *Acta Mater.*, vol. 94, pp. 319–327, 2015.
- [79] H. Simons, J. E. Daniels, A. J. Studer, J. L. Jones, and M. Hoffman, “Measurement and

- analysis of field-induced crystallographic texture using curved position-sensitive diffraction detectors,” *J. Electroceramics*, vol. 32, no. 4, pp. 283–291, 2014.
- [80] J. L. Jones, B. J. Iverson, and K. J. Bowman, “Texture and anisotropy of polycrystalline piezoelectrics,” *J. Am. Ceram. Soc.*, vol. 90, no. 8, pp. 2297–2314, 2007.
- [81] Z. Wang and J. E. Daniels, “Quantitative analysis of domain textures in ferroelectric ceramics from single high-energy synchrotron X-ray diffraction images,” *J. Appl. Phys.*, vol. 121, no. 16, pp. 1–6, 2017.
- [82] E. Aksel, J. S. Forrester, B. Kowalski, J. L. Jones, and P. A. Thomas, “Phase transition sequence in sodium bismuth titanate observed using high-resolution x-ray diffraction,” *Appl. Phys. Lett.*, vol. 99, no. 22, p. 222901, Nov. 2011.
- [83] G. Esteves *et al.*, “Effect of Mechanical Constraint on Domain Reorientation in Predominantly {111}-Textured Lead Zirconate Titanate Films,” *J. Am. Ceram. Soc.*, vol. 99, no. 5, pp. 1802–1807, May 2016.
- [84] C. M. Fancher *et al.*, “The contribution of 180° domain wall motion to dielectric properties quantified from in situ X-ray diffraction,” *Acta Mater.*, vol. 126, pp. 36–43, Mar. 2017.
- [85] M. Wallace *et al.*, “In situ measurement of increased ferroelectric/ferroelastic domain wall motion in declamped tetragonal lead zirconate titanate thin films,” *J. Appl. Phys.*, vol. 117, no. 5, Feb. 2015.
- [86] C. Zhao *et al.*, “Deconvolved intrinsic and extrinsic contributions to electrostrain in high performance, Nb-doped $\text{Pb}(\text{Zr}_x\text{Ti}_{1-x})\text{O}_3$ piezoceramics ($0.50 \leq x \leq 0.56$),” *Acta Mater.*, vol. 158, pp. 369–380, 2018.
- [87] J. E. Daniels, A. Pramanick, and J. L. Jones, “Time-Resolved Characterization of

- Ferroelectrics Using High-Energy X-ray Diffraction,” *IEEE Trans. Ultrason. Ferroelectr. Freq. Control*, vol. 56, no. 8, pp. 1539–1545, 2009.
- [88] W. Y. Chang *et al.*, “Study on dielectric and piezoelectric properties of 0.7 Pb(Mg_{1/3}Nb_{2/3})O₃-0.3 PbTiO₃ single crystal with nano-patterned composite electrode,” *J. Appl. Phys.*, vol. 114, no. 11, p. 114103, Sep. 2013.
- [89] D. H. Do, P. G. Evans, E. D. Isaacs, D. M. Kim, C. B. Eom, and E. M. Dufresne, “Structural visualization of polarization fatigue in epitaxial ferroelectric oxide devices,” *Nat. Mater.*, vol. 3, no. 6, pp. 365–369, 2004.
- [90] T. Zhu, F. Fang, and W. Yang, “Fatigue crack growth in ferroelectric ceramics below the coercive field,” *J. Mater. Sci. Lett.*, vol. 18, no. 13, pp. 1025–1027, 1999.
- [91] H. Cao and A. G. Evans, “Electric Field Induced Fatigue Crack Growth in Piezoelectrics,” *J. Am. Ceram. Soc.*, vol. 77, no. 7, pp. 1783–1786, 1994.
- [92] W. Qiu, Y. L. Kang, Q. H. Qin, Q. C. Sun, and F. Y. Xu, “Study for multilayer piezoelectric composite structure as displacement actuator by Moiré interferometry and infrared thermography experiments,” *Mater. Sci. Eng. A*, vol. 452–453, pp. 228–234, 2007.
- [93] “Computergestützte Multiskalenmodellierung zur Virtuellen Entwicklung Polykristalliner Ferroelektrischer Materialien (COMFEM). Report,” 2010.
- [94] D. Viehland, “Effect of uniaxial stress upon the electromechanical properties of various piezoelectric ceramics and single crystals,” *J. Am. Ceram. Soc.*, vol. 89, no. 3, pp. 775–785, 2006.
- [95] R. Gerson, “Variation in ferroelectric characteristics of lead zirconate titanate ceramics due to minor chemical modifications,” *J. Appl. Phys.*, vol. 31, no. 1, pp. 188–194, Jan.

- 1960.
- [96] D. M. Zhu and P. D. Han, “Thermal conductivity and electromechanical property of single-crystal lead magnesium niobate titanate,” *Appl. Phys. Lett.*, vol. 75, no. 24, pp. 3868–3870, Dec. 1999.
- [97] W. Liu and X. Ren, “Large piezoelectric effect in Pb-free ceramics,” *Phys. Rev. Lett.*, vol. 103, no. 25, p. 257602, Dec. 2009.
- [98] G. Tutuncu, L. Fan, J. Chen, X. Xing, and J. L. Jones, “Extensive domain wall motion and deaging resistance in morphotropic $0.55\text{Bi}(\text{Ni}_{1/2}\text{Ti}_{1/2})\text{O}_3\text{-}0.45\text{PbTiO}_3$ polycrystalline ferroelectrics,” *Appl. Phys. Lett.*, vol. 104, no. 13, pp. 0–5, 2014.
- [99] D. A. Ochoa *et al.*, “Extensive domain wall contribution to strain in a (K,Na)NbO₃-based lead-free piezoceramics quantified from high energy X-ray diffraction,” *J. Eur. Ceram. Soc.*, vol. 36, no. 10, pp. 2489–2494, 2016.
- [100] J. E. Daniels, W. Jo, J. Roedel, and J. L. Jones, “Electric-field-induced phase transformation at a lead-free morphotropic phase boundary. Case study in a $93\%(\text{Bi}_{0.5}\text{Na}_{0.5})\text{TiO}_3\text{-}7\% \text{BaTiO}_3$ piezoelectric ceramic,” *Appl. Phys. Lett. F. Full J. Title Applied Phys. Lett.*, vol. 95, no. 3, pp. 032904/1-032904/3, 2009.
- [101] M. C. Ehmke, N. H. Khansur, J. E. Daniels, J. E. Blendell, and K. J. Bowman, “Resolving structural contributions to the electric-field-induced strain in lead-free $(1 - X)\text{Ba}(\text{Zr}_{0.2}\text{Ti}_{0.8})\text{O}_3\text{-}x(\text{Ba}_{0.7}\text{Ca}_{0.3})\text{TiO}_3$ piezoceramics,” *Acta Mater.*, vol. 66, pp. 340–348, 2014.
- [102] “Beamline 11-ID-C, APS: High-energy Diffraction.” [Online]. Available: https://www.aps.anl.gov/Beamlines/Directory/Details?beamline_id=15. [Accessed: 16-Jun-2020].

- [103] “PI H-850 6-Axis Hexapod: Specifications Motion and positioning.”
- [104] a. P. Hammersley, S. O. Svensson, M. Hanfland, a. N. Fitch, and D. Hausermann, “Two-dimensional detector software: From real detector to idealised image or two-theta scan,” *High Press. Res.*, vol. 14, no. 4–6, pp. 235–248, 1996.
- [105] B. H. Toby, “EXPGUI, a graphical user interface for GSAS,” *J. Appl. Crystallogr.*, vol. 34, no. 2, pp. 210–213, 2001.
- [106] B. H. Toby and R. B. Von Dreele, “GSAS-II: The genesis of a modern open-source all purpose crystallography software package,” *J. Appl. Crystallogr.*, vol. 46, no. 2, pp. 544–549, 2013.
- [107] L. Lutterotti, S. Matthies, and H. R. Wenk, “MAUD: a friendly Java program for Material Analysis Using Diffraction,” *International Union of Crystallography Newsletter*, no. 21, pp. 14–15, 1999.
- [108] A. A. Coelho, “TOPAS and TOPAS-Academic: An optimization program integrating computer algebra and crystallographic objects written in C++: An,” *J. Appl. Crystallogr.*, vol. 51, no. 1, pp. 210–218, 2018.
- [109] J. Rodríguez-Carvajal, “Recent advances in magnetic structure determination by neutron powder diffraction,” *Phys. B Phys. Condens. Matter*, vol. 192, no. 1–2, pp. 55–69, 1993.
- [110] G. Esteves, K. Ramos, C. Fancher, and J. Jones, “LIPRAS: Line-Profile Analysis Software.” 2017.
- [111] G. Esteves, “Synchrotron X-Ray Diffraction Studies of Domain Reorientation in Lead Zirconate Titanate,” North Carolina State University, 2017.
- [112] J. L. Jones *et al.*, “Time-resolved and orientation-dependent electric-field-induced strains in lead zirconate titanate ceramics,” *Appl. Phys. Lett.*, vol. 90, no. 17, pp. 23–25, 2007.

- [113] L. Fan, J. Chen, Y. Ren, Z. Pan, L. Zhang, and X. Xing, “Unique Piezoelectric Properties of the Monoclinic Phase in Pb (Zr,Ti) O₃ Ceramics: Large Lattice Strain and Negligible Domain Switching,” *Phys. Rev. Lett.*, vol. 116, no. 2, pp. 1–5, 2016.
- [114] H. Liu *et al.*, “Role of Reversible Phase Transformation for Strong Piezoelectric Performance at the Morphotropic Phase Boundary,” *Phys. Rev. Lett.*, vol. 120, no. 5, pp. 1–19, 2018.
- [115] T. Iamsasri, G. Tutuncu, C. Uthaisar, S. Pojprapai, and J. L. Jones, “Analysis methods for characterizing ferroelectric/ferroelastic domain reorientation in orthorhombic perovskite materials and application to Li-doped Na_{0.5}K_{0.5}NbO₃,” *J. Mater. Sci.*, vol. 48, no. 20, pp. 6905–6910, 2013.
- [116] T. Iamsasri, “Electric Field-induced Phase Transitions in Ferroelectrics at Polymorphic Phase Boundaries,” 2016.
- [117] D. Berlincourt and H. H. A. Krueger, “Technical Publication TP-226 Properties of Piezoelectricity Ceramics Visit the Morgan Electro Ceramics Web Site www.morgan-electroceramics.com PROPERTIES OF MORGAN ELECTRO CERAMIC CERAMICS.”
- [118] L. Zheng, X. Huo, R. Wang, J. Wang, W. Jiang, and W. Cao, “Large size lead-free (Na,K)(Nb,Ta)O₃ piezoelectric single crystal: Growth and full tensor properties,” *CrystEngComm*, vol. 15, no. 38, pp. 7718–7722, 2013.
- [119] R. Wang, H. Bando, T. Katsumata, Y. Inaguma, H. Taniguchi, and M. Itoh, “Tuning the orthorhombic-rhombohedral phase transition temperature in sodium potassium niobate by incorporating barium zirconate,” *Phys. status solidi - Rapid Res. Lett.*, vol. 3, no. 5, pp. 142–144, Jul. 2009.
- [120] R. Zuo, J. Fu, D. Lv, and Y. Liu, “Antimony tuned rhombohedral-orthorhombic phase

- transition and enhanced piezoelectric properties in sodium potassium niobate,” *J. Am. Ceram. Soc.*, vol. 93, no. 9, pp. 2783–2787, Sep. 2010.
- [121] Y. Wang, D. Damjanovic, N. Klein, E. Hollenstein, and N. Setter, “Compositional inhomogeneity in Li- and Ta-modified (K, Na)NbO₃ ceramics,” *J. Am. Ceram. Soc.*, vol. 90, no. 11, pp. 3485–3489, Nov. 2007.
- [122] Y. Guo, K. I. Kakimoto, and H. Ohsato, “(Na_{0.5}K_{0.5})NbO₃-LiTaO₃ lead-free piezoelectric ceramics,” *Mater. Lett.*, vol. 59, no. 2–3, pp. 241–244, Feb. 2005.
- [123] A. Le Bail, L. M. Cranswick, I. Madsen, A. Fitch, R. Allmann, and C. Giacovazzo, *Powder diffraction: theory and practice*. 2008.
- [124] R. A. Young, “The Rietveld Method,” *International union of crystallography*, vol. 5. International union of crystallography, 1993.
- [125] J. E. Daniels, J. L. Jones, and T. R. Finlayson, “Characterization of domain structures from diffraction profiles in tetragonal ferroelastic ceramics,” *J. Phys. D. Appl. Phys.*, vol. 39, no. 24, pp. 5294–5299, Dec. 2006.
- [126] L. B. McCusker, R. B. Von Dreele, D. E. Cox, D. Louër, and P. Scardi, “Rietveld refinement guidelines,” *J. Appl. Crystallogr.*, vol. 32, no. 1, pp. 36–50, 1999.
- [127] B. H. Toby, “R factors in Rietveld analysis: How good is good enough?,” *Powder Diffr.*, vol. 21, no. 01, pp. 67–70, 2008.

APPENDICES

Appendix A: Image Reduction of Using FIT2D

This appendix covers detailed procedures on reducing 2D Debye-Scherrer rings to 1D XRD plots by utilizing FIT2D, an open-source software package that was developed at the European Synchrotron Research Facility (ESRF) [104]. 2D Debye-Scherrer images collected on a commercial PZT-EC-65 monolithic sample with full electrode configuration under *in situ* electric field with high-energy XRD at beamline 11-ID-C, APS, are used in this analysis as an example. The sample is a rectangular bar with dimensions of 5 mm x 1 mm x 1 mm, and experienced an applied electric field of 0, 1, 2, and 3 kV/mm. A single 2D XRD image is collected at each electric field amplitude. The monochromatic X-ray beam has a wavelength of 0.1173 Å and an energy of 105.7 keV, and the distance between the sample stage and the PerkinElmer 2D area detector is approximately 1500 mm. The detailed experimental setup is illustrated in Figures 2-2, 2-2, and 2-4. The following content includes comprehensive steps of performing data reduction, including experimental geometry calibration, individual 2D image reduction, and multiple 2D image reduction.

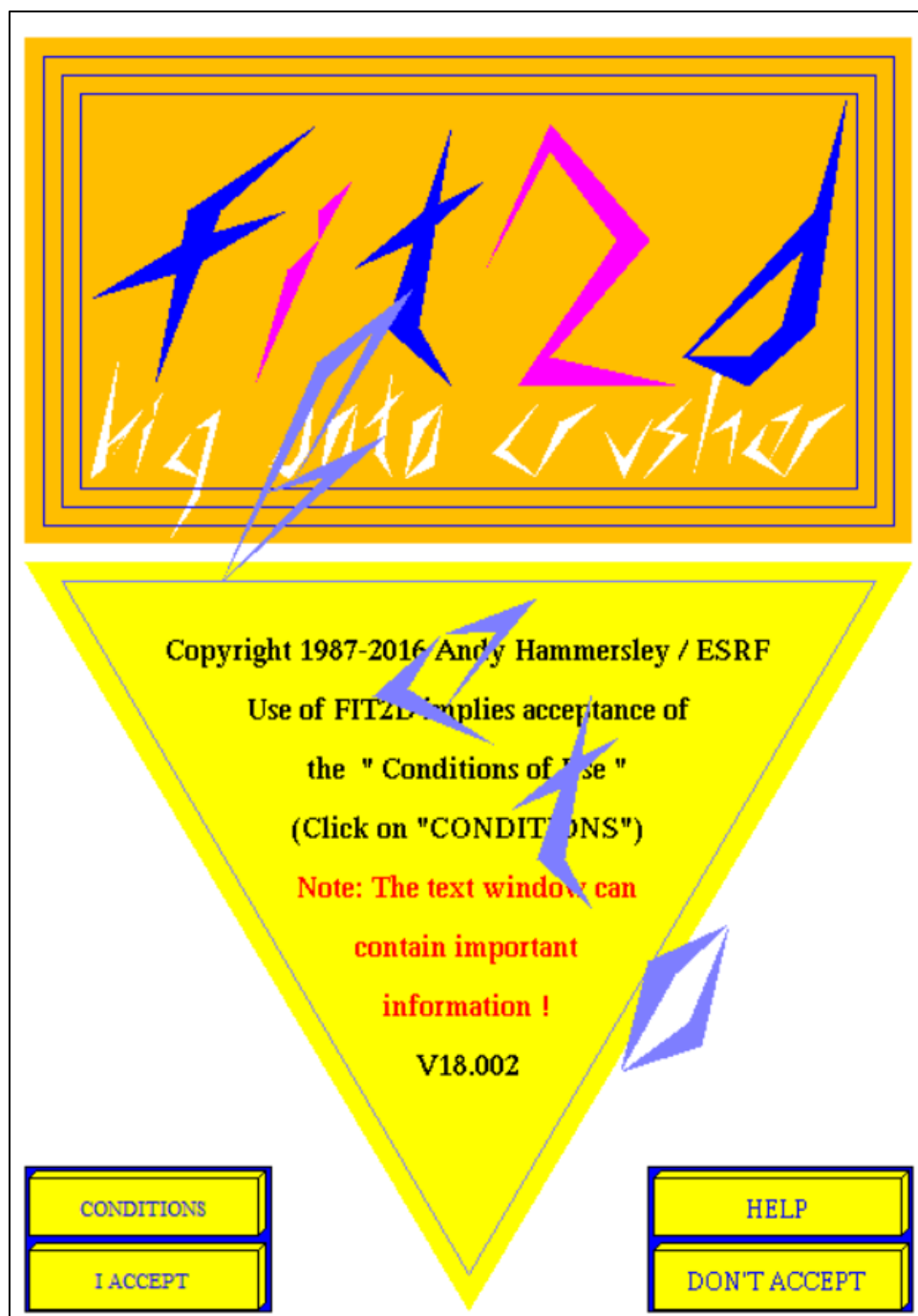


Figure S-1 Program interface of FIT2D.

Experimental Geometry Calibration

Laboratory-based XRD typically collects 1D diffraction patterns with a point or line detector, whereas beamline 11-ID-C utilizes a PerkinElmer 2D area detector. The area detector is composed of 2048 x 2048 pixels in the horizontal and vertical directions, and each pixel is 200 μm x 200 μm . It's critical to conduct an experimental geometry calibration to determine the accurate sample-to-detector distance, X-ray beam center, and the tilt angle between the X-ray beam and the out-of-plane normal of the detector, etc., to ensure the scattering angles and intensities used for data reduction can be precisely defined. The standard material, cerium oxide (CeO_2) powder, was used for calibration of the *in situ* high-energy XRD experiment at beamline 11-ID-C. Besides the CeO_2 powder, other alternative standard materials, such as powdered lanthanum hexaboride (LaB_6), silicon (Si), and titanium dioxide (TiO_2), can be employed in the experimental geometry calibration [123]. Most standard materials are available from the National Institute of Standards and Technology (NIST). The following steps demonstrate how to conduct the experimental geometry calibration in FIT2D:

- (1) Start FIT2D and click "I ACCEPT" to agree the "Conditions of Use", as shown in Figure S-1. In the window of "DIMENSION OF PROGRAM ARRAYS", input 2048 x 2048 pixels in the first and second array and click "O.K." to proceed to the geometry calibration.
- (2) Select the "POWDER DIFFRACTION (2D)" to initiate the calibration and data processing. Input the 2D image of CeO_2 powder collected in beamline 11-ID-C. Accept all default parameters in the window of "CONTROL OF DETECTOR DISTORTION CORRECTIONS". The program interface will be displayed as shown in Figure S-2.

- (3) Click “CALIBRANT” on the left bottom corner of the software interface, as shown in Figure S-2, and select “CERIUM DIOXIDE” as the standard calibrant.
- (4) In the pop-out window of “CALIBRANT PATTERN REFINEMENT”, input the values in the following parameters:
 - (a) Sample to detector distance (mm): 1500
 - (b) Wavelength (Å): 0.1173
 - (c) X pixel size (μm): 200
 - (d) Y pixel size (μm): 200
 - (e) Refine X-ray wavelength: NO

It is unnecessary to refine the X-ray wavelength since the energy is fixed at 105.7 keV.

- (5) Use the “TWO-CLICK” mode to select 4 to 6 points (more than 3 points) on the innermost Debye-Scherrer ring. After the point selection, the software interface will display as shown in Figure S-3. The rings shown in red on the 2D image are simulated for the CeO₂ calibrant, which indicates a completed experimental geometry calibration. Figure S-4 presents the important parameters that are refined from the geometry calibration. These experimental parameters will be required to perform 2D image reduction. For instance, the sample-to-detector distance is calibrated to 1505.132 mm instead of the approximated 1500 mm in the experiment.

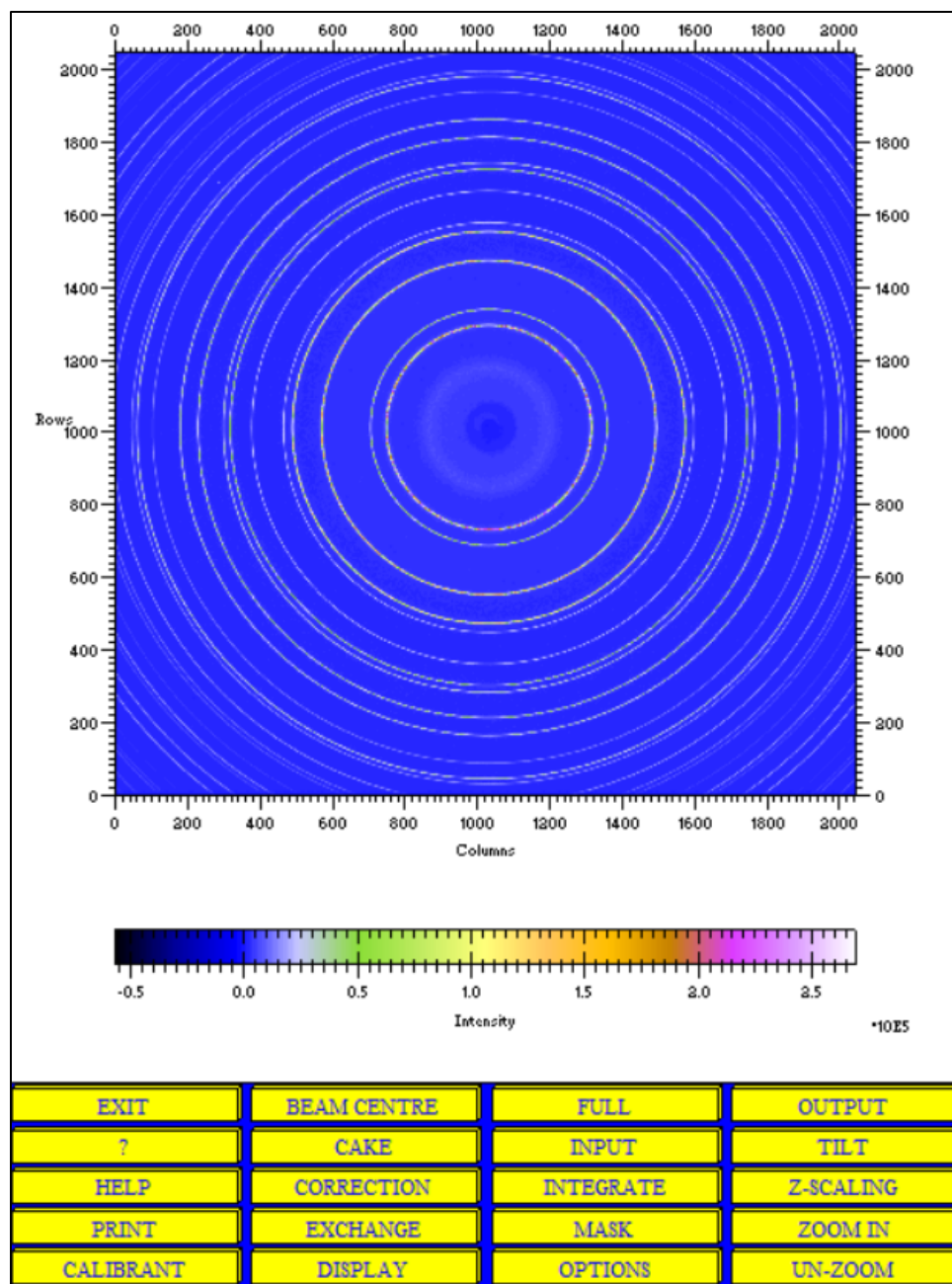


Figure S-2 FIT2D software interface displays the collected 2D Debye-Scherrer rings from standard calibrant CeO₂.

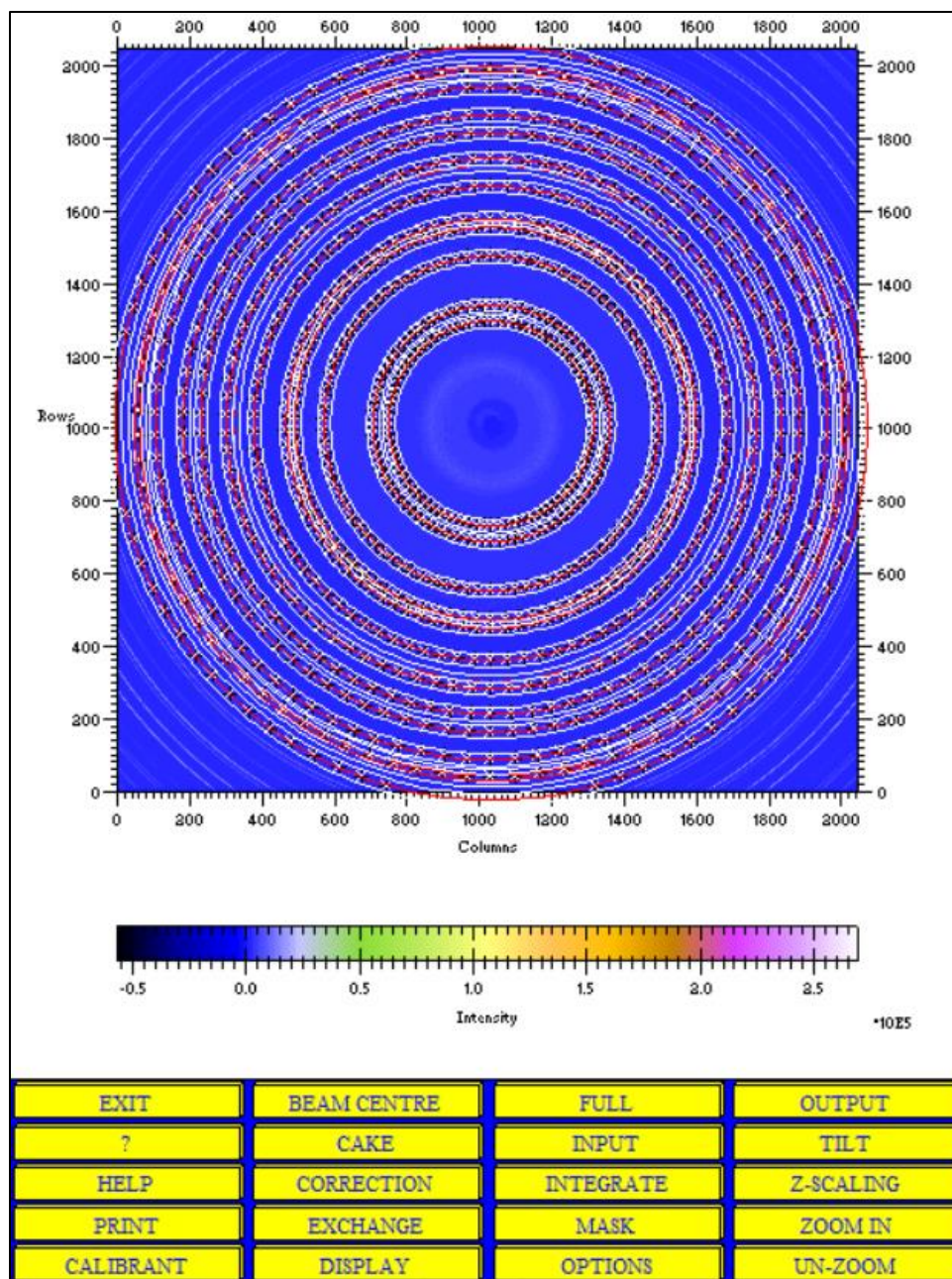


Figure S-3 FIT2D software interface displays the fitted Debye-Scherrer rings for the standard calibrant CeO₂.

EXPERIMENTAL GEOMETRY		
CONTROL FORM		
O.K.	CANCEL	? HELP INFO
DESCRIPTIONS	VALUES	CHANGE
SIZE OF HORIZONTAL PIXELS (MICRONS)	200.0000	X-PIXEL SIZE
SIZE OF VERTICAL PIXELS (MICRONS)	200.0000	Y-PIXEL SIZE
SAMPLE TO DETECTOR DISTANCE (MM)	1505.132	DISTANCE
WAVELENGTH (ANGSTROMS)	0.117300	WAVELENGTH
X-PIXEL COORDINATE OF DIRECT BEAM	1032.616	X-BEAM CENTRE
Y-PIXEL COORDINATE OF DIRECT BEAM	1014.279	Y-BEAM CENTRE
ROTATION ANGLE OF TILTING PLANE (DEGREES)	163.5262	TILT ROTATION
ANGLE OF DETECTOR TILT IN PLANE (DEGREES)	-0.189956	ANGLE OF TILT
ROTATION ANGLE OF DETECTOR X-AXIS FROM HORIZONTAL (DEGREES)	0.0	DETECTOR ROTATION

Figure S-4 FIT2D software interface displays the completed experimental geometry calibration with the appropriate parameters refined.

Individual Image Reduction

Following the experimental geometry calibration, this section provides the procedure to reduce a single 2D Debye-Scherrer image into multiple 1D XRD plots with respect to the azimuthal angle. The 2D image acquired from the tetragonal commercial PZT-EC-65 sample under the application of an electric field at 3kV/mm is used as an example in this section.

- (1) After completing the experimental geometry calibration, input the 2D image file from the experiment using PZT-EC-65 with an applied field of 3 kV/mm.
- (2) Click on the “CAKE” button to divide the 2D image into multiple azimuthal sectors. Select “NO CHANGE” to activate further image division.
- (3) In the window of “TYPE OF AZIMUTH/RADIAL OR 2THETA TRANSFORMATION”, input the following values in related parameters,
 - (a) Start azimuthal angle (Degrees): 172.5
 - (b) End azimuthal angle (Degrees): 7.5
 - (c) Inner radial limit (Pixels): 0.0
 - (d) Outer radial limit (Pixels): 750
 - (e) Number of azimuthal bins: 13
 - (f) Number of radial/2theta bins: 2000

The above conditions will create 13 azimuthal sectors in total with an integration range of 15°. Keep the other parameters at their default values and finish the integration.

- (4) Click “EXIT” in the pop-out window and “OUTPUT” the integrated 1D XRD plots. There are several file formats to output the integrated data, including CHILOT, MULTI-CHILOTS, 2D-ASCII, FULLPROF, etc. The file format of “MULTI-CHILOTS” files are employed here since they can be directly analyzed in

GSAS, GSAS-II, LIPRAS, MAUD, or imported into Excel, Matlab, and OriginLab, etc., for further calculations. Since the 2D image is divided into 13 azimuthal sectors, there will be 13 CHI files outputted from each individual sector.

- (5) The outputted files named with suffix 1, 2, 3, 4, 5, 6, 7, 8, 9, 10, 11, 12, 13 correspond to the azimuthal sector of 180° , 165° , 150° , 130° , 120° , 105° , 90° , 75° , 60° , 45° , 30° , 15° , 0° , respectively. Figure S-5 presents the 1D XRD plots for all individual azimuthal sectors from the commercial PZT-EC-65 sample at 3 kV/mm.

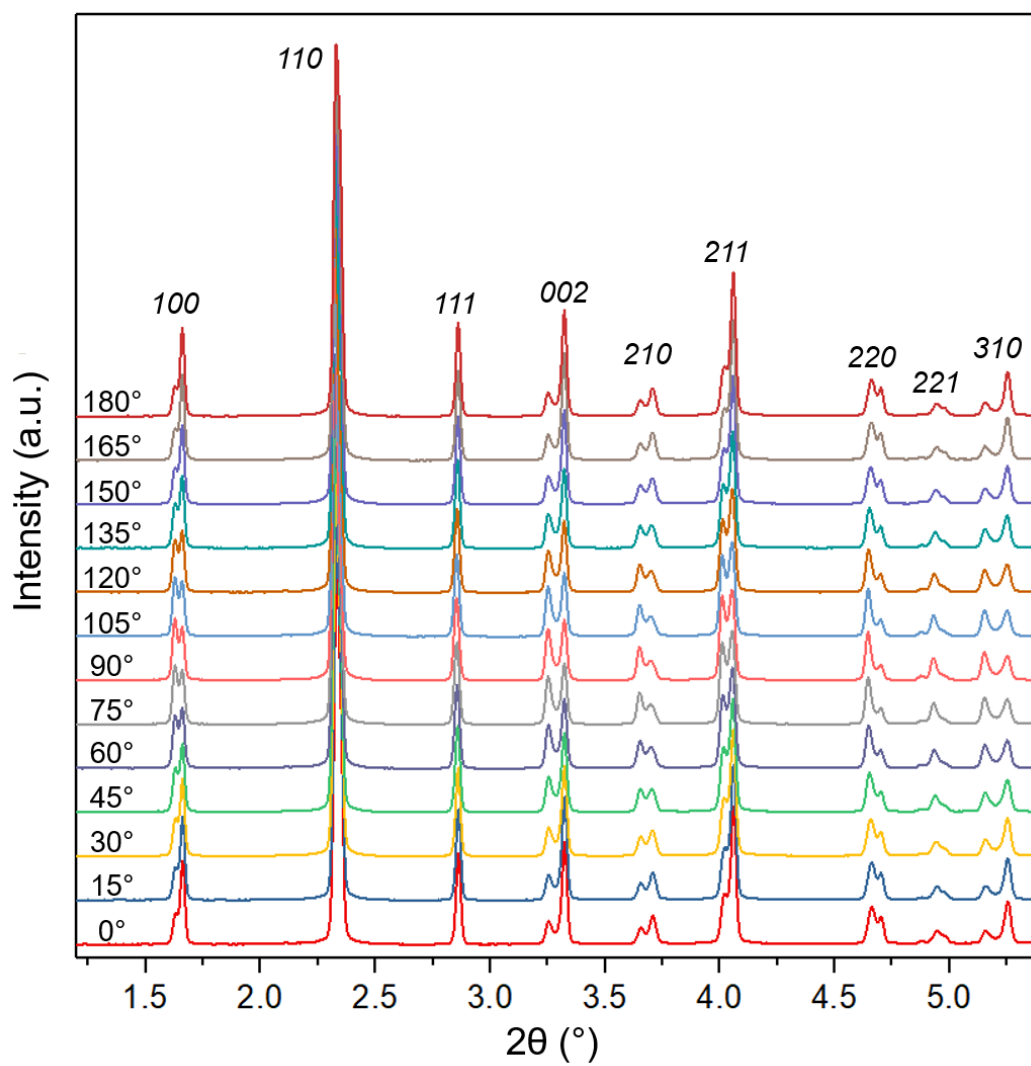


Figure S-5 XRD plots integrated from each azimuthal sector from the tetragonal phase commercial PZT-EC-65 sample with the full-electrode configuration.

Multiple Image Reduction

This section introduces the comprehensive procedures of using a MACRO programming script to process multiple 2D images simultaneously. The 2D images from the tetragonal phase commercial PZT-EC-65 ferroelectric sample were collected at 0 kV/mm (virgin state), 1 kV/mm, 2 kV/mm, and 3 kV/mm, respectively.

- (1) Start the FIT2D software and conduct the experimental geometry calibration using the 2D image of standard calibrant CeO₂ as explained in the earlier section.
- (2) Return to the main software interface and select “MACROS/LOG FILE”. Click “CREATE MACRO” to generate a programming script for later batch analysis of 2D images.
- (3) Return to “POWDER DIFFRACTION (2-D)” and input the 2D image at 0 kV/mm.
- (4) Repeat steps 2, 3, and 4 from “Individual Image Reduction”.
- (5) After outputting the 1D XRD plots in the form of “MULTI-CHILOTS”, click “EXCHANGE” to return the program interface from 1D plot to the 2D image.
- (6) Return to the main software interface and back to “MACRO/LOG FILE” to stop recording the operating steps for generating the MACRO programming script.
- (7) Open the Macro file with Notepad (or other similar text file editor) in the folder, add “#IN” and “#OUT” after certain lines and save the changes, as illustrated in the example.
- (8) Return to “MACRO/LOG FILE” and click “RUN SEQUENCE”. Select the generated MACRO programming script, then choose the 2D image collected at 1kV/mm as the initial image, and the image acquired at 3 kV/mm as the last image in this batch reduction, and then activate the multiple image reduction. Since each 2D image is divided into 13

azimuthal sectors, there will be 28 1D XRD plots stored individually in the “CHI” file for the 4 images collected at different electric field states.

The integrated 1D XRD plots can be used to compare domain texture in different azimuthal sectors as a function of field amplitude. Figure S-6 presents the 200 peak in the 0°, 30°, 60°, and 90° azimuthal sectors as a function of electric field amplitudes. As illustrated in the figure, the intensity of 002 reflection increases as a function of azimuthal angle from 0° to 90°, which is because the 002 domains are parallel to the electric field direction.

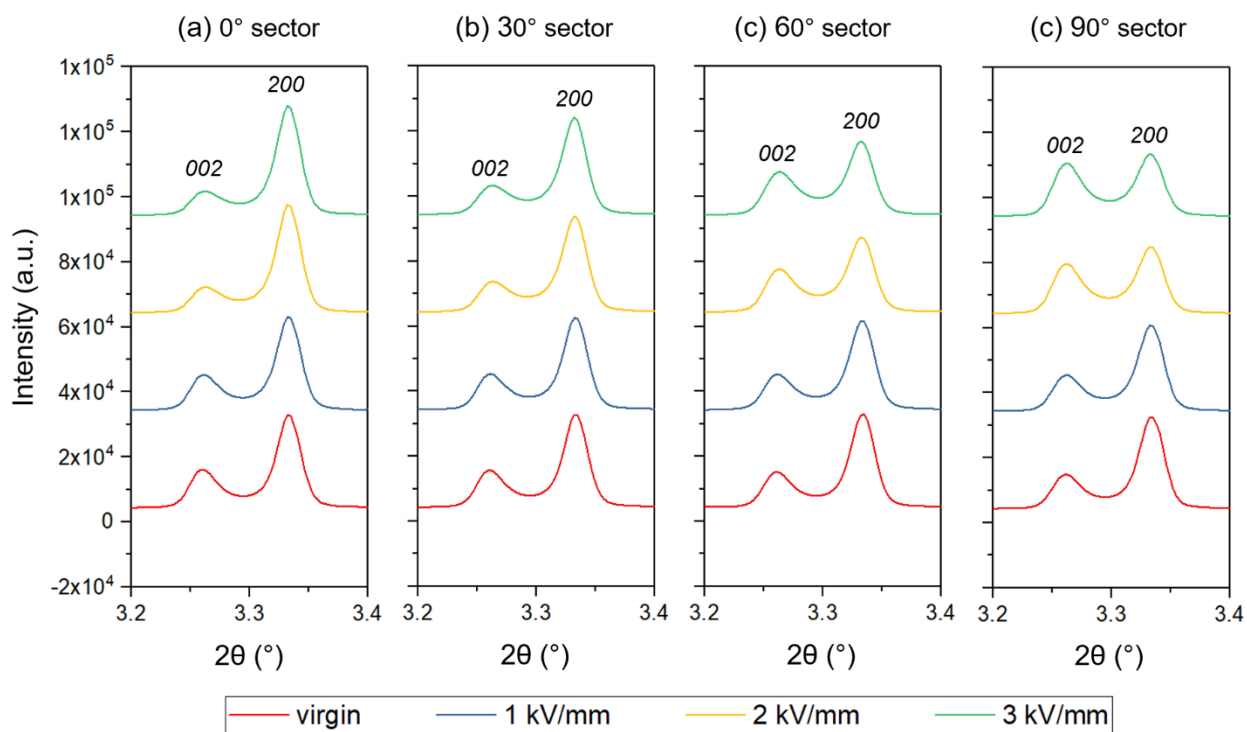


Figure S-6 Peak intensity changes in the (a) 0°, (b) 30°, (c) 60°, and (d) 90° azimuthal sector as a function of electric field amplitude, for the tetragonal phase commercial PZT-EC-65 material.

Example of a MACRO Programming Script used for Multiple Image Reduction

```
%!*\  
%!*\  
%!*\  
%!*\  
EXIT  
POWDER DIFFRACTION (2-D)  
INPUT  
#IN  
O.K.  
CAKE  
NO CHANGE  
0  
0  
0  
1  
1.7717006E+03  
1.0114689E+03  
INTEGRATE  
O.K.  
START AZIMUTH  
172.5  
END AZIMUTH  
7.5  
OUTER RADIUS  
750  
AZIMUTH BINS  
13  
RADIAL BINS  
2000  
O.K.  
EXIT  
OUTPUT  
#OUT  
MULTI-CHIPLOT  
O.K.  
EXCHANGE  
EXIT  
MACROS / LOG FILE  
%!*\  
END OF IO MACRO FILE
```

Appendix B: Peak Fitting in LIPRAS

This appendix presents various profile functions to describe the peak shapes and function selection for different phases in the examined ferroelectric materials.

Peak Shape Functions

There are four main profile functions used for describing Bragg peak shapes in diffraction as a function of 2θ , which is written as x in Equations A(1) – A(4), including Gaussian, Lorentzian, Pseudo-Voigt, and Pearson VII [124].

$$\text{Gaussian:} \quad G(x) = I \frac{2\sqrt{\ln 2}}{H_K \sqrt{\pi}} \exp \left[\frac{-4 \ln 2 (x - x_0)^2}{H_K^2} \right] \quad \text{A(1)}$$

$$\text{Lorentzian:} \quad L(x) = I \frac{2}{H_K \pi} \left[1 + \frac{4(x - x_0)^2}{H_K^2} \right]^{-1} \quad \text{A(2)}$$

$$\text{Pseudo-Voigt:} \quad PV(x) = (1 - \eta)G(x) + \eta L(x) \quad \text{A(3)}$$

$$\text{Pearson VII:} \quad PVII(x) = I \frac{2\Gamma(m)\sqrt{2^{1/m} - 1}}{\Gamma(m - 0.5)H_K \sqrt{\pi}} \left[1 + 4(2^{1/m} - 1) \frac{(x - x_0)^2}{H_K^2} \right]^{-m} \quad \text{A(4)}$$

where,

x_0 (2θ) is the center of the peak position,

I is the integrated intensity,

H_K is the full-width at half-maximum (FWHM) of the K^{th} Bragg peak,

η is the linear mixing parameter, $0 \leq \eta \leq 1$

$m = NA + NB/x + NC/x^2$, in which NA , NB , and NC are refinable variables,

Γ is the gamma function.

As illustrated in Equation A(3), the Pseudo-Voigt shape function is a linear combination of Gaussian and Lorentzian functions. Figure S-7 presents a comparison of multiple Pseudo-Voigt functions using different linear mixing parameters. Since $0 \leq \eta \leq 1$, the Pseudo-Voigt function is completely Gaussian when $\eta = 0$, and it becomes a Lorentzian function when $\eta = 1$.

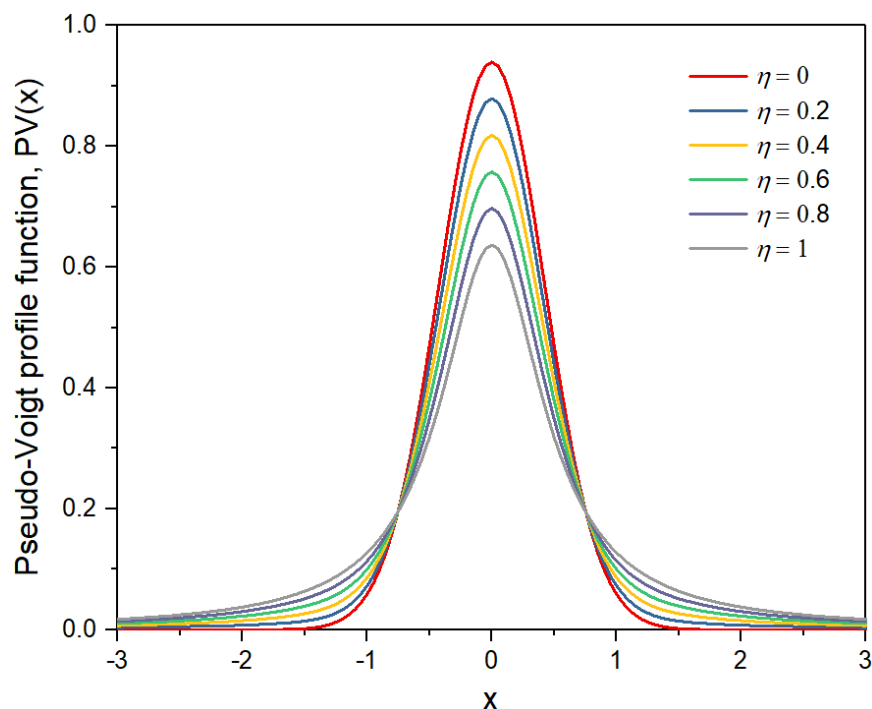


Figure S-7 Representative Pseudo-Voigt profile functions with different mixing parameter values. These functions set $x_0 = 0$ and $H_K = 1$.

The Pearson VII profile function includes a power parameter, m , to describe the peak shape. It is a reasonable approximation to consider the Pearson VII function roughly equivalent to a Gaussian function when $m > 10$, while it approaches a Lorentzian function shape when $m \approx 1$. In ferroelectric materials, both Pseudo-Voigt and Pearson VII profile functions are extensively used in peak fitting analysis.

Under the application of an electric field, domain reorientation takes place in ferroelectric material, which gives rise to interchanging intensities among degenerate diffraction peaks. However, these degenerate peaks frequently exhibit asymmetric shapes because of diffuse scattering that may result from domain walls, intergranular stress, nano-polar regions, etc. Under such circumstances, a modified profile function, the asymmetric Pearson VII, which is a combination of two individual Pearson VII functions, can be effectively employed to describe such asymmetric peaks. Equation A(5) presents the profile functions with respect to x (2θ) [125].

Asymmetric Pearson VII:

$$APVII(x) = \begin{cases} N_L \frac{2\Gamma(m_L)\sqrt{2^{1/m_L} - 1}}{\Gamma(m_L - 0.5)H_{KL}\sqrt{\pi}} \left[1 + 4(2^{1/m_L} - 1) \frac{(x - x_0)^2}{H_{KL}^2} \right]^{-m_L}, & \text{for } x < x_0 \\ N_R \frac{2\Gamma(m_R)\sqrt{2^{1/m_R} - 1}}{\Gamma(m_R - 0.5)H_{KR}\sqrt{\pi}} \left[1 + 4(2^{1/m_R} - 1) \frac{(x - x_0)^2}{H_{KR}^2} \right]^{-m_R}, & \text{for } x \geq x_0 \end{cases} \quad A(5)$$

where L and R stand for the left-hand and right-hand sides of the central peak position (x_0), respectively. N_L and N_R are the integrated intensities on either side of x_0 , hence the overall intensity of the K^{th} Bragg peak becomes:

$$I = \frac{1}{2} (N_L + N_R) \quad A(6)$$

There are several criteria to interpolate how well the line-profile analysis result is, including R_{wp} , R_{exp} , and χ^2 , as shown in Equations A(7) - A(9) [126]. These criteria are also used for demonstrating the Rietveld refinement results.

$$R_{wp} = \left\{ \sum_i w_i [y_i(obs) - y_i(calc)]^2 / \sum_i w_i [y_i(obs)]^2 \right\}^{1/2} \quad A(7)$$

$$R_{exp} = \left[(N - P) / \sum_i w_i [y_i(obs)]^2 \right]^{1/2} \quad A(8)$$

$$\chi^2 = R_{wp} / R_{exp} \quad A(9)$$

where $y_i(obs)/y_i(calc)$ is the observed/calculated intensity at step i , and w_i is the weight; N is the total data points in the XRD pattern, and P is the number of parameters refined in the line-profile analysis. R_{wp} is a weighted factor that is most commonly reported value to represent the quality of the analysis; R_{exp} is another gauge to describe the peak fitting result based on the counting statistics; χ^2 is the ratio of R_{wp} and R_{exp} , which is also referred to as the goodness of fit.

For a reasonable line-profile analysis, R_{wp} and R_{exp} are often less than 3% because only one or two peaks are fitted at a time. For a good Rietveld refinement, R_{wp} and R_{exp} may be less than 10% since there are multiple reflections in the analysis. However, It is worth noting that one should be careful to trust the fitting results since they can be influenced by many factors, such as the total number of data points, background functions, shape functions, false minima, etc. As suggested by B. H. Toby, who is the program developer of GSAS/GSAS-II, the best way to determine a Rietveld refinement quality is graphically comparing the modeled pattern with the observed pattern [127].

Profile Function Selection for Different Phases

A part of this work introduces domain reorientation in various crystallographic phases under the application of electric fields, which is used for determining the most preferred domain texture with respect to the angle to macroscopic field direction. It is important to select the most appropriate profile function to fit and describe the peak shape in specific phases. Figures S-8, 9, and 10 provide comparisons of employing Pseudo-Voigt and asymmetric Pearson VII profile functions in tetragonal, rhombohedral, and orthorhombic phases for ferroelectric materials under the application of 3 kV/mm. The 90° azimuthal sector, which is parallel to the macroscopic field direction, is used as an example in the analyses presented here.

For the tetragonal phase, the comparison in Figure S-8 shows that the asymmetric Pearson VII functions are superior in this case for modeling peak shoulders and shape asymmetry, versus the Pseudo-Voigt functions. The fitting results, represented by the weighted profile R-factor (R_{wp}), are 3.95% and 1.65% for the analyses in Figure S-8 for (a) Pseudo-Voigt and (b) Pearson-VII, respectively, which quantitatively shows that asymmetric Pearson VII profile functions are better for tetragonal phase analysis. Specifically, to avoid the contribution of diffuse scattering to peak intensity and shape asymmetry, only N_L of 002_T and N_R of 200_T are utilized in the domain texture strength calculation in the tetragonal phase. For the rhombohedral phase, as shown in Figure S-9, there is not a significant difference with the employment of either Pseudo-Voigt or asymmetric Pearson VII profile functions in fitting the peaks. However, for ease of calculating the degree of domain alignment, the Pseudo-Voigt profile function is selected to analyze the rhombohedral phase. For the orthorhombic phase, the results in Figure S-10 prove that the application of three Pseudo-Voigt profile functions are better for fitting the reflections in the pseudo-monoclinic frame, which exhibits reasonable peak positions, better fits to the shape, and lower R_{wp} values.

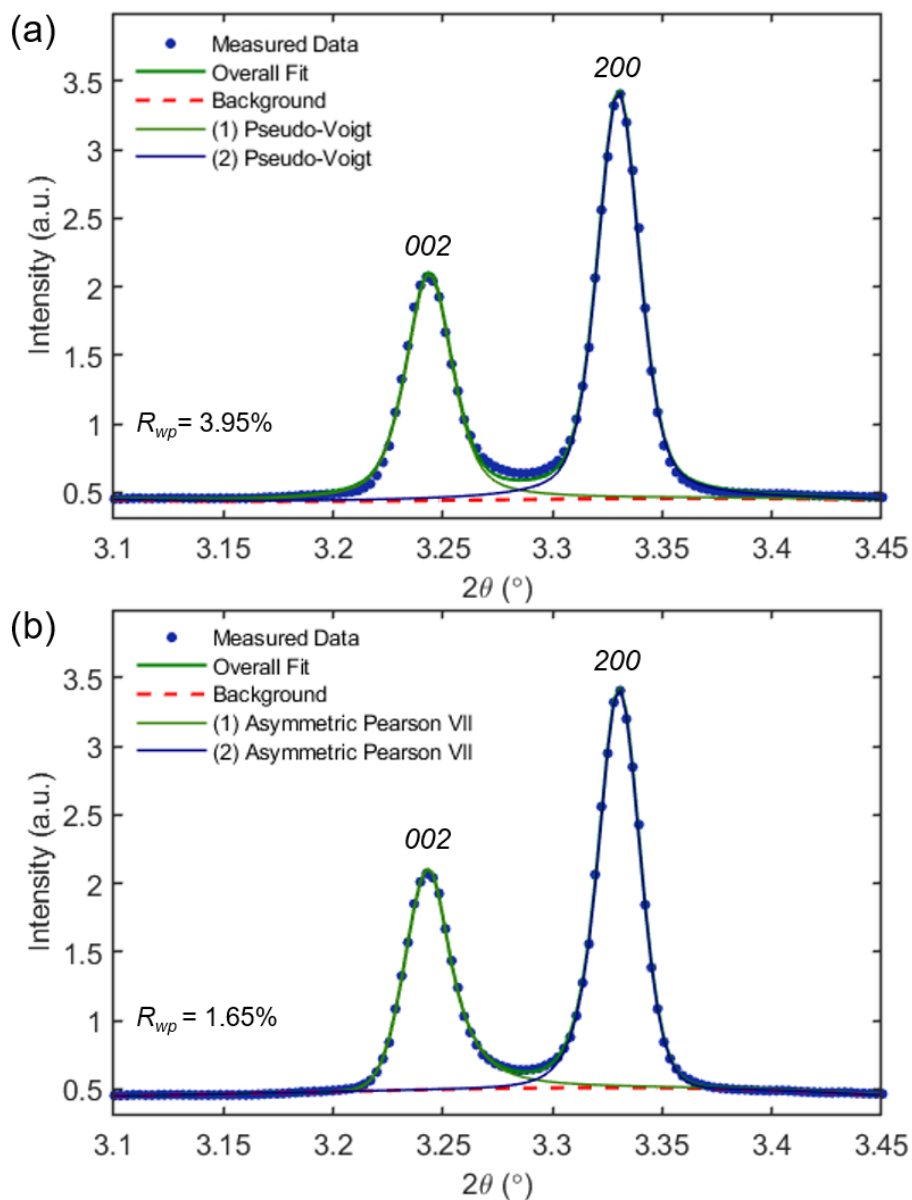


Figure S-8 Peak fitting analysis on 002 and 200 reflections parallel to the macroscopic electric field direction in the tetragonal phase Nb-PZT 50/50 full-electrode sample at 3 kV/mm, using (a) Pseudo-Voigt, and (b) asymmetric Pearson VII profile functions.

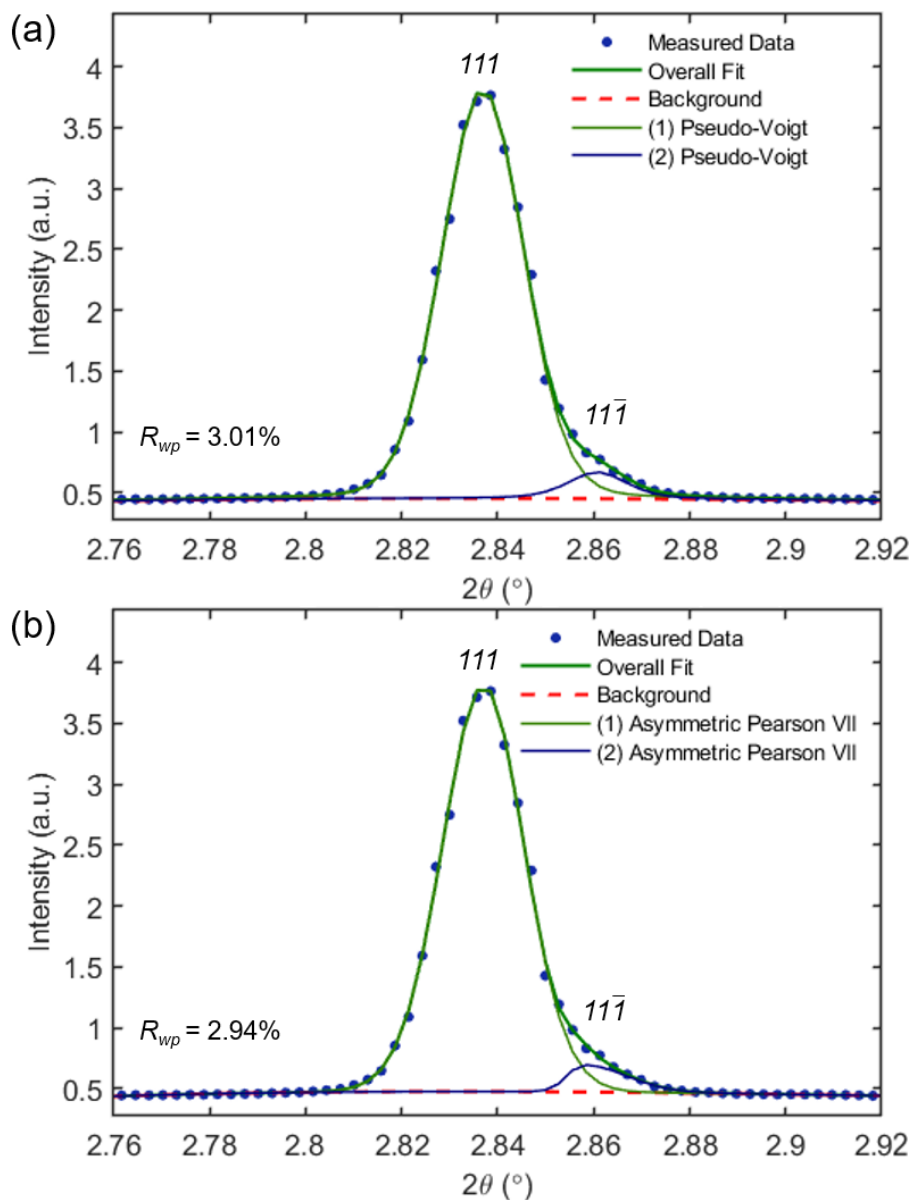


Figure S-9 Peak fitting analysis on 111 and $1\bar{1}\bar{1}$ reflections parallel to the macroscopic electric field direction in the rhombohedral phase Nb-PZT 56/44 full-electrode sample at 3 kV/mm, using (a) Pseudo-Voigt, and (b) asymmetric Pearson VII profile functions.

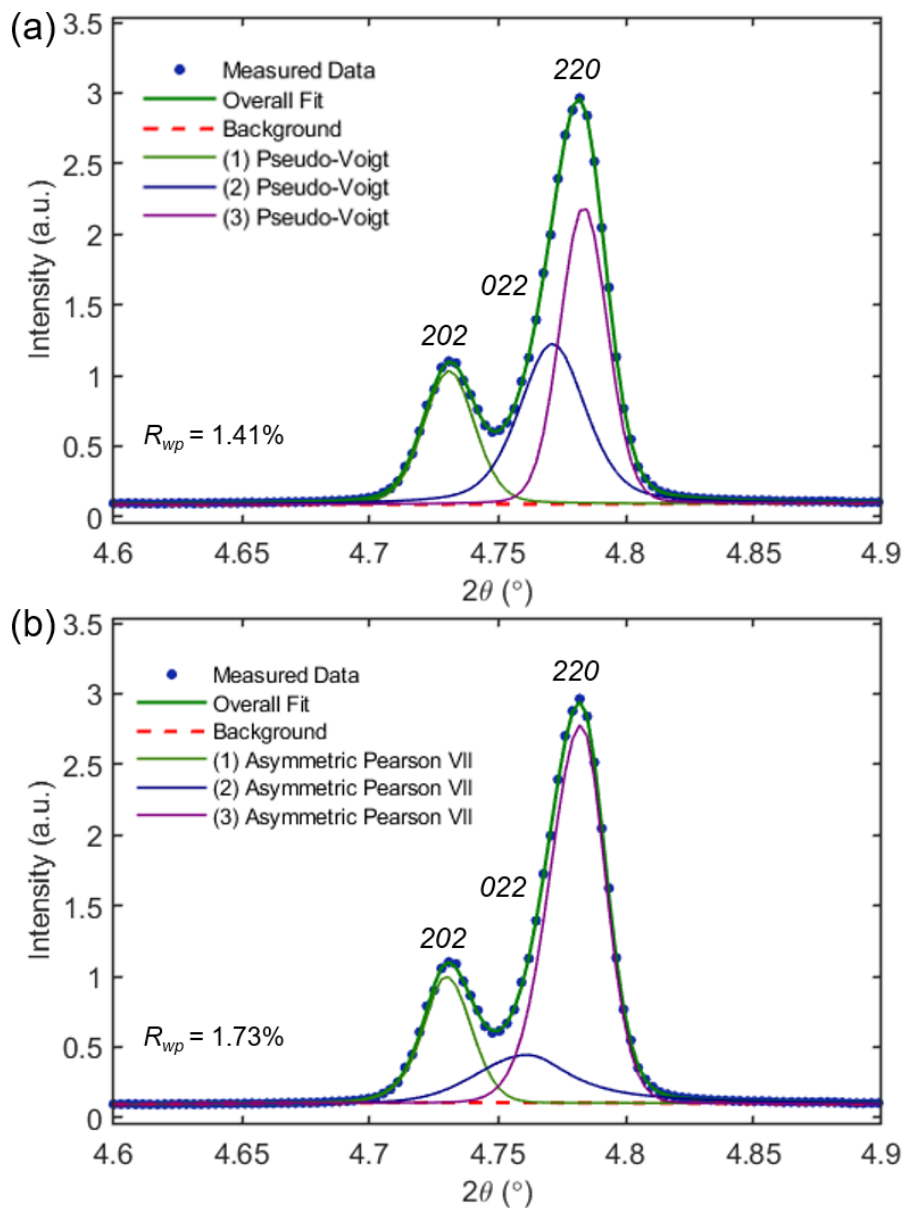


Figure S-10 Peak fitting analysis on 202, 022, and 220 reflections parallel to the macroscopic electric field direction in the pseudo-monoclinic (orthorhombic) phase undoped KNN full-electrode sample at 3 kV/mm, using (a) Pseudo-Voigt, and (b) asymmetric Pearson VII profile functions.

Appendix C: Supplementary Figures

▪ Representative pixels in the Nb-PZT 53/47 partial-electrode sample, whole bar scan

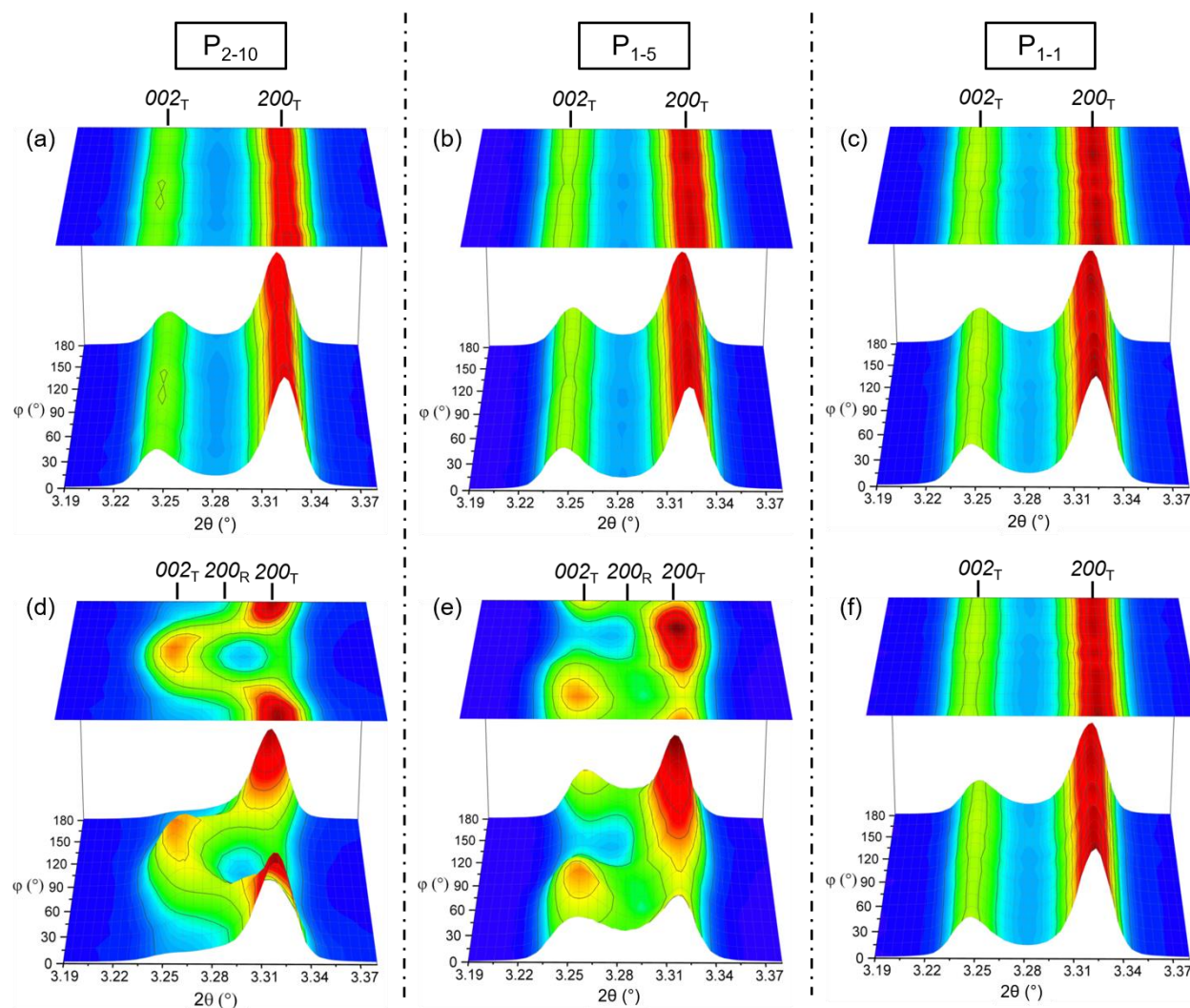


Figure S-11 Peak intensities as a function of azimuthal angle (ϕ) for P_{2-10} , P_{1-5} , and P_{1-1} in the Nb-PZT 53/47 partial-electrode sample with the whole bar scan pattern. Plots (a), (b), (c) present the peak intensities in the virgin state, and (d), (e), (f) show the interchanged intensities at 3 kV/mm for P_{2-10} , P_{1-5} , and P_{1-1} , respectively.

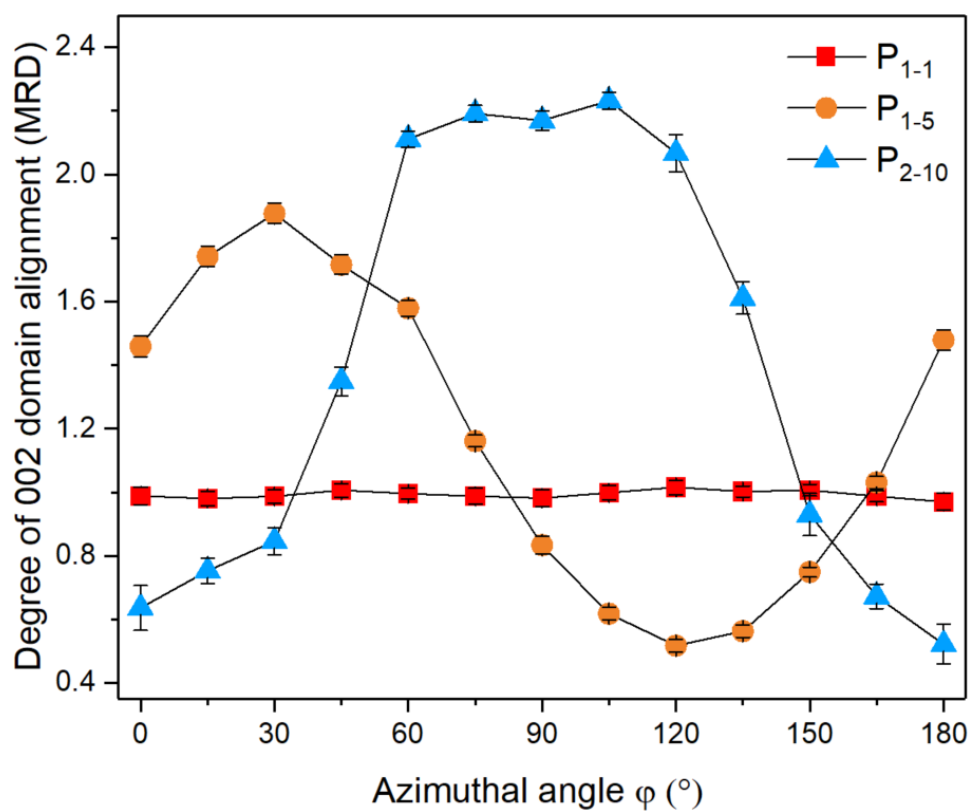


Figure S-12 The degree of 002 domain alignment (MRD) of representative pixels P_{2-10} , P_{1-5} , and P_{1-1} in the Nb-PZT 53/47 partial-electrode sample with the whole bar scan pattern at 3 kV/mm.

▪ Representative pixels in the Nb-PZT 56/44 partial-electrode sample, whole bar scan

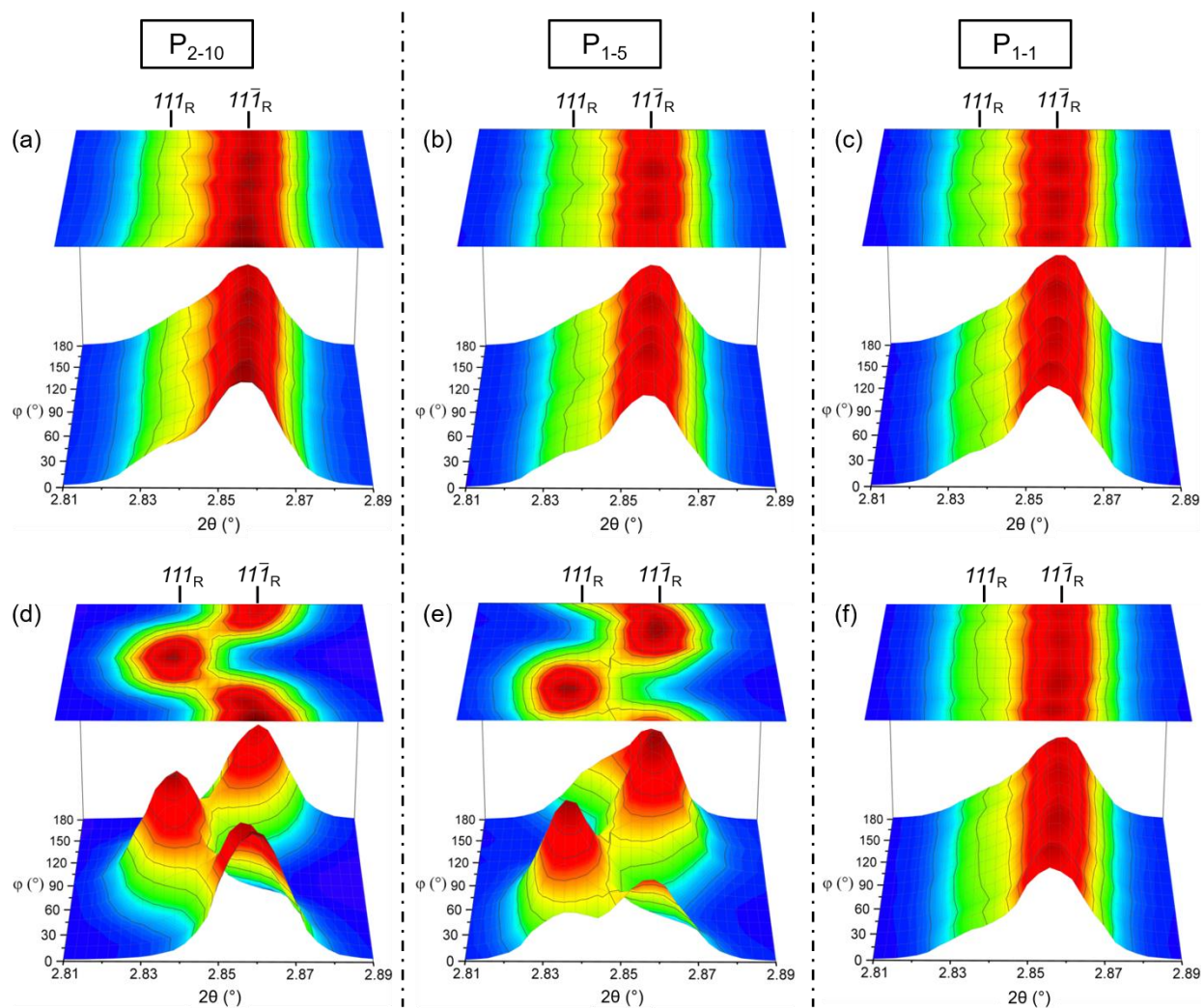


Figure S-13 Peak intensities as a function of azimuthal angle (φ) for P_{2-10} , P_{1-5} , and P_{1-1} in the Nb-PZT 56/44 partial-electrode sample with the whole bar scan pattern. Plots (a), (b), (c) present the peak intensities in the virgin state, and (d), (e), (f) show the interchanged intensities at 3 kV/mm for P_{2-10} , P_{1-5} , and P_{1-1} , respectively.

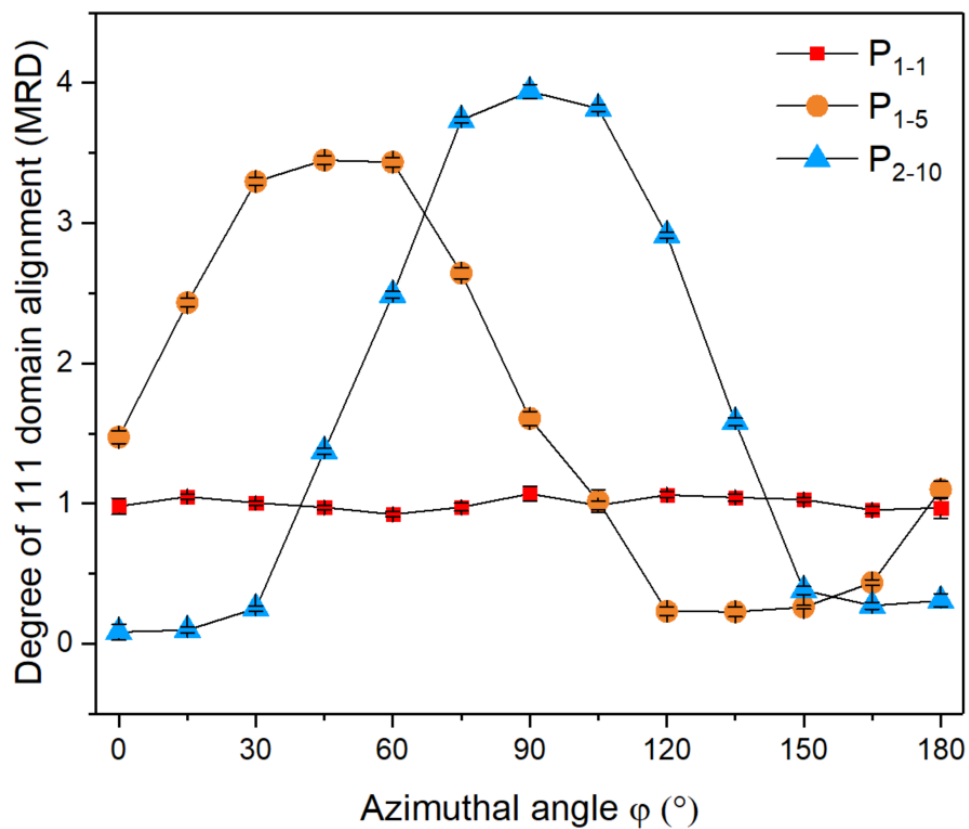


Figure S-14 The degree of 111 domain alignment (MRD) of representative pixels P_{2-10} , P_{1-5} , and P_{1-1} in the Nb-PZT 56/44 partial-electrode sample with the whole bar scan pattern at 3 kV/mm.

▪ Representative pixels in the doped KNN partial-electrode sample, whole bar scan

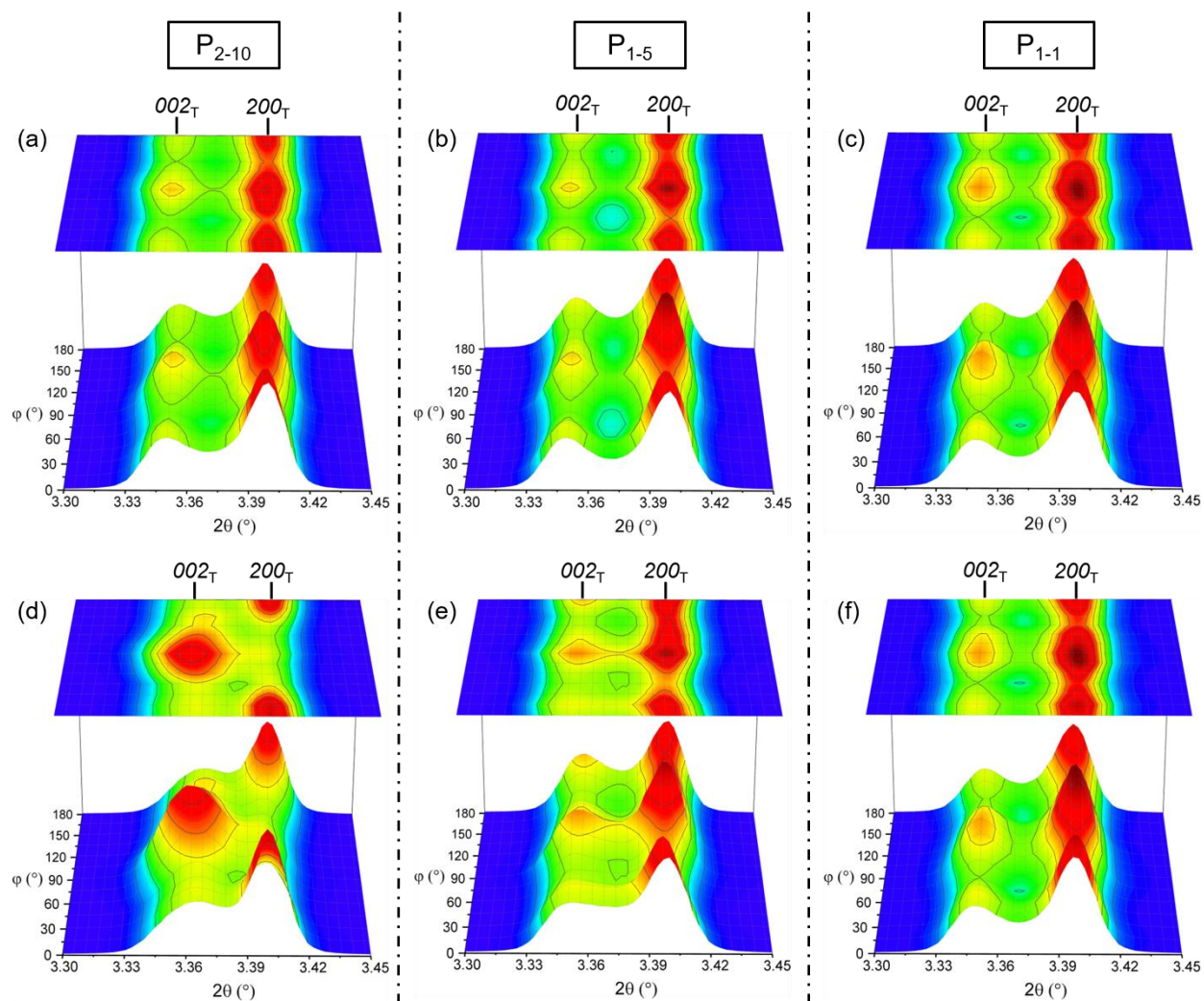


Figure S-15 Peak intensities as a function of azimuthal angle (ϕ) for P_{2-10} , P_{1-5} , and P_{1-1} in the doped KNN partial-electrode sample with the whole bar scan pattern. Plots (a), (b), (c) present the peak intensities in the virgin state, and (d), (e), (f) show the interchanged intensities at 3 kV/mm for P_{2-10} , P_{1-5} , and P_{1-1} , respectively.

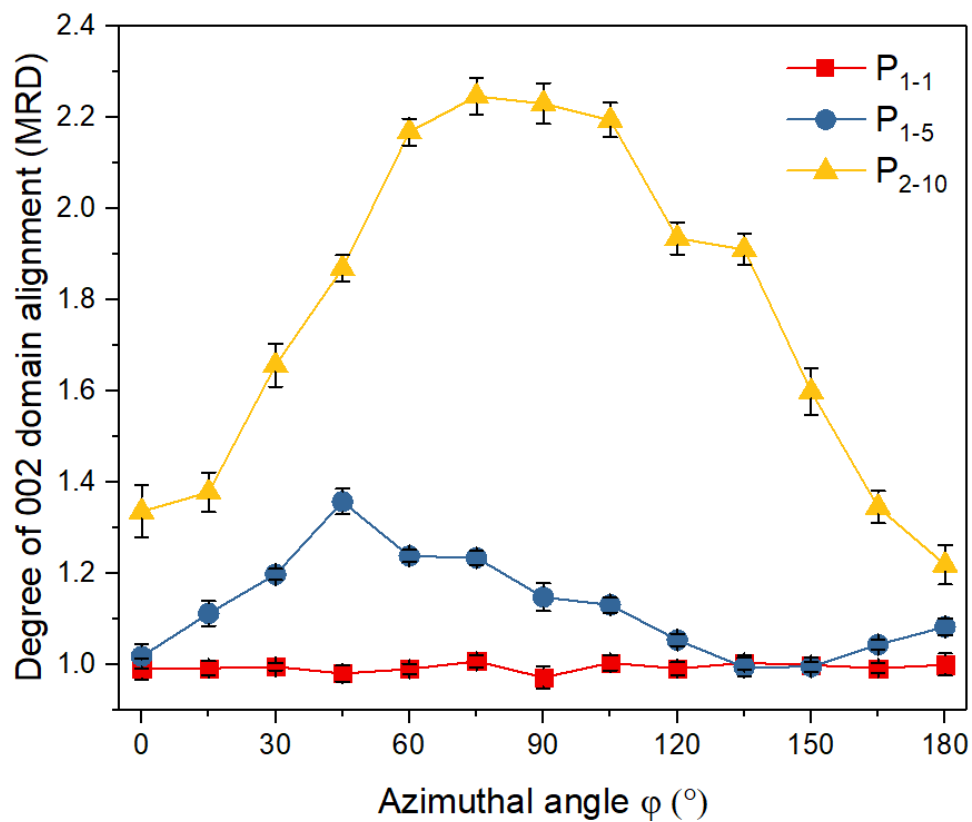


Figure S-16 The degree of 002 domain alignment (MRD) of representative pixels P_{2-10} , P_{1-5} , and P_{1-1} in the doped KNN partial-electrode sample with the whole bar scan pattern at 3 kV/mm.

- Representative pixels in the Nb-PZT 50/50 partial-electrode sample, electrode edge scan

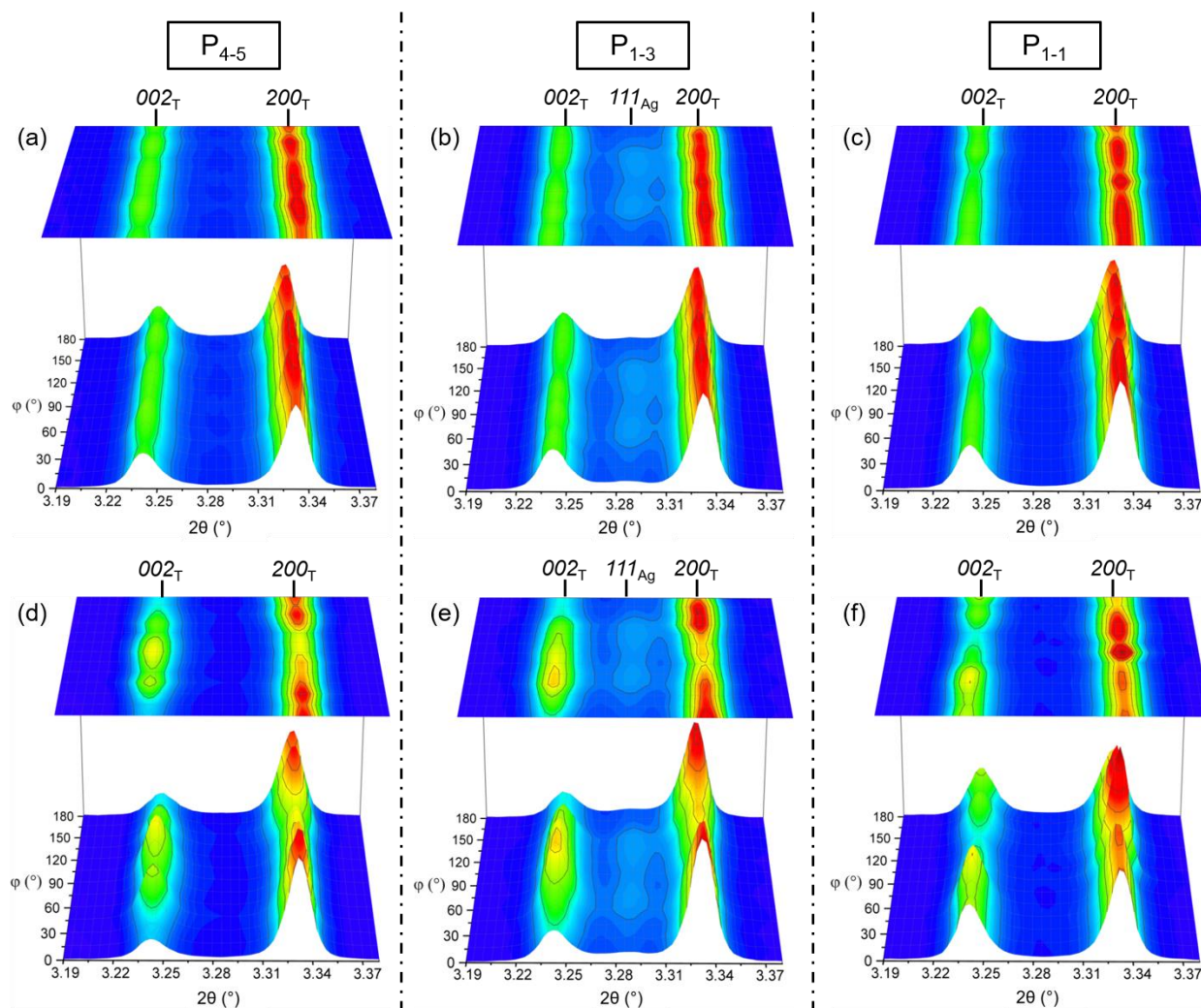


Figure S-17 Peak intensities as a function of azimuthal angle (φ) for P_{4-5} , P_{1-3} , and P_{1-1} in the Nb-PZT 50/50 partial-electrode sample with the electrode edge scan pattern. Plots (a), (b), (c) present the peak intensities in the virgin state, and (d), (e), (f) show the interchanged intensities at 3 kV/mm for P_{4-5} , P_{1-3} , and P_{1-1} , respectively.

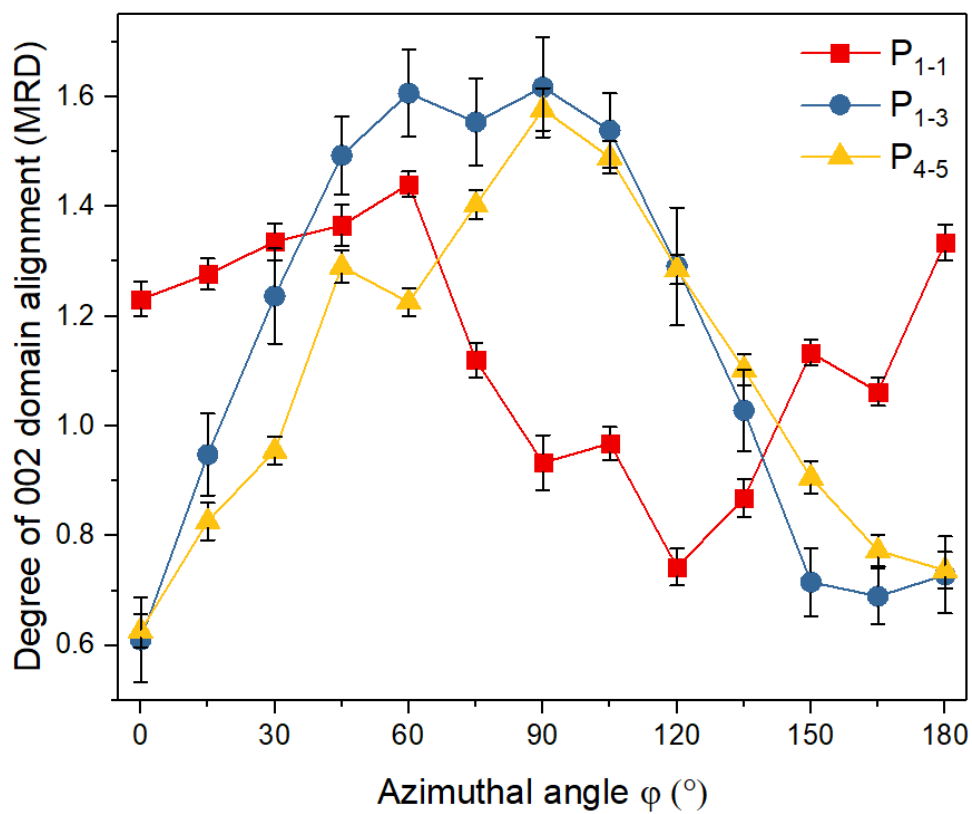


Figure S-18 The degree of 002 domain alignment (MRD) of representative pixels P_{4-5} , P_{1-3} , and P_{1-1} in the Nb-PZT 50/50 partial-electrode sample with the electrode edge scan pattern at 3 kV/mm.

- Representative pixels in the Nb-PZT 56/44 partial-electrode sample, electrode edge scan

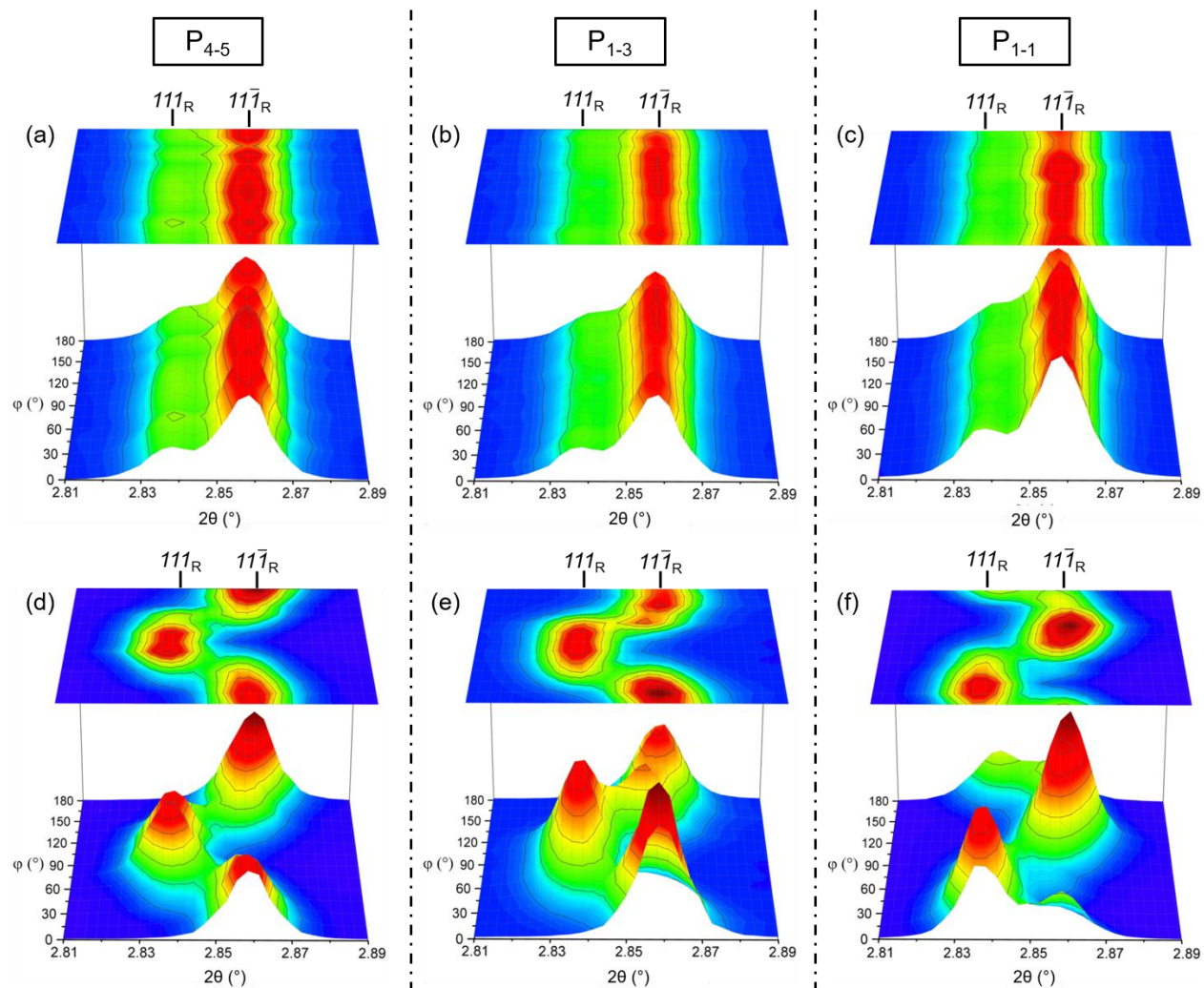


Figure S-19 Peak intensities as a function of azimuthal angle (φ) for P_{4-5} , P_{1-3} , and P_{1-1} in the Nb-PZT 56/44 partial-electrode sample with the electrode edge scan pattern. Plots (a), (b), (c) present the peak intensities in the virgin state, and (d), (e), (f) show the interchanged intensities at 3 kV/mm for P_{4-5} , P_{1-3} , and P_{1-1} , respectively.

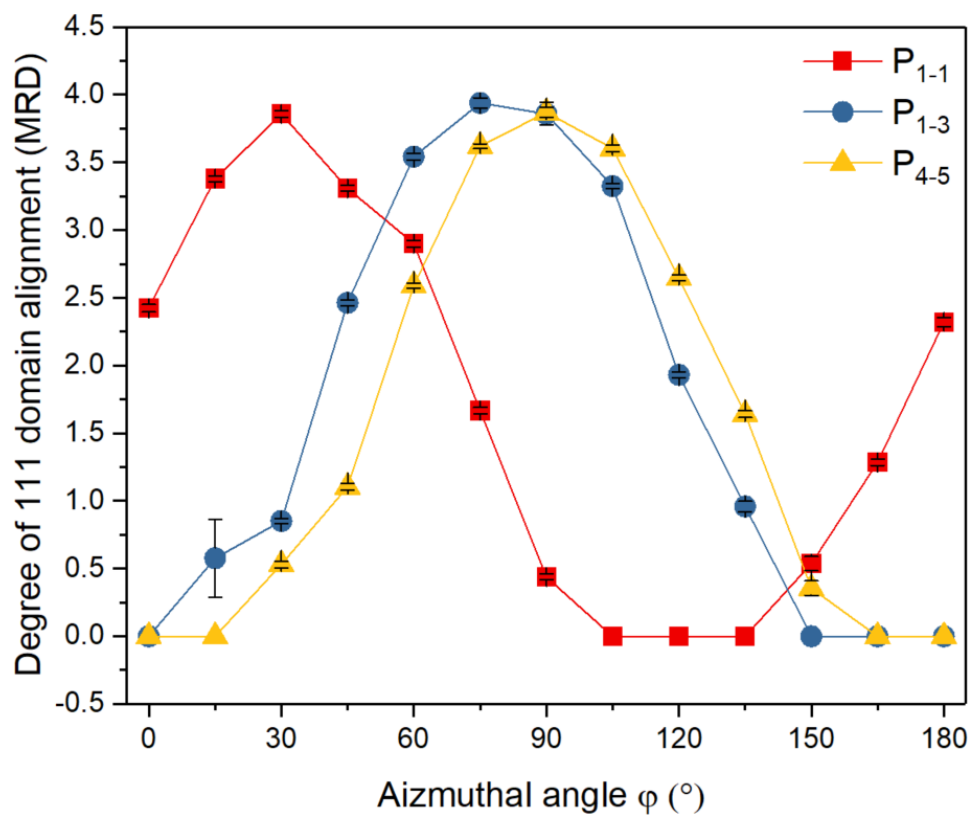


Figure S-20 The degree of 111 domain alignment (MRD) of representative pixels P_{4-5} , P_{1-3} , and P_{1-1} in the Nb-PZT 56/44 partial-electrode sample with the electrode edge scan pattern at 3 kV/mm.

- **Representative pixels in the undoped KNN partial-electrode sample, electrode edge scan**

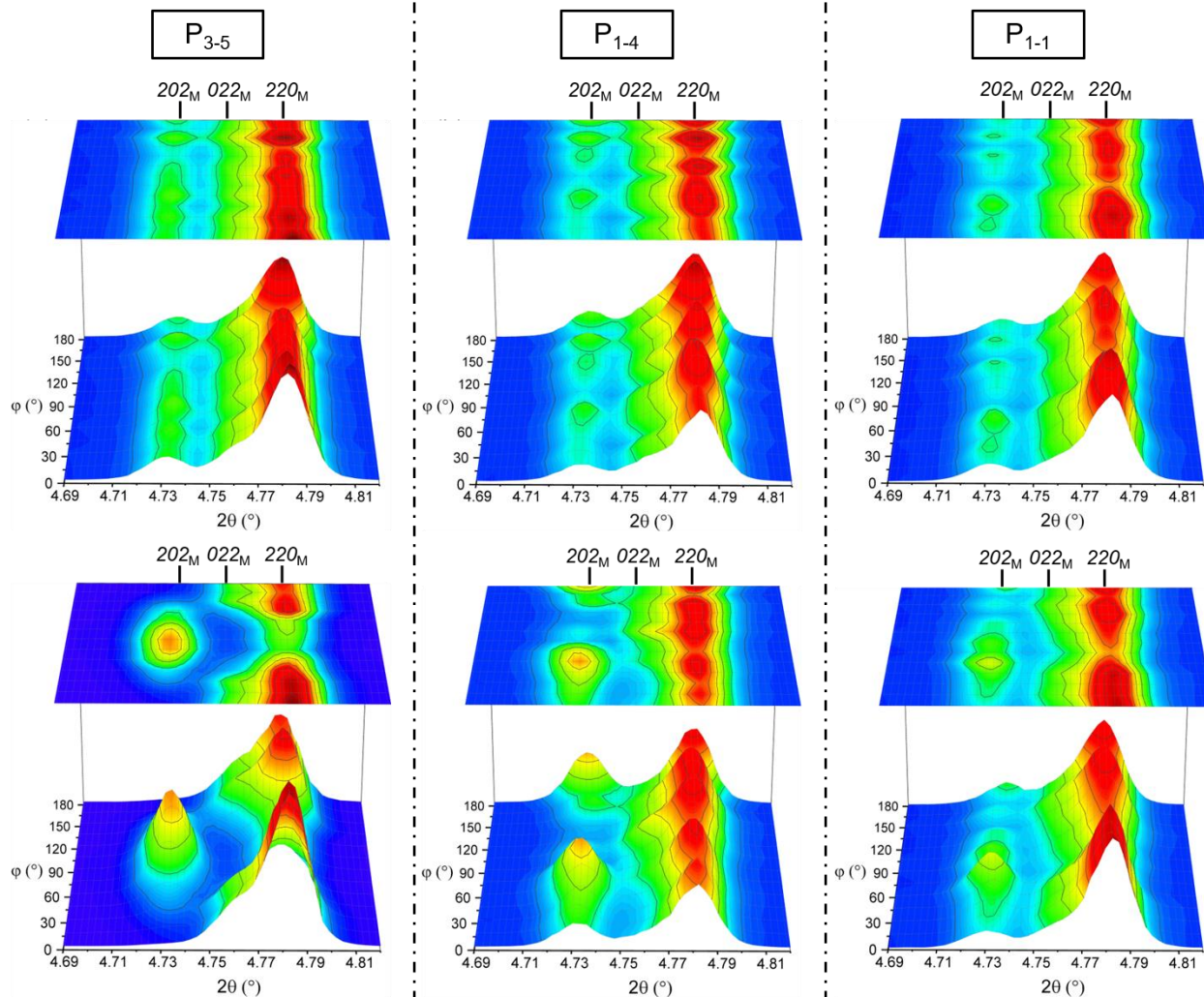


Figure S-21 Peak intensities as a function of azimuthal angle (ϕ) for P_{3-5} , P_{1-4} , and P_{1-1} in the undoped KNN partial-electrode sample with the electrode edge scan pattern. Plots (a), (b), (c) present the peak intensities in the virgin state, and (d), (e), (f) show the interchanged intensities at 3 kV/mm for P_{3-5} , P_{1-4} , and P_{1-1} , respectively.

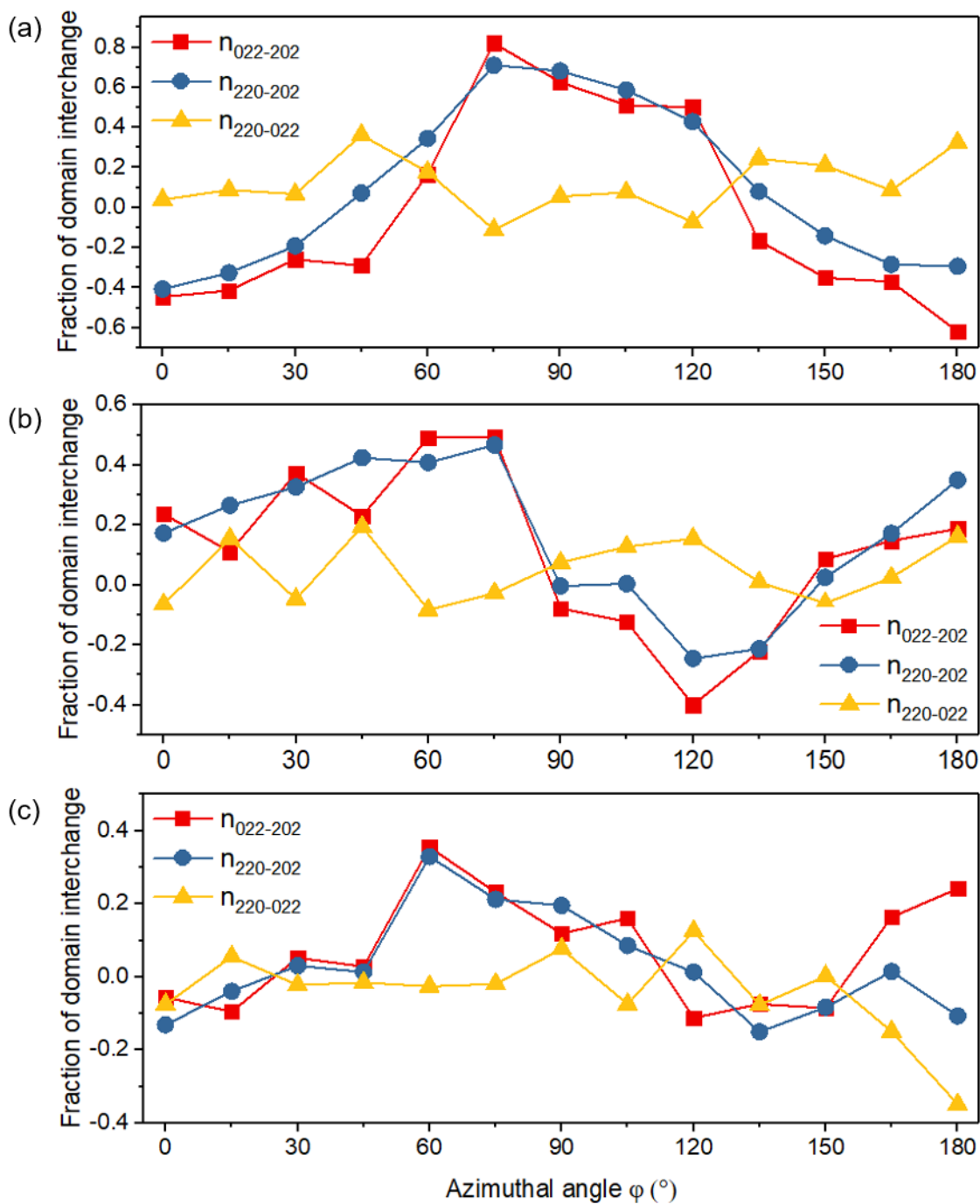


Figure S-22 Fraction of domain interchange in (a) P_{3-5} , (b) P_{1-4} , and (c) P_{1-1} in the pseudo-monoclinic (orthorhombic) phase undoped KNN partial-electrode sample with the electrode edge scan pattern at 3 kV/mm.

▪ Representative pixels in the doped KNN partial-electrode sample, electrode edge scan

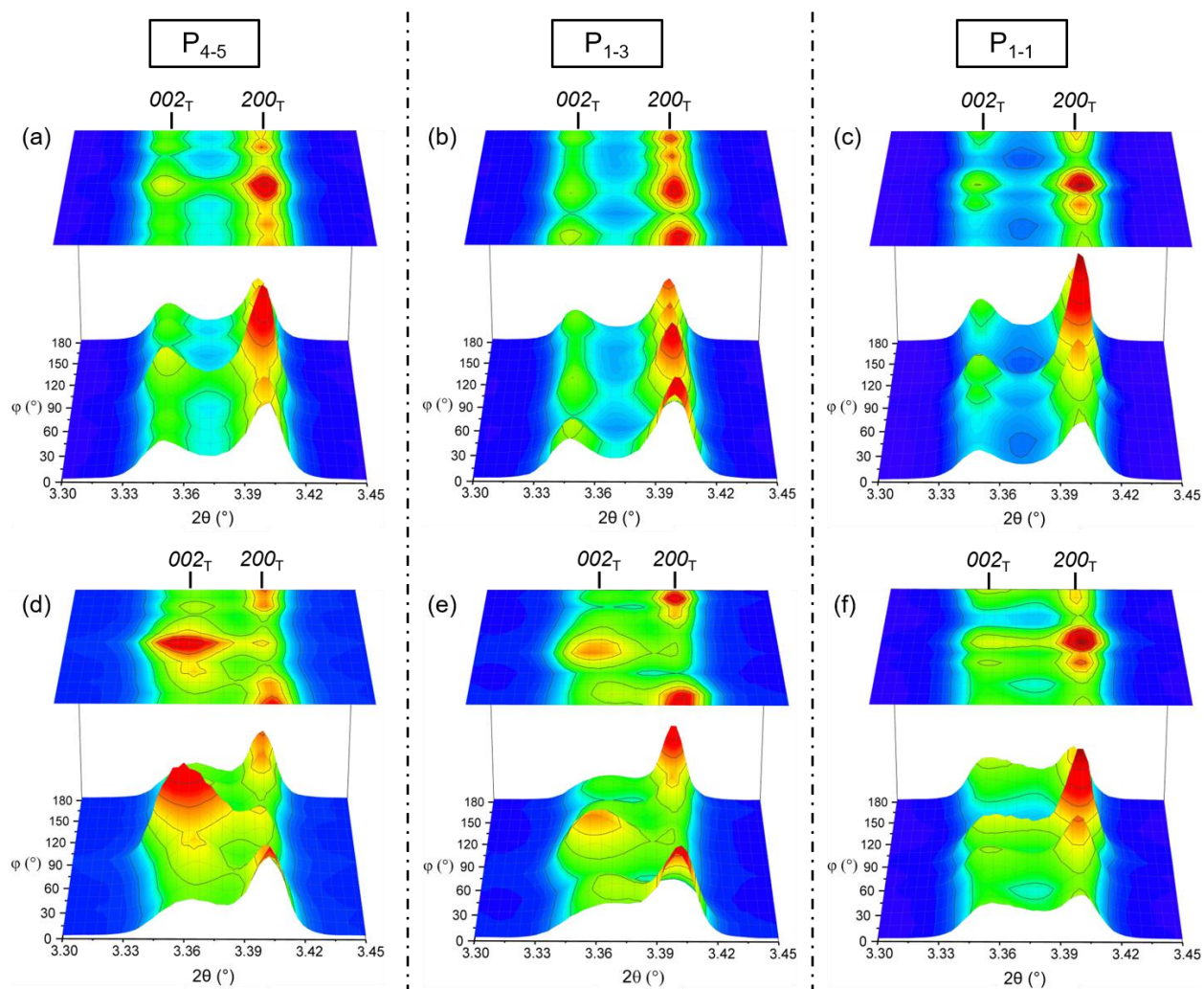


Figure S-23 Peak intensities as a function of azimuthal angle (ϕ) for P_{4-5} , P_{1-3} , and P_{1-1} in the doped KNN partial-electrode sample with the electrode edge scan pattern. Plots (a), (b), (c) present the peak intensities in the virgin state, and (d), (e), (f) show the interchanged intensities at 3 kV/mm for P_{4-5} , P_{1-3} , and P_{1-1} , respectively.

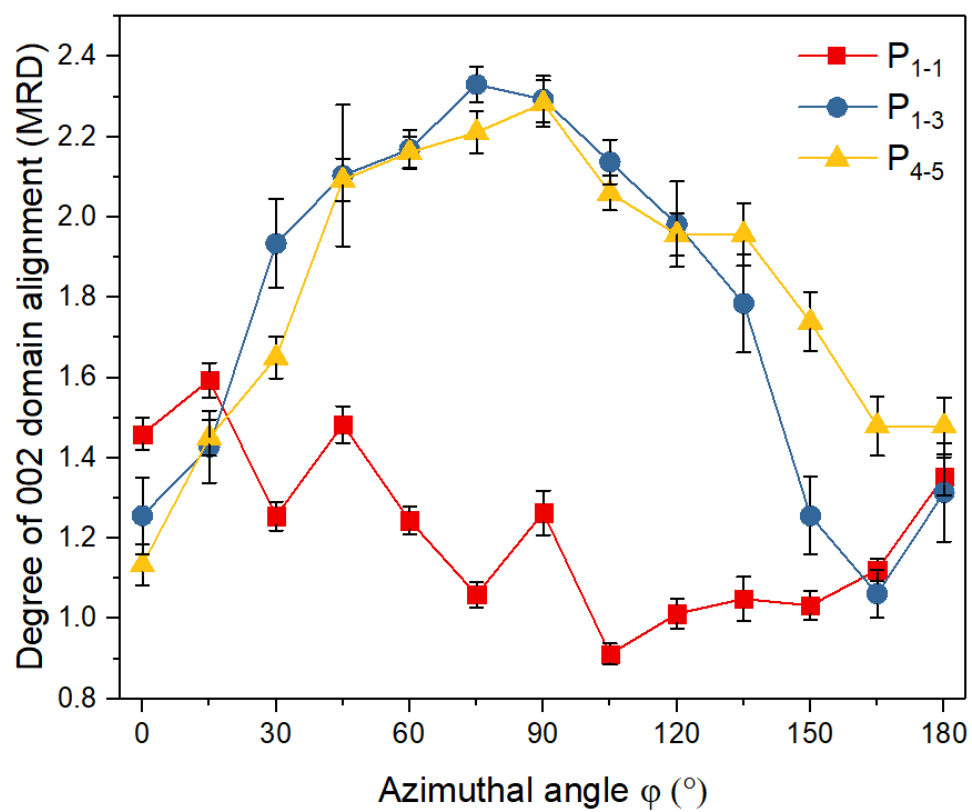


Figure S-24 The degree of 002 domain alignment (MRD) of representative pixels P_{4-5} , P_{1-3} , and P_{1-1} in the doped KNN partial-electrode sample with the electrode edge scan pattern at 3 kV/mm.

Appendix D: Supplementary Tables

▪ Partial-electrode sample, whole bar scan

Table 5 Summary of the maximum 002 domain texture strength and experimentally inferred local electric field direction in each scanned pixel for Nb-PZT 50/50 partial-electrode sample with the whole bar scan pattern under the application of macroscopic electric field 3kV/mm.

Degree of 002 domain alignment (MRD)										
	C 1	C 2	C 3	C 4	C 5	C 6	C 7	C 8	C 9	C 10
R 1	1.01	1.03	1.02	1.10	1.29	1.47	1.43	1.42	1.48	1.43
R 2	1.01	1.01	1.08	1.28	1.42	1.49	1.52	1.55	1.55	1.54
Local field direction at azimuthal angle φ ($^{\circ}$)										
	C 1	C 2	C 3	C 4	C 5	C 6	C 7	C 8	C 9	C 10
R 1	105	90	90	30	30	90	75	75	75	105
R 2	90	90	75	75	90	90	90	105	105	90
Note: “R” represents “Row”, “C” represents “Column”.										

Table 6 Summary of the maximum 002 domain texture strength and experimentally inferred local electric field direction in each scanned pixel for Nb-PZT 53/47 partial-electrode sample with the whole bar scan pattern under the application of macroscopic electric field 3kV/mm.

Degree of 002 domain alignment (MRD)										
	C 1	C 2	C 3	C 4	C 5	C 6	C 7	C 8	C 9	C 10
R 1	1.01	1.01	1.02	1.23	1.88	2.10	2.04	2.02	2.07	1.97
R 2	1.02	1.01	1.09	1.53	1.89	2.04	2.15	2.15	2.21	2.19
Local field direction at azimuthal angle φ ($^{\circ}$)										
	C 1	C 2	C 3	C 4	C 5	C 6	C 7	C 8	C 9	C 10
R 1	45	60	60	45	30	90	90	75	90	90
R 2	60	75	105	60	90	90	90	90	90	75
Note: “R” represents “Row”, “C” represents “Column”.										

Table 7 Summary of the maximum 111 domain texture strength and experimentally inferred local electric field direction in each scanned pixel for Nb-PZT 56/44 partial-electrode sample with the whole bar scan pattern under the application of macroscopic electric field 3kV/mm.

Degree of 111 domain alignment (MRD)										
	C 1	C 2	C 3	C 4	C 5	C 6	C 7	C 8	C 9	C 10
R 1	1.07	1.08	1.34	2.53	3.45	3.85	3.89	3.82	3.91	3.83
R 2	1.06	1.05	1.82	3.05	3.63	3.81	3.90	3.88	3.90	3.94
Local field direction at azimuthal angle φ ($^{\circ}$)										
	C 1	C 2	C 3	C 4	C 5	C 6	C 7	C 8	C 9	C 10
R 1	90	75	45	30	45	75	90	90	90	90
R 2	75	105	90	75	75	90	90	90	90	90
Note: “R” represents “Row”, “C” represents “Column”.										

Table 8 Summary of the maximum 002 domain texture strength and experimentally inferred local electric field direction in each scanned pixel for doped KNN partial-electrode sample with the whole bar scan pattern under the application of macroscopic electric field 3kV/mm.

Degree of 002 domain alignment (MRD)										
	C 1	C 2	C 3	C 4	C 5	C 6	C 7	C 8	C 9	C 10
R 1	1.01	1.01	1.01	1.01	1.36	1.84	1.69	1.56	1.45	1.40
R 2	1.02	1.00	1.00	1.08	1.50	2.10	2.34	2.26	2.28	2.25
Local field direction at azimuthal angle φ ($^{\circ}$)										
	C 1	C 2	C 3	C 4	C 5	C 6	C 7	C 8	C 9	C 10
R 1	75	45	105	45	45	45	75	75	105	75
R 2	120	75	60	90	75	90	90	90	90	75
Note: “R” represents “Row”, “C” represents “Column”.										

Table 9 Summary of fraction of domain interchange and experimentally inferred local electric field direction in each scanned pixel for undoped KNN partial-electrode sample with the whole bar scan pattern under the application of macroscopic electric field 3kV/mm.

Fraction of domain interchange, $n_{022-202}$										
	C 1	C 2	C 3	C 4	C 5	C 6	C 7	C 8	C 9	C 10
R 1	0.16	0.03	0.22	0.45	0.47	0.63	0.59	0.59	0.60	0.74
R 2	0.52	0.47	0.52	0.36	0.53	0.52	0.52	0.53	0.54	0.68
Local field direction at azimuthal angle φ ($^{\circ}$)										
	C 1	C 2	C 3	C 4	C 5	C 6	C 7	C 8	C 9	C 10
R 1	15	15	30	30	60	30	90	75	75	90
R 2	90	105	90	90	75	90	90	90	75	75
Fraction of domain interchange, $n_{220-202}$										
	C 1	C 2	C 3	C 4	C 5	C 6	C 7	C 8	C 9	C 10
R 1	0.13	0.07	0.25	0.43	0.44	0.59	0.58	0.59	0.54	0.65
R 2	0.47	0.35	0.38	0.38	0.43	0.50	0.48	0.51	0.51	0.59
Local field direction at azimuthal angle φ ($^{\circ}$)										
	C 1	C 2	C 3	C 4	C 5	C 6	C 7	C 8	C 9	C 10
R 1	60	0	0	30	75	30	105	75	60	90
R 2	90	105	105	60	75	90	90	90	75	75
Note: "R" represents "Row", "C" represents "Column".										

- **Partial-electrode sample, electrode edge scan**

Table 10 Summary of 002 domain texture strength and experimentally inferred local electric field direction in each scanned pixel for Nb-PZT 50/50 partial-electrode sample with the electrode edge scan pattern under the application of macroscopic electric field 3kV/mm.

Degree of 002 domain alignment (MRD)						Local field direction at azimuthal angle ϕ (°)					
	C 1	C 2	C 3	C 4	C 5		C 1	C 2	C 3	C 4	C 5
R 1	1.44	1.51	1.61	1.59	1.60	R 1	60	45	90	75	90
R 2	1.44	1.52	1.46	1.59	1.61	R 2	45	60	60	75	90
R 3	1.42	1.47	1.52	1.50	1.51	R 3	60	75	75	90	75
R 4	1.46	1.49	1.56	1.59	1.58	R 4	90	90	75	90	90

Note: “R” represents “Row”, “C” represents “Column”.

Table 11 Summary of 002 domain texture strength and experimentally inferred local electric field direction in each scanned pixel for Nb-PZT 53/47 partial-electrode sample with the electrode edge scan pattern under the application of macroscopic electric field 3kV/mm.

Degree of 002 domain alignment (MRD)						Local field direction at azimuthal angle ϕ (°)					
	C 1	C 2	C 3	C 4	C 5		C 1	C 2	C 3	C 4	C 5
R 1	1.76	2.16	2.55	2.29	2.42	R 1	15	15	60	105	75
R 2	1.99	2.15	2.33	2.24	2.38	R 2	45	45	45	60	90
R 3	2.12	2.29	2.17	2.21	2.21	R 3	60	60	60	75	90
R 4	1.97	2.17	2.17	2.14	2.30	R 4	60	75	90	90	75

Note: “R” represents “Row”, “C” represents “Column”.

Table 12 Summary of 111 domain texture strength and experimentally inferred local electric field direction in each scanned pixel for Nb-PZT 56/44 partial-electrode sample with the electrode edge scan pattern under the application of macroscopic electric field 3kV/mm.

Degree of 111 domain alignment (MRD)						Local field direction at azimuthal angle ϕ ($^{\circ}$)					
	C 1	C 2	C 3	C 4	C 5		C 1	C 2	C 3	C 4	C 5
R 1	3.86	3.85	3.94	3.90	3.94	R 1	30	60	75	90	90
R 2	3.78	3.89	3.92	3.89	3.97	R 2	60	60	75	90	90
R 3	3.74	3.77	3.82	3.84	3.82	R 3	60	75	75	90	90
R 4	3.62	3.70	3.60	3.82	3.87	R 4	75	75	75	90	90

Note: “R” represents “Row”, “C” represents “Column”.

Table 13 Summary of fraction of domain interchange and experimentally inferred local electric field direction in each scanned pixel for undoped KNN partial-electrode sample with the electrode edge scan pattern under the application of macroscopic electric field 3kV/mm.

Fraction of domain interchange, $n_{022-202}$						Local field direction at azimuthal angle ϕ ($^{\circ}$)					
	C 1	C 2	C 3	C 4	C 5		C 1	C 2	C 3	C 4	C 5
R 1	0.36	0.25	0.28	0.49	0.79	R 1	60	30	60	75	75
R 2	0.47	0.56	0.50	0.44	0.65	R 2	90	105	90	90	60
R 3	0.81	0.62	0.76	0.77	0.82	R 3	90	90	105	90	75
R 4	0.71	0.61	0.69	0.65	0.75	R 4	90	90	60	90	90

Fraction of domain interchange, $n_{220-202}$						Local field direction at azimuthal angle ϕ ($^{\circ}$)					
	C 1	C 2	C 3	C 4	C 5		C 1	C 2	C 3	C 4	C 5
R 1	0.33	0.19	0.41	0.47	0.66	R 1	60	30	30	75	75
R 2	0.59	0.60	0.62	0.53	0.56	R 2	90	105	90	90	60
R 3	0.75	0.63	0.68	0.69	0.71	R 3	90	90	90	90	75
R 4	0.57	0.58	0.68	0.67	0.64	R 4	90	75	105	105	90

Note: “R” represents “Row”, “C” represents “Column”.

Table 14 Summary of 002 domain texture strength and experimentally inferred local electric field direction in each scanned pixel for doped KNN partial-electrode sample with the electrode edge scan pattern under the application of macroscopic electric field 3kV/mm.

Degree of 002 domain alignment (MRD)						Local field direction at azimuthal angle ϕ (°)					
	C 1	C 2	C 3	C 4	C 5		C 1	C 2	C 3	C 4	C 5
R 1	1.59	2.35	2.33	1.89	1.61	R 1	15	60	75	75	75
R 2	1.56	2.04	2.40	2.45	2.32	R 2	45	45	75	90	90
R 3	1.51	1.79	2.04	2.19	2.31	R 3	45	60	75	90	105
R 4	1.59	1.59	1.85	2.09	2.28	R 4	120	105	75	90	90

Note: “R” represents “Row”, “C” represents “Column”.

Appendix E: Reprint Permissions

M. Acosta *et al.*, “BaTiO₃-based piezoelectrics: Fundamentals, current status, and perspectives,” *Applied Physics Reviews*, vol. 4, no. 4. American Institute of Physics Inc., 01-Dec-2017.

This Agreement between Jianwei ("You") and AIP Publishing ("AIP Publishing") consists of your license details and the terms and conditions provided by AIP Publishing and Copyright Clearance Center.	
License Number	4853941352993
License date	Jun 21, 2020
Licensed Content Publisher	AIP Publishing
Licensed Content Publication	Applied Physics Reviews
Licensed Content Title	BaTiO ₃ -based piezoelectrics: Fundamentals, current status, and perspectives
Licensed Content Author	M. Acosta, N. Novak, V. Rojas, et al
Licensed Content Date	Dec 1, 2017
Licensed Content Volume	4
Licensed Content Issue	4
Type of Use	Thesis/Dissertation
Requestor type	Student
Format	Print and electronic
Portion	Figure/Table
Number of figures/tables	1
Title	Inhomogeneous Electric Field-Induced Domain Reorientation and Phase Transitions in Piezoceramics
Institution name	North Carolina State University
Expected presentation date	Jul 2020
Portions	Figure 1
Requestor Location	Jianwei 1440 Collegiate Circle, Apt 202 RALEIGH, NC 27606 United States Attn: Jianwei

J. F. Li, K. Wang, F. Y. Zhu, L. Q. Cheng, and F. Z. Yao, "(K, Na) NbO₃-based lead-free piezoceramics: Fundamental aspects, processing technologies, and remaining challenges," *J. Am. Ceram. Soc.*, vol. 96, no. 12, pp. 3677–3696, 2013.

This Agreement between Jianwei ("You") and John Wiley and Sons ("John Wiley and Sons") consists of your license details and the terms and conditions provided by John Wiley and Sons and Copyright Clearance Center.	
License Number	4853371071977
License date	Jun 20, 2020
Licensed Content Publisher	John Wiley and Sons
Licensed Content Publication	Journal of the American Ceramic Society
Licensed Content Title	(K, Na)NbO ₃ -Based Lead-Free Piezoceramics: Fundamental Aspects, Processing Technologies, and Remaining Challenges
Licensed Content Author	Fang-Zhou Yao, Li-Qian Cheng, Fang-Yuan Zhu, et al
Licensed Content Date	Nov 26, 2013
Licensed Content Volume	96
Licensed Content Issue	12
Licensed Content Pages	20
Type of use	Dissertation/Thesis
Requestor type	University/Academic
Format	Print and electronic
Portion	Figure/table
Number of figures/tables	1
Will you be translating?	No
Title	Inhomogeneous Electric Field-Induced Domain Reorientation and Phase Transitions in Piezoceramics
Institution name	North Carolina State University
Expected presentation date	Jul 2020
Portions	Figure 2
Requestor Location	Jianwei 1440 Collegiate Circle, Apt 202 RALEIGH, NC 27606 United States Attn: Jianwei
Publisher Tax ID	EU826007151